Title: “Thermo-Chemical Dynamics in Earth’s Core Arising from Interactions with the Mantle”.

Authors: Christopher J. Davies and Sam Greenwood, School of Earth and Environment, University of Leeds, Leeds LS2 9JT, UK.

This article is an invited review that has been submitted for publication to the AGU Monograph “Core-Mantle Coevolution - A multidisciplinary approach”.

Thermo-Chemical Dynamics in Earth's Core Arising from Interactions with the Mantle

Christopher J. Davies[a], Sam Greenwood[a]

[a] *School of Earth and Environment, University of Leeds, Leeds LS2 9JT, UK (tel: +44 (0) 113 34 31140; email: c.davies@leeds.ac.uk*

Abstract

Thermo-chemical interactions at the core-mantle boundary (CMB) play an integral role in determining the dynamics and evolution Earth's deep interior. This review considers the processes in the core that arise from heat and mass transfer at the CMB, with particular focus on thermo-chemical stratification and the precipitation of oxides. A fundamental parameter is the thermal conductivity of the core, which we estimate as $k = 70 - 110$ W m^{-1} K^{-1} at CMB conditions based on consistent extrapolation from a number of recent studies. These high conductivity values imply the existence of an early basal magma ocean (BMO) overlying a hot core and rapid cooling potentially leading to a loss of power to the dynamo before the inner core formed around $0.5 - 1$ Gyrs ago, the so-called "new core paradox". Coupling core thermal evolution modelling and calculations of chemical equilibrium between liquid iron and silicate melts suggests that FeO dissolved into the core after its formation, creating a stably stratified chemical layer below the CMB, while precipitation of MgO and SiO_2 was delayed until the last $2-3$ Gyrs and was therefore not available to power the early dynamo; however, once initiated, precipitation supplied ample power for field generation. We also present a possible solution to the new core paradox without requiring precipitation or radiogenic heating using $k = 70$ W m^{-1} K^{-1}. The model matches the present inner core size and heat flow and temperature at the top of the

convecting mantle. It predicts a present-day CMB heat flow of 8.5 TW, a chemically stable layer 100 km thick, and a BMO lifetime of 2 Gyrs.

Keywords:

1. Introduction

The core-mantle boundary (CMB) accommodates one of the most significant transitions in the structure and dynamics of the Earth system. The Preliminary Reference Earth Model (PREM Dziewonski and Anderson, 1981) shows that the horizontally-averaged density ρ and compressional wave speed V_p change by $\sim$40% across the CMB. In terms of physical properties the lower mantle is a poor thermal and electrical conductor and has a viscosity that is perhaps $10^{15} - 10^{20}$ times larger than that of the core, which allows it to sustain temperature variations of thousands of Kelvin and support large-scale dynamic structures such as the Large Low Velocity Provinces (LLVPs) that sit on the CMB (e.g. Garnero et al., 2016). The core, by contrast, is an excellent thermal and electrical conductor, while the low viscosity, similar to that of water (Pozzo et al., 2013), implies that the bulk of the core is undergoing turbulent convection. This stark contrast between structural and dynamical properties leads to thermo-chemical interactions at the CMB that provide power for generating the geomagnetic field and are important for determining the long-term evolution of the core and mantle systems.

In this paper we review recent progress in understanding core mantle interactions with a focus on the thermodynamics and fluid dynamics of the upper core; a complementary perspective from the mantle side can be found in Nakagawa (2020). Many excellent reviews of the CMB region already exist and so we focus on the main developments since the authoritative Treatise on Geophysics reviews by Nimmo (2015a,b); Buffett (2015); Hernlund and McNamara (2015) and Jaupart et al. (2015). Relevant background on geodynamo simulations has also been recently reviewed by Wicht and Sanchez (2019). To ensure a concise presentation we further focus on thermal and chemical interactions. Core-mantle interactions also influence the rotational dynamics of the Earth, a topic that was reviewed by Tilgner (2015) and more recently by Dumberry (2018), and the shape of the core-mantle boundary, which has recently been discussed in connection with the anomalously low (Koelemeijer et al., 2017) or high (Lau et al., 2017) density of LLVPs. Here we will assume that the CMB is spherical and that the core and mantle are co-rotating.

The dynamo process that maintains the geomagnetic field is ultimately driven by heat extracted across the CMB. Syntheses of paleointensity data show that the field has been continuously generated for at least the last 3.5 Gyrs (Tarduno et al., 2010; Biggin et al., 2015; Tauxe and Yamazaki, 2015; Bono et al., 2019), while recordings dating back to 4.2 Ga (Tarduno et al., 2015) are currently debated (Tang et al., 2019; Tarduno et al., 2020). Heat loss at the CMB drives vigorous convection that maintains the bulk core in a state close to adiabatic temperature and uniform composition (e.g. Braginsky and Roberts, 1995; Nimmo, 2015a). Compared to the mean CMB temperature of $\sim$4000 K (Lay et al., 2009; Davies et al., 2015) the thermal anomalies associated with core convection are $O(10^{-3})$ K (Stevenson, 1987; Bloxham and Jackson, 1990), while the convective chemical anomalies are many orders of magnitude smaller than the mean light element mass fraction of $\sim$10 wt%. Consequently, even small thermo-chemical anomalies resulting from interactions at the CMB can have a significant effect on core dynamics.

The dynamics that result from thermo-chemical core-mantle coupling are dictated by the fluxes of heat and mass at the CMB. The total CMB heat flow Q^{c} is poorly constrained even for the present day, with current estimates suggesting the range $Q^{c} = 7 - 17$ TW (Lay et al., 2009; Nimmo, 2015a), which amounts to $\sim 15 - 50\%$ of

Earth's total heat budget (Jaupart et al., 2015). Back in time Q^{c} must be inferred from numerical models of mantle dynamics (Jaupart et al., 2015; Nakagawa, 2020). The key quantity for core dynamics is the superadiabatic heat flow $Q^{\mathrm{c}} - Q^{\mathrm{c}}_{\mathrm{a}}$. The adiabatic heat flow on the core side of the CMB (radius $r = r_{\mathrm{c}}$) is

$$Q^{\mathrm{c}}_{\mathrm{a}} = -4\pi r_{\mathrm{c}}^2 k^{\mathrm{c}} \left.\frac{\partial T^{\mathrm{c}}_{\mathrm{a}}}{\partial r}\right|_{r=r_{\mathrm{c}}}, \tag{1}$$

where T_{a} is the adiabatic temperature, k^{c} is the thermal conductivity and superscripts c and m denote quantities on the core and mantle side of the CMB respectively (parameter values are given in Table 2). The total heat flow on the core side of the CMB is

$$\begin{aligned} Q^{\mathrm{c}} &= -4\pi r_{\mathrm{c}}^2 k^{\mathrm{m}} \left.\frac{\partial T^{\mathrm{m}}}{\partial r}\right|_{r=r_{\mathrm{c}}} - 4\pi r_{\mathrm{c}}^2 \left[R^{\mathrm{c}}_i - R^{\mathrm{m}}_i\right] \mathbf{n} \cdot \mathbf{i}_i \\ Q^{\mathrm{c}} &= Q^{\mathrm{m}} + Q_{\mathrm{h}} \end{aligned} \tag{2}$$

(Davies et al., 2020), where $\mathbf{i}_i$ is the mass flux per unit area of element i (e.g. Mg, Si, O), $\mathbf{n}$ is the outward unit normal to the CMB and $[R^{\mathrm{c}}_i - R^{\mathrm{m}}_i] < 0$ (> 0) is the amount of heat released (absorbed) as one formula unit of i is transferred from the core to the mantle or vice versa (Pozzo et al., 2019). Here $R_i = \mu_i - T(\partial\mu_i/\partial T)_{P,T}$ is the heat of reaction coefficient with μ_i the chemical potential of element i and P the pressure. If the heat of reaction $Q_{\mathrm{h}} < 0$, corresponding for example to an exothermic reaction with accompanying mass transfer into the core ($\mathbf{n}\cdot\mathbf{i} < 0$) then the heat flow available to core convection is reduced below the heat Q^{m} conducted through the lower mantle boundary layer, while $Q_{\mathrm{h}} > 0$ acts as a heat source, increasing Q^{c} for a given Q^{m}. If $Q^{\mathrm{c}} > Q^{\mathrm{c}}_{\mathrm{a}}$ then thermal convection probably occurs throughout the core. Conversely, if $Q^{\mathrm{c}} < Q^{\mathrm{c}}_{\mathrm{a}}$ then a thermally stratified layer exists below the CMB in which heat is transported by conduction and vertical motion is strongly impeded. Depending on the radial variation of $k(r)$ and the distribution of buoyancy sources within the core, which are both uncertain at present, it is possible to produce stratification at intermediate depths (Gomi et al., 2013). In this review we will mainly consider the case where stratification arises directly below the CMB.

The total chemical flux I_i of species i at the CMB is given by

$$I_i = -4\pi r_{\mathrm{c}}^2 \rho D_i \left.\frac{\partial w_i^{\mathrm{c}}}{\partial r}\right|_{r=r_{\mathrm{c}}} + 4\pi r_{\mathrm{c}}^2 \alpha_i^{\mathrm{c}} \alpha_i^{\mathrm{D}} g, \tag{3}$$

where D_i, w_i^{c}, α_i^{c} and α_i^{D} are respectively the self-diffusion coefficient, mass fraction, compositional expansion coefficient and barodiffusion coefficient of species i and g is radial gravity. Unlike the heat flux, I_i is continuous at the CMB if the small effect of core contraction is neglected (Gubbins et al., 2003; Davies et al., 2020). In equation (3) the second term on the right-hand side is the barodiffusion, representing transport of light element down the hydrostatic pressure gradient $\mathrm{d}P/\mathrm{d}r = -\rho g$, while element transport along the temperature gradient (thermodiffusion) is small and has been omitted (Gubbins et al., 2004). I is very hard to estimate because global mass balance constrains the bulk chemical composition of the core and mantle but not the compositional gradient at the CMB. Therefore much recent work has focused on establishing the equilibrium chemical conditions at the CMB, which relate compositions on either side of the interface (e.g. Fischer et al., 2015; Badro et al., 2018; Pozzo et al., 2019). If $I_i < 0$ then light elements leave the mantle, which almost certainly results in chemical stratification below the CMB since the chemical anomalies associated with core convection are minute and are hence unable to mix the anomalously light fluid downwards (Buffett and Seagle, 2010; Davies et al., 2018, 2020). Conversely, $I_i > 0$ implies that light elements precipitate out of solution (as oxides) and underplate onto the base of the mantle; the residual fluid, slightly iron-rich compared to the fluid below, will sink via Rayleigh-Taylor instability thus helping to drive core flow (O'Rourke and Stevenson, 2016).

The lower mantle is thermally and chemically heterogeneous and so heat and mass exchange should vary with location on the CMB. Lateral variations in CMB heat flow are expected from seismic tomography and geodynamic simulations (see for example Gubbins, 2003; Olson et al., 2015, for reviews), which drive baroclinic flows at the top of the core (e.g. Zhang, 1992) that might affect the observed magnetic field (Gubbins et al., 2007; Aubert et al., 2007). CMB heat flow heterogeneity can also alter a pre-existing stable layer (e.g. Olson et al., 2017; Christensen, 2018; Cox et al., 2019) or even induce regional stratification if the anomalies are strong enough to make the heat flow locally subadiabatic (Olson et al., 2018; Mound et al., 2019). Lateral variations in chemical flux also seem likely if LLVPs are compositionally distinct (Garnero et al., 2016), though this effect does not appear to have been studied to date.

The existence of stratification and/or precipitation has important implications for the dynamics and evolution of the core. Stratified layers suppress radial motion and may support strong toroidal fields (Hardy et al., 2020) and distinct classes of wave motions (Braginsky, 1999) that are observed as periodic variations of the geomagnetic field (Buffett, 2014; Buffett et al., 2016). Such a layer also acts to filter the field that is generated in the bulk core (Christensen, 2006; Gastine et al., 2020), effectively filtering our view of the dynamo process, which is primarily based on observations that only probe CMB field. Precipitation has recently been advocated as the primary long-term power source for Earth's magnetic field (O'Rourke and Stevenson, 2016; Hirose et al., 2017), while precipitation products may have been incorporated into the mantle via Rayleigh-Taylor instability (Helffrich et al., 2018). However, at present, a definitive observation of either stratification or precipitation is lacking. Therefore, in this review we focus on predictions from modelling studies, such as the thickness and strength of stratification and the thermal and magnetic history of the core, that add further constraints to complement the observational evidence.

Broadly speaking, there are presently 2 scenarios for thermo-chemical core-mantle interactions that depend to a large extent on the core thermal conductivity k (see Table 1). In the "low conductivity" scenario the core cooled slowly over geological time, powering the geomagnetic field by thermal convection until the onset of inner core freezing around 1 billion years ago, which provided additional power for field generation through release of latent heat and light elements (e.g. Buffett et al., 1996; Labrosse et al., 2001; Gubbins et al., 2003, 2004; Nimmo et al., 2004). Due to the low conductivity the present adiabatic heat flow is predicted to be around $4-6$ TW and hence thermal convection probably operated throughout the core until the present-day. In this scenario, thermal history models indicate that the core temperature remained below the mantle solidus over the last 4 Gyrs, though a Basal Magma Ocean (BMO Labrosse et al., 2007) could still have formed via mantle crystallisation that proceeded from the middle outwards (Stixrude et al., 2009). With low k, models predict that the BMO can survive to the present-day while still providing enough power to the geodynamo (via Q^{c}) to sustain the magnetic field (Blanc et al., 2020). This situation would facilitate efficient long-term chemical exchange between the core and mantle owing to the much higher self-diffusion coefficients of chemical species in the liquid (e.g. Adjaoud et al., 2011; Posner et al., 2018; Caracas et al., 2019).

The second scenario for thermo-chemical core-mantle evolution corresponds to a high thermal conductivity exceeding around 90 W $\mathrm{m}^{-1}\mathrm{K}^{-1}$. In order to maintain the geomagnetic field for the last 3.5 Gyrs the core must cool faster to offset the enhanced power losses from thermal conduction, leading to an estimated inner core age of ∼0.5 − 0.7 Gyrs (Driscoll and Bercovici, 2014; Davies, 2015; Davies et al., 2015; Labrosse et al., 2015; Nimmo, 2015a). The high conductivity values predict $Q^{\mathrm{c}}_{\mathrm{a}} = 14$–16 TW, comparable to the upper estimates of Q^{c} at the present day and suggesting thermal stratification of the upper core. Rapid cooling further implies early core temperatures that far exceeded current estimates of the lower mantle solidus and hence the presence of a BMO. However, since release of latent and radiogenic heat in the BMO stifled heat loss from the core (Labrosse et al., 2007), maintaining the early magnetic field with high k may require that the BMO was short-lived (Davies et al., 2020).

The major problem posed by the high conductivity scenario is illustrated by parameterised models of coupled core-mantle evolution (Driscoll and Bercovici, 2014; O'Rourke et al., 2017) and could have been appreciated from the early study by Nimmo et al. (2004). With high k, classical parameterised mantle evolution models based on boundary layer theory predict an approximately exponential decline in CMB heat flow over time, which can lead to a loss of power to the dynamo before inner core nucleation around 1-2 Ga, in contradiction with paleomagnetic data (Biggin et al., 2015; Bono et al., 2019). However, the obvious remedy, increasing CMB heat flow and hence core cooling rate, leads to an old inner core that grows larger than its present size as determined by seismology. The apparent contradiction between observations and the fundamental model of core evolution has been termed the "new core paradox". The term "paradox" is used because higher k generally implies higher electrical conductivity in metals (Chester and Thellung, 1961) and hence weaker magnetic diffusion, which should be beneficial to dynamo action. Driscoll and Du (2019) show that the ratio of magnetic induction to diffusion declines in both high and low electrical conductivity limits and suggest that Earth's core came close to this "no dynamo" state prior to inner core nucleation. Thermal history models have

	low conductivity	high conductivity
k	$\lesssim 50$ W m^{-1}K^{-1}	$\gtrsim 90$ W m^{-1}K^{-1}
$Q^{\mathrm{c}}_{\mathrm{a}}$	$4 - 6$ TW	$14 - 16$ TW
Core cooling rate	Slow	Fast
Inner core age	$\sim$1 Gyr	$\sim$0.5 Gyrs
Thermal stratification	Never	Likely at present
Basal magma ocean (BMO)	Maybe, possibly long-lived	Likely, probably short-lived
Pre-inner core dynamo power	Secular cooling	Secular cooling, but precipitation maybe also required
Chemical exchange	Efficient with BMO	Efficient only in early times

Table 1: Two scenarios for core-mantle evolution described in the text. The CMB heat flow is estimated as $Q^{\mathrm{c}} = 7 - 17$ TW (Nimmo, 2015a).

attempted to overcome the new core paradox by invoking additional effects such as a significant amount of radiogenic heating (e.g. from ^{40}K, Driscoll and Bercovici, 2014) or gravitational power provided by the precipitation of MgO (O'Rourke et al., 2017) or SiO_2 (Hirose et al., 2017), though the viability of all of these processes has been questioned (Xiong et al., 2018; Du et al., 2019; Arveson et al., 2019).

In this review we first discuss the material properties of the core that are required to model the processes of stratification and precipitation, focusing on the composition on either side of the CMB and the core thermal conductivity (Section 2). This motivates us to consider the high conductivity scenario in the remainder of the review. In section 3 we describe recent studies of core-mantle chemical equilibrium and discuss constraints on the onset and rate of chemical precipitation and stratification below the CMB. Section 4 reviews thermal and chemical stratification at the top of the core, while Section 5 discusses recent studies of chemical precipitation. Finally, in Section 6 we discuss potential resolutions to the "new core paradox".

2. Material Properties of the Core

The dynamics and evolution of the CMB region are intimately linked to processes in the bulk core. The standard tools used to investigate core evolution on Gyr timescales are thermal history models, which are 2D (radius and time) parameterisations of the complex 4D processes that arise in direct numerical simulation (DNS) of core dynamics. The primary constraints on these models, and the predictions of stratification and precipitation processes they make, are 1) the continuous generation of a magnetic for at least the last 3.5 Gyrs (Tarduno et al., 2010) and; 2) to match the present-day radius $r_{\rm i}$ of the inner core, $r_{\rm i} = 1221$ km. Therefore constraining the evolution of the CMB region requires knowledge of the material properties of the whole core. The growth rate of the inner core depends on the rate at which the core cools and also the slopes of the melting temperature $T_{\rm m}$ and ambient temperature T of the core alloy. The power available to the dynamo depends on many factors, including the cooling rate and the thermal conductivity k.

The challenge of estimating core material properties arises from the extreme conditions that must be replicated. The pressure ranges from $P = 135$ GPa to $P = 330$ GPa across the core (Dziewonski and Anderson, 1981), T is several thousands of Kelvin, while the mass fractions $w_i^{\rm c}$ of light element i are themselves determined by partitioning behaviour at high P and T. The main experimental tool used to access these conditions is the laser-heated diamond anvil cell. Here the challenges include minimising temperature gradients across small samples (Sinmyo et al., 2019), identifying melting (Anzellini et al., 2013), and the potential for oxidation of the sample at high $P-T$ (Frost et al., 2010). *Ab initio* calculations can sample core $P-T$ conditions, but also contain uncertainties such as the form of the exchange-correlation functional and must ultimately be ground-truthed by experiments. Hence, determinations of core properties do come with appreciable uncertainties. In this review we will explicitly discuss uncertainties arising in determinations of core thermal conductivity and partitioning behaviour, but we will not provide a systematic survey of all parameters. We will also focus on models of the core that are consistent with seismic observations (Badro et al., 2014; Davies et al., 2015).

Present-day constraints on P, T and w_i^{c} come from the liquid core density ρ, which is about 10 wt% lighter than pure iron, and also from the density jump $\Delta\rho$ at the inner core boundary (ICB, radius r_{i}). Fluctuations in ρ due to convection are small (Stevenson, 1987) while time variations in core composition are tiny (Davies, 2015) and so the pressure gradient is determined from hydrostatic balance with ρ and gravity g derived from 1D seismic models of the core (Dziewonski and Anderson, 1981; Irving et al., 2018). Part of the observed density jump, $\Delta\rho_m = 240$ kg m^{-3} (Alfè et al., 2002c), arises from the phase change at the ICB; the rest determines the excess concentration of light elements in the liquid core compared to the solid core. Matching candidate compositions derived from partitioning behaviour at ICB conditions to observational constraints on $\Delta\rho$ allows to estimate the present core composition and hence the melting temperature T_{m} of the iron alloy at the CMB (e.g. Alfè et al., 2002a). The core temperature T is usually assumed to vary adiabatically outside thin boundary layers and stable regions. The anchor point for T is the value of T_{m} at the ICB. The chemical properties α_i^{c}, α_i^{D} and R_i are calculated from chemical potentials at fixed P, T and composition. Finally, transport properties such as the core viscosity ν, self-diffusion coefficients D_i and thermal conductivity can be calculated for specified composition at points along core $P-T$ curves (e.g. Pozzo et al., 2013).

The ICB density jump $\Delta\rho$ is rather uncertain (see Wong et al., 2021, for a recent review). In this work we take the range obtained from normal modes of $\Delta\rho = 800 \pm 200$ kg m^{-3} (Masters and Gubbins, 2003) and consider the three values $\Delta\rho =$ 600 kg m^{-3}, 800 kg m^{-3} and 1000 kg m^{-3}. The parameter values for each $\Delta\rho$ are listed in Table 2. These are generally taken from Davies et al. (2015) where more details can be found. In the following subsections we review constraints on the core and magma ocean compositions that are relevant for understanding mass exchange at the CMB. We then consider the core temperature structure and sketch a derivation of the core energy balance before discussing recent estimates of core thermal conductivity.

2.1. Bulk Composition of the Core and Basal Magma Ocean

The composition of the core and the nature and abundance of mineral phases at the base of the mantle are still rather uncertain at present (Hirose et al., 2013; Garnero et al., 2016). Core formation models suggest that O, Si and S are likely to partition into metal (Rubie et al., 2015a; Badro et al., 2015), though at very high temperatures other elements such as Mg can also become siderophile (O'Rourke and Stevenson, 2016). Carbon has also been considered (Rubie et al., 2015a), but recent work suggests C partitions weakly into metal at high P and T (Fischer et al., 2020). Calculations attempting to match the present-day core mass and $\Delta\rho$ show that O and C partition almost exclusively into liquid at ICB conditions (Alfè et al., 2002a; Li et al., 2019) and so matching the overall mass of the core requires another element that partitions evenly such as S or Si (Alfè et al., 2002a). Hydrogen may also be present if the core temperature is on the lower end of present estimates (Umemoto and Hirose, 2020). The main stable phase in the present lower mantle is $(Mg,Fe)SiO_3$ silicate perovskite, with ∼15% ferropericlase and some calcium silicate perovskite (Garnero et al., 2016). Bridgmanite composition is dominated by the oxides SiO_2

Symbol	100%Fe	82%Fe-8%O-10%Si	79%Fe-13%O-8%Si	81%Fe-17%O-2%Si
$\Delta\rho$ (kg m^{-3})	240	600	800	1000
w_O^S	–	0.0002	0.0004	0.0006
w_{Si}^S	–	0.0554	0.0430	0.0096
w_O^L	–	0.0256	0.0428	0.0559
w_{Si}^L	–	0.0560	0.0461	0.0115
C_p (J/kg/K)	715—800	–	–	–
$L(r_\mathrm{i})$ (MJ/kg)	0.75	–	–	–
$T_\mathrm{m}(r_\mathrm{i})$ (K)	6350	5900	5580	5320
$\left.\frac{\mathrm{d}T_\mathrm{m}}{\mathrm{d}P}\right\vert_{r_\mathrm{i}}$ (K/GPa)	9.01	9.01	9.01	9.01
$\alpha_\mathrm{T}(r_\mathrm{i})$ ($\times 10^{-5}$/K)	1.0	-	-	-
$T_\mathrm{a}(r_\mathrm{c})$ (K)	4735	4290	4105	3910
$\left.\frac{\partial T_\mathrm{a}}{\partial P}\right\vert_{r_\mathrm{i}}$ (K/GPa)	6.96	6.25	6.01	5.81
$\left.\frac{\partial T_\mathrm{a}}{\partial r}\right\vert_{r_\mathrm{c}}$ (K/km)	-1.15	-1.03	-1.00	-0.96
k (W/m/K)		See	Text	
D_O ($\times 10^{-8}$ m^2/s)	-	1.31	1.30	-
D_{Si} ($\times 10^{-8}$ m^2/s)	-	0.52	0.46	-
ν ($\times 10^{-7}$ m^2/s)	6.9	6.8	6.7	-
$\alpha_\mathrm{O}^\mathrm{D}$ ($\times 10^{-12}$ kg/m^3 s)	–	0.72	0.97	1.11
$\alpha_\mathrm{Si}^\mathrm{D}$ ($\times 10^{-12}$ kg/m^3 s)	–	1.19	1.10	40.6
		O	Si	
α_i^c	–	1.1	0.87	
$R^\mathrm{c} - R^\mathrm{m}$ (eV/f.u.)	–	-2.5		

Table 2: Core material properties for pure iron and three Fe-O-Si mixtures denoted by their molar concentrations in the header line. Superscripts c have been suppressed for clarity. Gravity g, pressure P and gravitational potential ψ are derived from the PREM density ρ. Quantities in the first section define the core chemistry model. Numbers in the second section determine the core temperature properties in the third section, which are given for the present day. The core temperature is assumed to follow an adiabat, denoted T_a, and the melting temperature of the core alloy is denoted T_m. L denotes the latent heat of fusion and α_T is the thermal expansion coefficient. CMB values for transport properties calculated along the corresponding adiabats are given in section four. The CMB radius is denoted $r_\mathrm{c} = 3480$ km, the present-day ICB radius is $r_\mathrm{i} = 1221$ km. α_i^c are the compositional expansion coefficients, $R^\mathrm{c} - R^\mathrm{m}$ is the heat of reaction coefficient [equation (2)] from Pozzo et al. (2019) and α_i^D is the barodiffusion coefficient [equation (3)] from Gubbins and Davies (2013). Adapted from Davies et al. (2015).

and MgO (Garnero et al., 2016).

Much recent work has focused on the partitioning of Mg, Si and O between the core and mantle. Mg and Si are of interest because they may become saturated in the core as the planet cools, precipitating as oxides MgO and SiO_2 respectively, which releases gravitational energy that is available to power the geodynamo (O'Rourke and Stevenson, 2016; Badro et al., 2016; Hirose et al., 2017; Mittal et al., 2020). The study of FeO has attracted attention because it provides a mechanism for oxygen to enter the core, either from FeO in ferropericlase in the present Earth (Frost et al., 2010) or from an FeO-enriched basal magma ocean in the past (Davies et al., 2020), which leads to a stable stratification below the CMB (Buffett and Seagle, 2010; Davies et al., 2020). We will therefore focus on the interactions between Fe, Mg, Si and O in the remainder of this review. Note that the material properties listed in Table 2 were obtained without Mg, though the error is probably not significant since the fraction of Mg dissolved in the core is probably much less than Si or O.

The initial bulk compositions of the core and mantle were set during planetary differentiation. Recent multi-stage core formation models find broadly consistent initial oxygen concentrations in the range $2-5$ wt% (Badro et al., 2015; Rubie et al., 2015b), but diverge on the estimated silicon content with Badro et al. (2015) finding $2-3.6$ wt% Si while Rubie et al. (2015b) obtaining $8-9$ wt% Si. The difference is partly due to the inferred oxidation state (oxidising or reducing) of accretion materials, though other uncertainties in the core formation process mean that initial Si and O core concentrations in the range $1-10$ wt% cannot be ruled out (Fischer et al., 2017). Partitioning of Mg has generally been omitted in core formation studies. Badro et al. (2016) ran multi-stage core formation models and found 0.8 wt% MgO could be delivered to the core without a late giant impact, while $1.6-3.6$ wt% MgO could be delivered depending on the mass of a late impactor.

O'Rourke and Stevenson (2016) estimated 0.5 wt% Mg in the core for a single stage model with equilibration at 3500 K while a 2-stage model with second equilibration at higher T permitted up to 2 wt% Mg in the core. Recently Helffrich et al. (2020) estimated that 0.3 wt% Mg could be delivered via single-stage core formation. The initial BMO composition is also hard to constrain. Andrault et al. (2017) conclude that deep mantle melts near the eutectic temperature may have had compositions similar to pyrolite, i.e. 40 mol% SiO_2, 50 mol% MgO and 10 mol% FeO (Eggins et al., 1998). Caracas et al. (2019) calculate a change in melt composition between 0 and 30% melt fraction of 10 mol% SiO_2, 5 mol% MgO and 37 mol% FeO.

2.2. Core Temperature and Energy Balance

The temperature at the inner core boundary is obtained from the melting point of pure iron, T_{m}^{Fe}, depressed by an amount ΔT to account for the presence of impurities. In this work we take $T_{\mathrm{m}}^{Fe} = 6360$ K from the *ab initio* study of Alfè et al. (2002a), which is consistent with the experimental results of Anzellini et al. (2013), though higher than recent estimates of 5500 K from Sinmyo et al. (2019). The gradient of the melting curve, $\mathrm{d}T_{\mathrm{m}}^{Fe}/\mathrm{d}P$ is more important for thermal history calculations, which is more consistent between the Sinmyo et al. (2019) and Anzellini et al. (2013) studies when accounting for uncertainties in extrapolating the experimental results to ICB pressure.

The effect of impurities on T_{m} is clearly hard to constrain given current uncertainties on the core composition. Here we employ the linear melting point depression derived by Alfè et al. (2002a) using a truncated expansion of the chemical potentials at ICB conditions. The total ΔT is assumed to be a linear combination of the values for O and Si (ignoring any effect from Mg).

The adiabatic temperature gradient is given by

$$\frac{\partial T_{\mathrm{a}}}{\partial r} = -\frac{\alpha_{\mathrm{T}} g T_{\mathrm{a}}}{C_p}. \tag{4}$$

T_{a} is anchored to T_{m} at the ICB and calculated as a function of radius using the values of the thermal expansion coefficient α_{T} and specific heat capacity C_p quoted in Gubbins et al. (2003) and reported in Table 2. Gubbins et al. (2003) noted that cooling on the adiabat is independent of radius to a good approximation such that

$$\frac{\mathrm{D}T_{\mathrm{a}}}{\mathrm{D}t} = \frac{T_{\mathrm{a}}}{T_{\mathrm{c}}}\frac{\mathrm{d}T_{\mathrm{c}}}{\mathrm{d}t}, \tag{5}$$

where subscripts i and c denote the ICB and CMB respectively. The power Q_{s} released by heat stored in the core in the core can then be written

$$Q_{\mathrm{s}} = C_p \frac{T_{\mathrm{i}}}{T_{\mathrm{c}}}\frac{\mathrm{d}T_{\mathrm{c}}}{\mathrm{d}t}\int \rho T_{\mathrm{a}} \mathrm{d}V. \tag{6}$$

The rate of growth of the inner core is give by

$$\frac{\mathrm{d}r_{\mathrm{i}}}{\mathrm{d}t} = \frac{1}{(\mathrm{d}T_m/\mathrm{d}P)_{r=r_{\mathrm{i}}} - (\partial T_{\mathrm{a}}/\partial P)_{r=r_{\mathrm{i}}}}\frac{1}{\rho(r_{\mathrm{i}})g(r_{\mathrm{i}})}\frac{T_{\mathrm{i}}}{T_{\mathrm{c}}}\frac{\mathrm{d}T_{\mathrm{c}}}{\mathrm{d}t}, \tag{7}$$

(Gubbins et al., 2003), which together with the latent heat coefficient L defines the total heat released by latent heat at the ICB:

$$Q_{\mathrm{L}} = 4\pi r_{\mathrm{i}}^2 \rho(r_{\mathrm{i}}) L \frac{\mathrm{d}r_{\mathrm{i}}}{\mathrm{d}t}. \tag{8}$$

Using mass balance, the rate of change of light element fraction in the core is also related to the ICB growth rate by

$$\frac{\mathrm{D}w_i^l}{\mathrm{D}t} = \frac{4\pi r_\mathrm{i}^2 \rho(r_\mathrm{i})}{M_\mathrm{oc}} \left(w_i^l - w_i^s\right) \frac{\mathrm{d}r_\mathrm{i}}{\mathrm{d}t}, \tag{9}$$

(Gubbins et al., 2004), where M_oc is the mass of the outer core and the superscripts l and s here define quantities in the liquid and solid cores respectively. The gravitational energy release due to light elements mixing the core is

$$Q_\mathrm{g} = \int \rho \psi \alpha_i^\mathrm{c} \frac{\mathrm{D}w_i^l}{\mathrm{D}t} \mathrm{d}V \tag{10}$$

(Gubbins et al., 2004), where ψ is the gravitational potential.

Together with the power Q_p produced by precipitation (defined precisely below), Q_s, Q_L and Q_g are the dominant terms in the core energy balance. It is therefore appropriate to write the total core energy balance as

$$Q^\mathrm{c} = Q_\mathrm{s} + Q_\mathrm{L} + Q_\mathrm{g} + Q_\mathrm{p} = A \frac{\mathrm{d}T_\mathrm{c}}{\mathrm{d}t} \tag{11}$$

(Gubbins et al., 2004; Nimmo, 2015b), where A represents integrals over core properties that can be calculated from Table 2. Equation (11) is the basis of the core-mantle interaction model developed by Greenwood et al. (2021) that is used frequently below.

2.3. Core thermal conductivity

A detailed comparison of different methodologies for determining k is both beyond the scope of this article and the expertise of the authors and so we refer the reader to Williams (2018), Zhang et al. (2020) and Pourovskii et al. (2020) for recent discussions. We consider experimental studies comprising direct determinations of k

in hcp iron (Konôpková et al., 2016) and solid Fe-Si alloys (Hsieh et al., 2020) and inferences of k based on measured electrical conductivity σ of hcp iron (Ohta et al., 2016; Xu et al., 2018; Zhang et al., 2020) and hcp Fe-Si alloys (Inoue et al., 2020) using the Wiedemann-Franz Law

$$k = LT\sigma, \tag{12}$$

where L is the Lorenz number. Equation (12) assumes that free electrons are predominantly scattered elastically by phonons; in the case of perfect scattering L takes the Sommerfeld value of $L = L_0 = 2.44 \times 10^{-8}$ W Ω K^{-2} (e.g. Secco, 2017). Recent computational studies also include inferences of k from the Wiedemann-Franz law (Xu et al., 2018) as well as direct determinations of k in liquid iron (Pozzo et al., 2012; de Koker et al., 2012; Pozzo and Alfè, 2016) and iron alloys (Pozzo et al., 2013; de Koker et al., 2012).

Figure 1 shows k values obtained directly (top) and inferred from the Wiedemann-Franz law (bottom) at the $P - T$ conditions reported in the above studies, i.e. without extrapolation to core conditions. Only selected high $P - T$ results are shown and so the $P - T$ trends obtained by individual studies are not represented. When comparing the various data, several factors need to be taken into account. Increases in k arise from increasing pressure and temperature. Decreasing k arises from the solid-liquid transition, presence of impurities, the effect of electron-electron scattering (for calculations), and a non-ideal value of L (for electrical conductivity measurements). We consider each of these factors in turn:

Pressure: Pozzo and Alfè (2016) provide the pressure-dependence of electrical conductivity of pure iron at 4350 K. Inoue et al. (2020) show P-dependence of a 4 wt% Si alloy at 300 K and also at the similar temperatures of 1570 K and 1650 K.

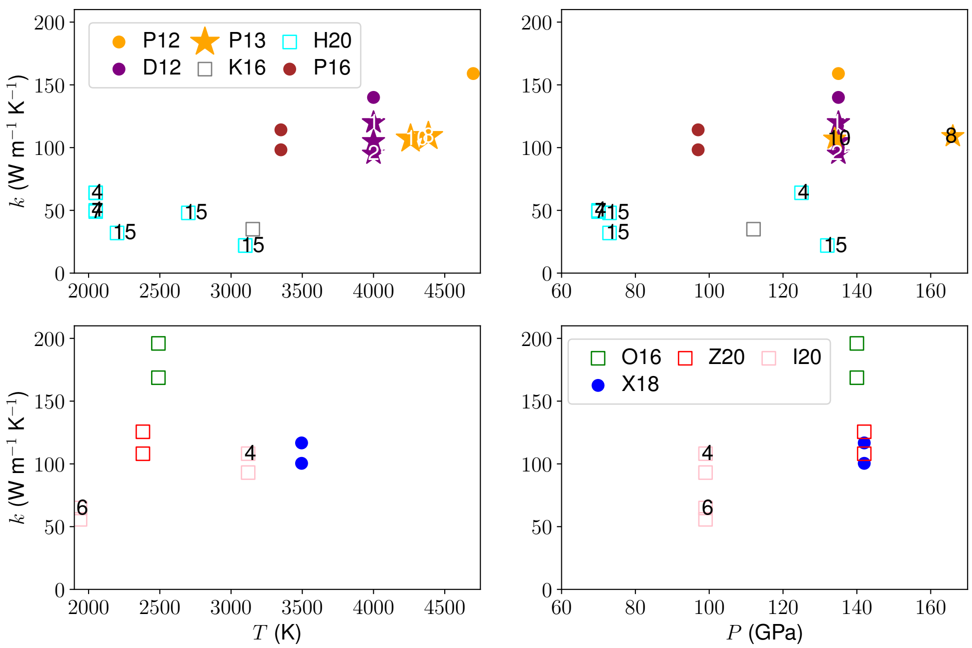

Figure 1: Summary of recent studies of core thermal conductivity k. The top row shows direct determinations of k while the bottom row shows inferences of k using electrical conductivity and the Wiedemann-Franz law. Left column shows the dependence on temperature T at the pressure P shown in the right column. Colours distinguish studies: open/closed symbols denote the method employed (experiment, calculation); shape denotes the material (square=solid, circle=liquid), stars distinguish alloys with the Si molar concentration denoted as a number inside the symbol. The considered studies are: P12 (Pozzo et al., 2012); D12 (de Koker et al., 2012); P13 (Pozzo et al., 2013); K16 (Konôpková et al., 2016); O16 (Ohta et al., 2016); P16 (Pozzo and Alfè, 2016); X18 (Xu et al., 2018); Z20 (Zhang et al., 2020); I20 (Inoue et al., 2020); H20 (Hsieh et al., 2020).

Converting to k values using equation (12) with $L = L_0$ yields mean $\mathrm{d}k/\mathrm{d}P$ values of 0.4 W m^{-1} K^{-1} GPa^{-1} for Pozzo and Alfè (2016) and 0.13 W m^{-1} K^{-1} GPa^{-1} and 0.5 W m^{-1} K^{-1} GPa^{-1} for Inoue et al. (2020) corresponding to an increase in k of 15−20 W m^{-1} K^{-1} from 95 GPa to 135 GPa. We use $\mathrm{d}k/\mathrm{d}P = 0.4$ W m^{-1} K^{-1} GPa^{-1} below.

Temperature: The expected T behaviour depends critically on the validity of equation (12) and the role of saturation effects (Konôpková et al., 2016; Pozzo and Alfè, 2016). In the absence of saturation, the Bloch-Grüneisen formula predicts that the electrical conductivity due to electron-phonon scattering varies as T^{-1} at high T, and hence $k = L \sim$ constant according to equation (12). Saturation can arise at high T when the electron mean free path becomes comparable to the inter-atomic distance, at which point σ stops decreasing with temperature and equation (12) predicts that k increases with T. The relevance of saturation to Earth's core properties was first recognised by Gomi et al. (2013) and has been observed by Pozzo and Alfè (2016) and Inoue et al. (2020), though not by Zhang et al. (2020). As a simple estimate of $\mathrm{d}k/\mathrm{d}T$ we use the results from de Koker et al. (2012), who found $\mathrm{d}k/\mathrm{d}T \approx 0.01$ W m^{-1} K^{-1} K^{-1} for FeO_3 at 135 GPa and $\mathrm{d}k/\mathrm{d}T \approx 0.02$ W m^{-1} K^{-1} K^{-1} for FeO_7 in the pressure range $130 - 160$ GPa. In order to produce a conservative increase in k we adopt $\mathrm{d}k/\mathrm{d}T = 0.01$ W m^{-1} K^{-1} K^{-1} below.

Phase transition: Zhang et al. (2020) discuss recent literature and invoke a 10% decrease in σ on melting. Pozzo et al. (2013) find a change in σ of $18-25\%$, which is mainly due to the solid structure, but also contains a contribution from the uneven partitioning of elements at the ICB. We take the value of 18% below since this is roughly halfway between the two extremes.

Impurities: Few studies have systematically compared the effect of different elements on k, but those that have find that the identity of the impurity is of secondary importance compared to their abundance as should be expected from relatively insulating impurities acting as disruptions to metallic structure. Inoue et al. (2020) found that up to 6.5 wt% Si could reduce k by $10-20\%$ while de Koker et al. (2012), Pozzo et al. (2013) and Zhang et al. (2020) found that various combinations of Si and O could reduce k by up to 30%. The recent work by Hsieh et al. (2020) suggests that the effect could be much more severe if there is a high Si concentration in the core. Here we assume a 20% reduction.

Electron-electron scattering (EES) and non-ideal L: EES can reduce both the k calculated from classical density functional theory (Pozzo et al., 2013; de Koker et al., 2012) and the L in equation (12) below the ideal value L_0. At high $P-T$ for hcp iron Zhang et al. (2020) find a 20% decrease in σ due to EES and estimate $L \approx 2.0-2.1\times10^{-8}$ W Ω K^{-2}, while Pourovskii et al. (2020) obtain a 20% decrease in k for bcc and hcp iron and estimate $L = 2.28\times10^{-8}$ W Ω K^{-2} at ICB conditions. de Koker et al. (2012) also obtain $L \approx 1.8 - 2.4 \times 10^{-8}$ W Ω K^{-2} without EES, indicating non-negligible inelastic scattering effects. In view of the current uncertainty we use $L = L_0$ and $L = 2.1 \times 10^{-8}$ W Ω K^{-2} and adopt a 20% drop in k due to EES.

Figure 2 shows the extrapolated values of k for the studies in Figure 2. The majority of values fit within the range $70 \leq k \leq 110$ W m^{-1} K^{-1}. Notable outliers are the extrapolations from direct conductivity measurements for the pure hcp (Konôpková et al., 2016) and Si-rich Fe-Si solid (Hsieh et al., 2020). Future work is needed to understand the reasons for this, and to better constrain the extrapolation, which is subject to significant uncertainties as discussed above. For the rest of this article we focus on two values of conductivity: $k = 70$ W m^{-1} K^{-1} and $k = 100$ W m^{-1} K^{-1} as suggested by Figure 2. As such we will henceforth focus on the "high conductivity" scenario in Table 1.

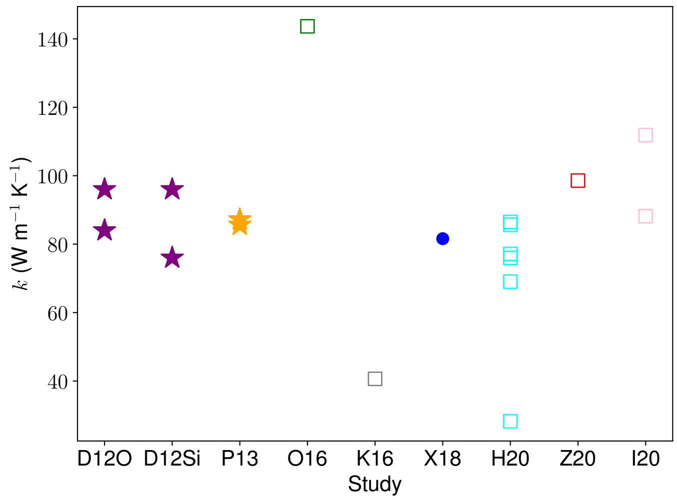

Figure 2: Extrapolation of k values in Figure 1 to CMB pressure of 135 GPa and temperature of 4000 K. The symbol styles are the same as in Figure 1.

3. Mass Transfer at the CMB

In general the chemical compositions of material in contact at the CMB will differ from the bulk compositions of the core and mantle, which gives rise to a chemical flux given by equation (3). The process of mass transfer at the CMB therefore depends on the chemical compositions of the core and mantle, both in the bulk and on either side of the CMB. Since we are primarily interested in the "high conductivity" scenario (see Table 1) we will focus on the interaction between the core and silicate melts in a basal magma ocean. This scenario is expected to yield greater chemical exchange than the interaction between the core and solid mantle because the significant increase in diffusion coefficient between solid mantle and BMO overwhelms any potential reduction in partition coefficient due to entropic effects in the melt (Pozzo et al., 2019).

Elements are usually assumed to be well-mixed by vigorous convection in the proto-core (e.g. Rubie et al., 2015a), though it is possible that a stratified layer developed near the end of core formation (Landeau et al., 2016; Jacobson et al., 2017) as discussed in Section 4.4. Self diffusion coefficients of O and Si in the liquid are very small (see Pozzo et al., 2013, and Table 2) and so chemical diffusion in a primordial stratified layer was probably too slow to produce significant time variations in the bulk composition. An early BMO was also presumably well-mixed (Solomatov, 2015); however, its bulk composition could evolve over time. In the simple case of fractional crystallisation the melt should become depleted in MgO and enriched in FeO as the ocean shrinks (Labrosse et al., 2007; Caracas et al., 2019). However, different scenarios for BMO evolution, such as compaction of an Fe-depleted mush layer, could produce alternative compositional evolution. Therefore, the distinction between precipitation and stratification scenarios depends primarily on the compositional evolution of a BMO and interactions at the CMB.

Chemical stratification of the upper core can arise when the equilibrium concentration of an element i at the CMB exceeds its bulk concentration. The flux I_i is negative and light element enters the core. Precipitation arises when the equilibrium concentration of i falls below the bulk concentration; I_i is positive and light element leaves the liquid. In this case the lowest energy configuration (corresponding to equality of the chemical potentials) is the co-existence of liquid with a solid phase, usually assumed to be an oxide of the supersaturated element. If precipitation arises at the CMB then the oxide, which is lighter than the bulk core liquid, will underplate onto the CMB, leaving behind a residual liquid at the top of the core that is depleted in light element and hence denser than the core fluid below. Owing to the low viscosity of the core, the dense residual liquid will rapidly sink via a Rayleigh-Taylor instability, presumably mixing throughout the core. The gravitational energy released by precipitation of element i is

$$Q_p = \int \rho\psi\alpha_i^{\mathrm{c}}\frac{\mathrm{d}w_i^{\mathrm{c}}}{\mathrm{d}t}\mathrm{d}V \approx \int \rho\psi\alpha_i^{\mathrm{c}}\frac{\mathrm{d}w_i^{\mathrm{c}}}{\mathrm{d}T}\frac{\mathrm{d}T}{\mathrm{d}t}\mathrm{d}V, \tag{13}$$

where V is the liquid core volume. The primary quantities of interest are therefore w_i^{c}, which is critical for determining the onset and evolution of stratification/precipitation, and $\mathrm{d}w_i^{\mathrm{c}}/\mathrm{d}T$, which determines the power released by precipitation. w_i^{c} and $\mathrm{d}w_i^{\mathrm{c}}/\mathrm{d}T$ are obtained from the equilibrium conditions at the CMB.

In this section we first present the calculation of equilibrium conditions at the CMB. The results will show that the fluxes I_i vary between elements i and also vary over time for a given element. Moreover, the flux of a given element depends not only on pressure P and temperature T but also on the abundance of other elements. We demonstrate the case of precipitation ($I_i > 0$) for MgO partitioning and stratification ($I_i < 0$) for FeO partitioning in isolation. Finally, we consider the coupled equilibrium conditions for MgO, FeO and SiO_2.

3.1. Chemical Equilibrium at the CMB

Departures from chemical equilibrium for materials in contact at the CMB should be very small since the timescale for diffusion is very short over such small length-scales. Chemical equilibrium at the CMB requires equality of chemical potentials μ_i for each species i, while mass conservation (ignoring thermal contraction of the core) implies that the total flux of mass from the mantle I_i equals the mass added to the core (Braginsky and Roberts, 1995; Davies et al., 2020). These conditions can be written

$$
\begin{aligned}
\mu_1^m(P,T,c_1^m,\dots,c_{N^{\mathrm{m}}}^m) &= \mu_2^c(P,T,c_1^c,\dots,c_{N^{\mathrm{c}}}^c),\\
\mu_2^m(P,T,c_1^m,\dots,c_{N^{\mathrm{m}}}^m) &= \mu_2^c(P,T,c_1^c,\dots,c_{N^{\mathrm{c}}}^c),\\
&\dots\\
\mu_{N^{\mathrm{m}}}^m(P,T,c_1^m,\dots,c_{N^{\mathrm{m}}}^m) &= \mu_{N^{\mathrm{c}}}^c(P,T,c_1^c,\dots,c_{N^{\mathrm{c}}}^c); \qquad (14)\\
I_1^m(P,T,c_1^m,\dots,c_{N^{\mathrm{m}}}^m) &= I_2^c(P,T,c_1^c,\dots,c_{N^{\mathrm{c}}}^c),\\
I_2^m(P,T,c_1^m,\dots,c_{N^{\mathrm{m}}}^m) &= I_2^c(P,T,c_1^c,\dots,c_{N^{\mathrm{c}}}^c),\\
&\dots\\
I_{N^{\mathrm{m}}}^m(P,T,c_1^m,\dots,c_{N^{\mathrm{m}}}^m) &= I_{N^{\mathrm{c}}}^c(P,T,c_1^c,\dots,c_{N^{\mathrm{c}}}^c). \qquad (15)
\end{aligned}
$$

where superscripts m and c denote the mantle and core respectively, $i, = 1, ..., N^{\mathrm{m}}$ and $j = 1, ..., N^{\mathrm{c}}$ represent the number of chemical species in the mantle and core respectively and c_i denotes the mole fraction of species i. Here the pressure and temperature correspond to conditions at the CMB. Note that equation (15) does not imply equality of the chemical compositions.

The key quantity for determining equilibrium conditions at the CMB is the equilibrium constant K, which is defined as

$$
K = \frac{\prod_i a_i}{\prod_j a_j} = \frac{\prod_i c_i}{\prod_j c_j} \cdot \frac{\prod_i \gamma_i}{\prod_j \gamma_j} = K_d \cdot \frac{\prod_i \gamma_i}{\prod_j \gamma_j}, \qquad (16)
$$

where K_d is the distribution coefficient, $a_i = c_i \gamma_i$ are the activities and γ_i are the activity coefficients. Here the i denotes the products that appear on the right side of the reaction and j denotes the reactants. At equilibrium K is related to the Gibbs free energy change across the reaction ΔG_r by

$$K = \exp\left(-\frac{\Delta G_r}{k_B T}\right) = \exp\left(-\frac{\Delta H_r - T\Delta S_r + P\Delta V_r}{k_B T}\right), \tag{17}$$

where k_B is the Boltzmann constant and ΔH_r, ΔS_r and ΔV_r, are respectively the standard state change in enthalpy, entropy and volume across the reaction. Equation (17) is usually written as

$$\log K_d = a + \frac{b}{T} + c\frac{P}{T} - \sum_i (\log \gamma_i) + \sum_j (\log \gamma_j), \tag{18}$$

where the coefficients a, b, c and γ_i are to be determined from recovered phases that are analysed at known $P - T-$composition conditions. Note for consistency with previous work we have retained the notation for the coefficient c, which should not be confused with mole fraction.

Computer simulations can be used to calculate chemical potentials for each species (e.g. Alfè et al., 2002b; Pozzo et al., 2019) and hence the equilibrium concentrations can be obtained directly from equations (14). Separating out the configurational part of the chemical potential, i.e. $\mu_i = k_B T \ln c_i + \tilde{\mu}_i$, the equilibrium becomes

$$\sum_i \left[k_B T \ln c_i^m + \tilde{\mu}_i^m\right] = \sum_j \left[k_B T \ln c_j^c + \tilde{\mu}_j^c\right], \tag{19}$$

or

$$k_B T \ln\left[\frac{\prod_j c_j^c}{\prod_i c_i^m}\right] = k_B T \ln K_d = \sum_i \tilde{\mu}_i^m - \sum_j \tilde{\mu}_j^c, \tag{20}$$

(Davies et al., 2018; Pozzo et al., 2019). Since the chemical potentials are completely determined, this formulation can be shown to be equivalent to equation (17) by separating the chemical potentials as $\mu_i = \mu_i^0 + k_B T \ln Y_i$, where μ_i^0 is the value of μ_i

in standard state.

The form of K (and K_d) is determined by the nature of the chemical reaction. The reactions that have generally been considered in the literature are dissolution, dissociation and exchange (e.g. Badro et al., 2018). These are summarised in Table 3. In principle numerical simulations could be used to distinguish between the different possibilities, however the simulation sizes required to obtain meaningful concentrations have traditionally been prohibitively costly in *ab initio* calculations. Another approach is to compare large datasets against the predictions from equation (18), which has been done recently for MgO by Badro et al. (2018). We reproduce the workflow of Badro et al. (2018) below to demonstrate the steps involved in obtaining equilibrium concentrations and precipitation rates and to provide a consistent framework with which to compare recent studies. Compositional variations in silicate activity coefficients are neglected and hence the γ_j^m can be absorbed into the parameters a and b; the γ_i below therefore refer to the metal. Silicate activities can be included in the modelling (Frost et al., 2010; Helffrich et al., 2020), but at the expense of introducing more fitting parameters.

3.2. Partitioning of MgO at the CMB

The equations determining $\log K_d$ for MgO dissolution, dissociation and exchange are respectively

$$\log \frac{c^c_{MgO}}{c^m_{MgO}} = \log K^{\mathrm{MgO}}_{dl} = a + \frac{b}{T} + c\frac{P}{T} - \log \gamma^c_{Mg} - \log \gamma^c_{O}, \tag{21}$$

$$\log \frac{c^c_{Mg} c^c_{O}}{c^m_{MgO}} = \log K^{\mathrm{MgO}}_{dc} = a + \frac{b}{T} + c\frac{P}{T} - \log \gamma^c_{Mg} - \log \gamma^c_{O}, \tag{22}$$

$$\log \frac{c^c_{Mg} c^m_{FeO}}{c^c_{Fe} c^m_{MgO}} = \log K^{\mathrm{MgO}}_{e} = a + \frac{b}{T} + c\frac{P}{T} - \log \gamma^c_{Mg} + \log \gamma^c_{Fe}. \tag{23}$$

Reaction	K_d	Ref
$\mathrm{MgO^m} \iff \mathrm{Mg^c} + \mathrm{O^c}$	$\frac{c^c_{Mg} c^c_O}{c^m_{MgO}}$	B16 B18 M20 H20
$\mathrm{MgO^m} \iff \mathrm{MgO^c}$	$\frac{c^c_{MgO}}{c^m_{MgO}}$	B18
$\mathrm{MgO^m} + \mathrm{Fe^c} \iff \mathrm{FeO^m} + \mathrm{Mg^c}$	$\frac{c^m_{FeO}}{c^c_{Fe}} \frac{c^c_{Mg}}{c^m_{MgO}}$	OS16, D17, D19
$2\mathrm{MgO^m} + \mathrm{Si^c} \iff \mathrm{SiO_2^m} + 2\mathrm{Mg^c}$	$\frac{c^m_{SiO_2}}{c^c_{Si}} \frac{(c^c_{Mg})^2}{(c^m_{MgO})^2}$	H20
$\mathrm{FeO^m} \iff \mathrm{Fe^c} + \mathrm{O^c}$	$\frac{c^c_{Fe} c^c_O}{c^m_{FeO}}$	F10 OS16 D18 M20 F15
$\mathrm{SiO_2^m} \iff \mathrm{Si^c} + 2\mathrm{O^c}$	$\frac{c^c_{Si} (c^c_O)^2}{c^m_{SiO_2}}$	H17 M20 H20
$\mathrm{SiO_2^m} \iff \mathrm{SiO_2^c}$	$\frac{c^c_{SiO_2}}{c^m_{SiO_2}}$	
$\mathrm{SiO_2^m} + 2\mathrm{Fe^c} \iff 2\mathrm{FeO^m} + \mathrm{Si^c}$	$\frac{(c^m_{FeO})^2}{(c^c_{Fe})^2} \frac{c^c_{Si}}{c^m_{SiO2}}$	OS16, F15

Table 3: Summary of chemical reactions between MgO, SiO_2, FeO and metallic alloys considered in recent literature. The cited studies are Badro et al. (2016, B16), Badro et al. (2018, B18), Du et al. (2017, D17), Du et al. (2019, D19), Fischer et al. (2015, F15), Frost et al. (2010, F10), Helffrich et al. (2020, H20), Hirose et al. (2017, H17), Mittal et al. (2020, M20), and O'Rourke and Stevenson (2016, O16).

Equations (21)–(23) are evaluated using the values of a, b and c reported in several previous studies and reproduced in Table 4. When accounting for compositional effects O'Rourke and Stevenson (2016) set all activity coefficients to 1, Du et al. (2019) model the effect of O and Si, while Badro et al. (2018) consider interactions between O, Si, Mg, C, and S. Figure 3 shows K_{dl}^{MgO} and K_e^{MgO} calculated for MgO dissociation and exchange reactions using the Badro et al. (2018) dataset. It is clear that accounting for the composition-dependence of partitioning via the activity coefficients, specifically oxygen and magnesium content of the metal, produces a significant reduction in data scatter. The importance of oxygen content was noted by Du et al. (2017), while the composition-dependence on joint solubility of Si, Mg and O is clearly demonstrated in Helffrich et al. (2020).

The γ_i^c are quite sensitive to the values of the parameters ϵ_i^j, which describe the interaction between elements i and j in the liquid (e.g. Badro et al., 2018). For ease

Study	Reaction	a_{Mg}	b_{Mg}	c_{Mg}
O16	e	0.1	-10851	0
B16	dl	1.23	-18816	0
B18	ds	0.1	-14054	0
B18	e	1.06	-12842	0
D19	e	-3.0	-2314	26
		a_O	b_O	c_O
O16	e	0.6	-3800	22
M20	ds	-0.3	0.0	-36.8
		a_{Si}	b_{Si}	c_{Si}
O16	e	1.3	-13500	0
M20		See text		

Table 4: Values of the constant parameters used in this study to fit empirically determined distribution coefficients. The sections show from top to bottom Mg, O and Si. For O and Si the values denoted by O16 (O'Rourke and Stevenson, 2016) were obtained from Fischer et al. (2015), while the values for Mg were estimated from experiments in Takafuji et al. (2005). For Mittal et al. (2020, M20) the values for O come from Hirose et al. (2017). Abbreviations 'e', 'ds' and 'dl' denote exchange, dissociation and dissolution reactions and are used as superscripts in the text.

of comparison these parameters are listed in Table 5 from the studies of Badro et al. (2018), Fischer et al. (2015) and Liu et al. (2020). Overall there is general consistency between the three studies, though with some notable exceptions such as $\epsilon_{\mathrm{Si}}^{\mathrm{Si}}$ and $\epsilon_{\mathrm{O}}^{\mathrm{C}}$. We test the effect by conducting two calculations that use the same parameters as in Figure 3 and differ only by using the ϵ_i^j values of Liu et al. (2020) in place of the respective values from Badro et al. (2018). At 6000 K we obtain $\gamma_O^c = 4.125$, $\gamma_{Mg}^c = 0.74$ and $w_{Mg}^c = 1.1$ for Badro et al. (2018) and $\gamma_O^c = 3.40$, $\gamma_{Mg}^c = 0.61$ and $w_{Mg}^c = 1.78$ for Liu et al. (2020); at 4200 K we obtain $\gamma_O^c = 1.20$, $\gamma_{Mg}^c = 0.65$ and $w_{Mg}^c = 0.52$ for Badro et al. (2018) and $\gamma_O^c = 0.91$, $\gamma_{Mg}^c = 0.50$ and $w_{Mg}^c = 0.96$ for Liu et al. (2020). This calculation is not entirely self-consistent because the γ_i^c are fit to the data alongside the values of a, b and c and are therefore not independent; nevertheless, it does show the that uncertainties in the γ_i^c could propagate into a $\sim$30 $-$ 40% change in the predicted equilibrium concentration.

ϵ_i^j	B18	F15	L20
$\epsilon_{\mathrm{O}}^{\mathrm{O}}$	-1.0	-7.0	-5.8
$\epsilon_{\mathrm{Si}}^{\mathrm{Si}}$	12.4	0.0	0.0
$\epsilon_{\mathrm{Mg}}^{\mathrm{Mg}}$	0.0	–	0.0
$\epsilon_{\mathrm{C}}^{\mathrm{C}}$	12.8	–	–
$\epsilon_{\mathrm{S}}^{\mathrm{S}}$	-5.7	–	–
$\epsilon_{\mathrm{O}}^{\mathrm{Si}}$	-5.0	-7.0	-8.3
$\epsilon_{\mathrm{O}}^{\mathrm{C}}$	-20.0	8.0	–
$\epsilon_{\mathrm{O}}^{\mathrm{S}}$	-17.1	–	–
$\epsilon_{\mathrm{O}}^{\mathrm{Mg}}$	-12.2	–	-16.4
$\epsilon_{\mathrm{S}}^{\mathrm{Si}}$	9.0	–	–
$\epsilon_{\mathrm{S}}^{\mathrm{C}}$	4.9	–	–
$\epsilon_{\mathrm{Si}}^{\mathrm{Mg}}$	4.4	–	0.0
$\epsilon_{\mathrm{S}}^{\mathrm{Mg}}$	13.8	–	–
$\epsilon_{\mathrm{C}}^{\mathrm{Mg}}$	24.3	–	–
$\epsilon_{\mathrm{C}}^{\mathrm{Si}}$	3.6	–	–

Table 5: Comparison of values for the interaction parameters ϵ_i^j between element i and j in liquid iron used in the studies of Badro et al. (2018, B18), Fischer et al. (2015, F15) and Liu et al. (2020, L20). The B18 values correspond to the dissolution reaction.

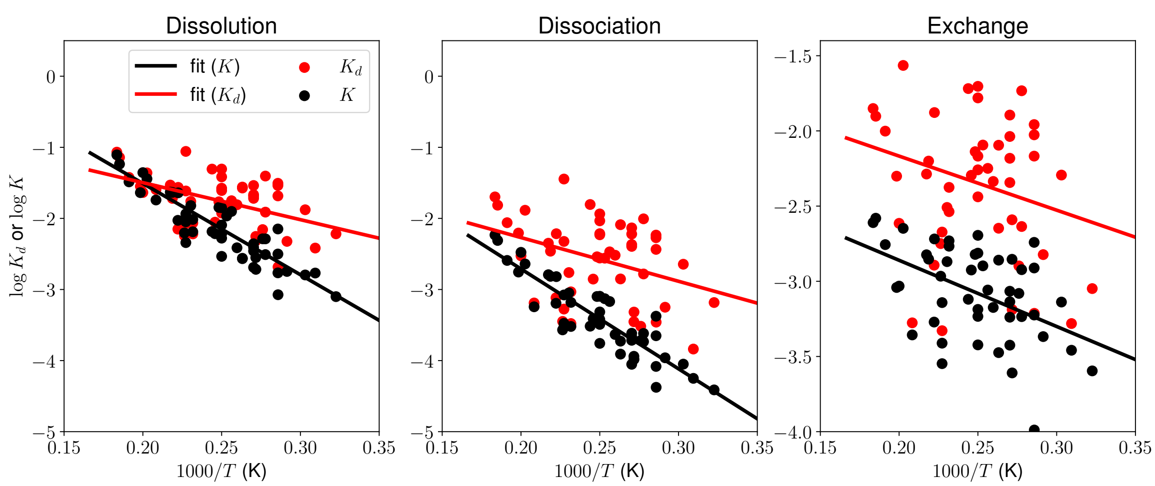

Figure 3: Calculated equilibrium constants for MgO dissolution (left), dissociation (centre) and exchange (right) reactions using the dataset in Badro et al. (2018, Table S1). Red points show $K = K_d$, i.e. with all activity coefficients set to one, while black points show K values calculated using the methodology of Badro et al. (2018) and data in their Table S2. Black and red lines are fits to the respectively datasets using Equations (21)–(23).

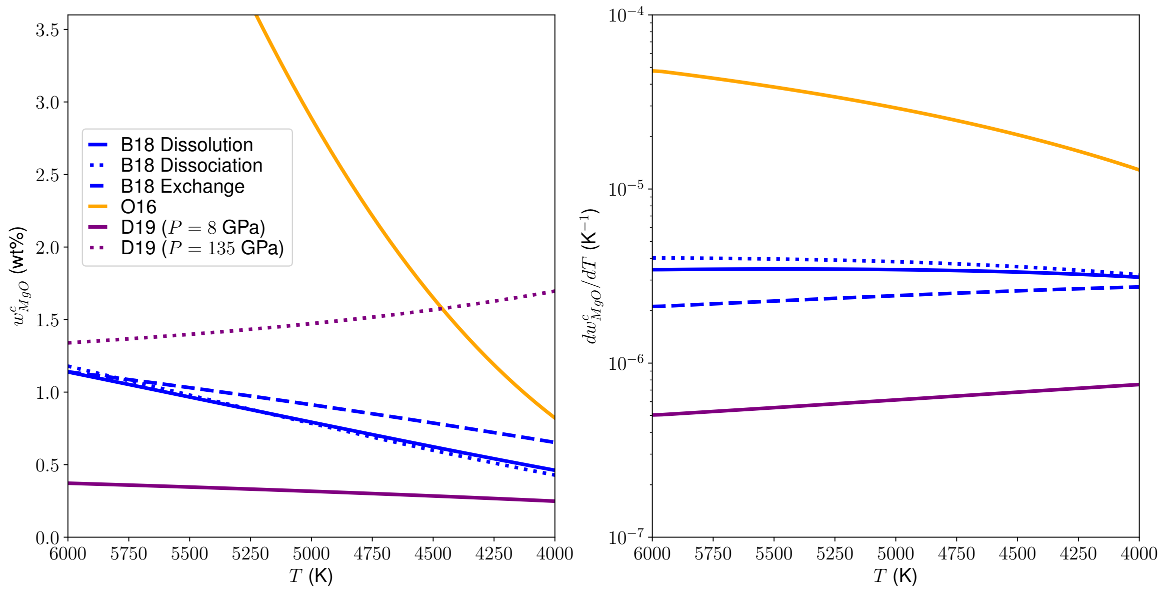

Figure 4: Equilibrium mass fraction of MgO (left) and precipitation rate $\mathrm{d}w^c_{MgO}/\mathrm{d}T$ for a constant core composition of 3 wt% O and 3 wt% Si and a constant BMO composition of 50 mol% MgO and 10 mol% FeO. Considered studies are O'Rourke and Stevenson (2016, O16), Badro et al. (2018, B18) and Du et al. (2019, D19).

In order to compare results from different assumed reactions and modelling strategies Figure 4 shows the core weight fraction of MgO, w^c_{MgO}, vs temperature. We consider the same compositions as Badro et al. (2018): a constant 3 wt% O and 3 wt% Si in the core and 50 mol% MgO in the mantle. Using the Badro et al. (2018) method and dataset the dissociation and dissolution reactions produce almost identical results while all three reactions yield similar $\mathrm{d}w^c_{MgO}/\mathrm{d}T$ as found by Du et al. (2019), though the exchange reaction yields a worse fit to their data (see Badro et al., 2018, and Figure 3). O'Rourke and Stevenson (2016) obtain a much larger equilibrium concentration and $\mathrm{d}w^c_{MgO}/\mathrm{d}T$ than the more recent studies that include composition-dependence on the equilibrium conditions. This result underscores the importance of accounting for the light element content of the core when modelling precipitation rates.

The pressure-dependence of equilibrium is a critical issue because this governs the depth in the core at which precipitation will commence. Badro et al. (2016), Badro et al. (2018) and Du et al. (2017) find that the K^{MgO} are independent of P and hence precipitation must begin at the CMB. Du et al. (2019) obtained a statistically significant pressure variation for K_e^{MgO}, which has a significant impact on the equilibrium behaviour obtained from their model. Figure 4 shows that at 8 GPa and 10 mol% FeO the equilibrium composition from Du et al. (2019) is almost independent of temperature as advocated in their earlier study (Du et al., 2017). However, when evaluated at CMB pressure this model predicts that precipitation would begin at the lowest temperature, i.e. the present day, and would therefore have been unavailable to provide power to the dynamo in the past.

The equilibrium concentrations in Figure 4 should be compared to the initial Mg content of the core, estimated to lie in the range $0.3 - 3.6$ wt% (Section 2). Taking the higher end of these estimates, all studies in Figure 4 except O'Rourke and Stevenson (2016) predict that the core was over-saturated in Mg for all temperatures below 6000 K; the bulk core Mg content was then higher than the CMB value corresponding to a positive (outward) flux I_{Mg} and the precipitation of MgO from the core. Conversely, using the lowest value, 0.3 wt% Mg, all studies predict that the core was under-saturated in Mg for all temperatures above 4000 K; the bulk core Mg content has then always been lower than the CMB value corresponding to a negative (inward) I_{Mg} and stratification of the uppermost core due to enrichment in Mg. Therefore, for fixed core and mantle compositions, Mg could either dissolve or precipitate at the top of the core within the uncertainties in partitioning behaviour and initial core composition.

Focusing on the precipitation case, Figure 4 shows that the individual modelling approaches and datasets used by different groups result in a spread of MgO precipitation rates $\mathrm{d}w^c_{MgO}/\mathrm{d}T$ that span almost two orders of magnitude. The high values from O'Rourke and Stevenson (2016) are likely due to their assumption that O and Mg activity coefficients could be set to zero, which was reasonable at the time when few experimental data were available. More recent work suggests lower precipitation rates, which correspondingly reduces the efficiency of precipitation as a mechanism for sustaining the ancient geomagnetic field. However, as shown in Section 3.4 below, higher $\mathrm{d}w^c_{MgO}/\mathrm{d}T$ can be obtained when the coupled reaction between MgO, SiO_2 and FeO are considered.

Figure 5 shows MgO precipitation rate as a function of temperature for the dissolution reaction and different constant core and mantle compositions that span the ranges described in Section 2. It is clear that both the core O content and the mantle MgO composition significantly affect $\mathrm{d}w^c_{MgO}/\mathrm{d}T$, which should be taken in the context of the $\sim$40% uncertainties on the calculated equilibrium concentration (Badro et al., 2018). In these calculations the amount of Si in the core has a relatively minor effect; however, this is not the case if an exchange reaction involving MgO and SiO_2 governs the partitioning behaviour of Mg (Helffrich et al., 2020). Interestingly the precipitation rate is almost independent of T in all cases considered. However, this turns out not to be the case when the joint equilibrium of Mg, O and Si is considered in Section 3.4.

3.3. Partitioning of FeO at the CMB

Previous studies have generally modelled FeO transfer using a dissolution reaction with distribution coefficient $K_d^{\mathrm{FeO}} = c^c_{Fe} c^c_O / c^m_{FeO}$. As with Mg, the most significant interaction parameters involve Si and O because of their expected high concentrations in the core. However, Fischer et al. (2015) found that their fitted $\epsilon^{\mathrm{O}}_{\mathrm{Si}}$ and $\epsilon^{\mathrm{O}}_{\mathrm{O}}$ values produced an unstable parameterisation in which partitioning of O into metal would

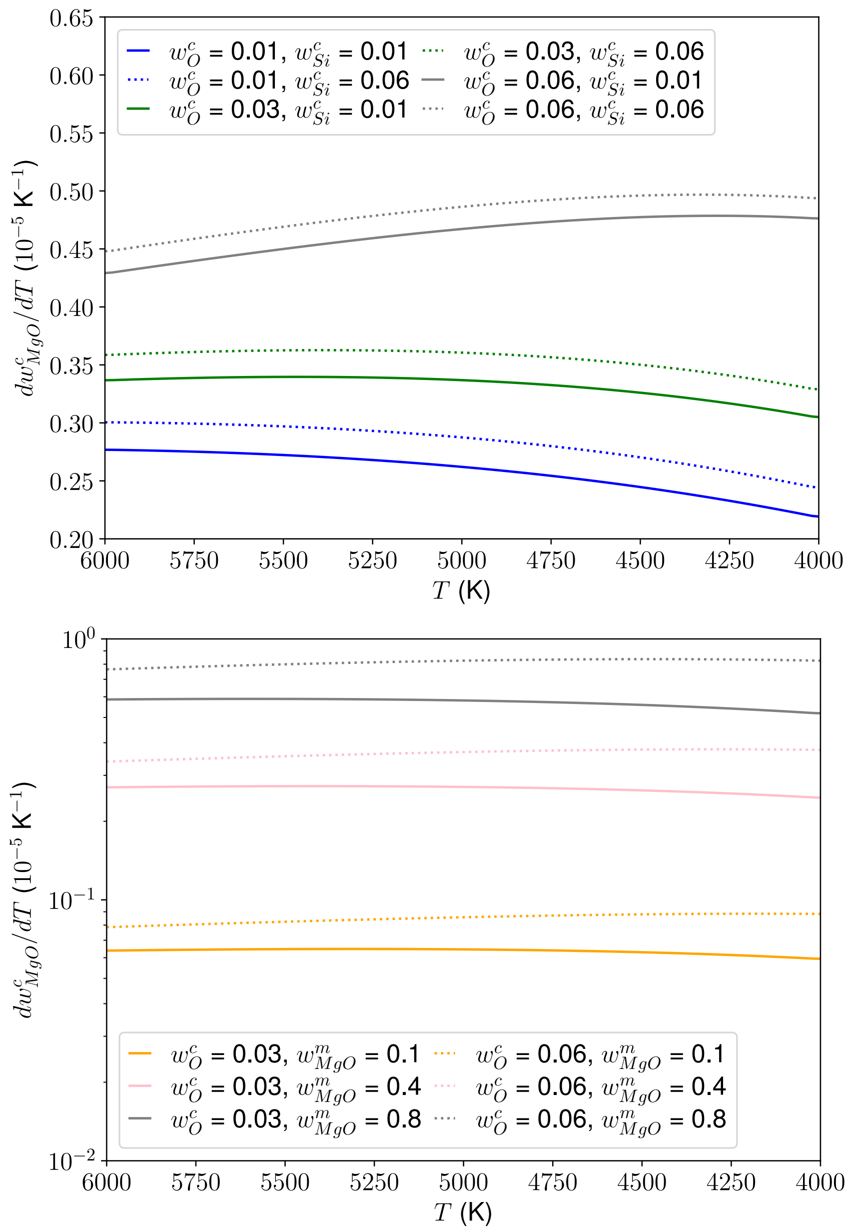

Figure 5: Precipitation rate $\mathrm{d}w^c_{MgO}/\mathrm{d}T$ as a function of temperature T for various starting compositions in the core (top) and BMO (bottom).

cause ever more O and Si to enter the core. Considering the interaction between an Fe-O metal and ferropericlase, Davies et al. (2018) found that K_d^{FeO} is a weak function of oxygen concentration in the range $0 \leq c_O^c \leq 30$ mol%, while adding 7.6 mol% Si to the metal produced a strong increase of K_d^{FeO} with c_O^c, consistent with the findings of Tsuno et al. (2013) and Fischer et al. (2015) for the case of silicate melts. Pozzo et al. (2019) performed first principles molecular dynamics calculations to determine K_d^{FeO} at CMB $P-T$ conditions for a silicate melt comprising 50 mol% SiO_2, 44 mol% MgO, and 6 mol% FeO and a liquid metal comprising 95 mol% Fe and 5 mol% O; however, they were not able to determine the composition-dependence of K_d^{FeO} owing to the large system sizes needed to robustly estimate free energy changes. Here we ignore the composition-dependence on FeO partitioning and focus on K_d^{FeO}, noting that improved constraints by future studies will be very valuable.

Figure 6 shows the temperature and pressure dependence of K_d^{FeO} from a number of recent experimental and computational studies. Davies et al. (2018) have shown that simulations at 134 GPa and 3200 K agree well with experiments at the same conditions with a starting composition consisting of a powdered mixture of pure metal and $Mg_{81}Fe_{19}O$ (Ozawa et al., 2008). Therefore any discrepancy between the two types of study are likely due to differences in the starting compositions and uncertainties in determining exact $P-T$ conditions. These factors produce a scatter of $0.5-1$ log units over much of the moderate T range and are consistent with the differences observed at high T. The results show that K_d^{FeO} increases with both P and T and that O tends to favour the metal as core conditions of $T > 4000$ K are approached.

Figure 7 shows the equilibrium concentration of O in the core for different core and BMO Fe concentrations spanning the ranges discussed in Section 2. Here K_d^{FeO} has been fit using the black line in Figure 6, which yields values on the lower end of the

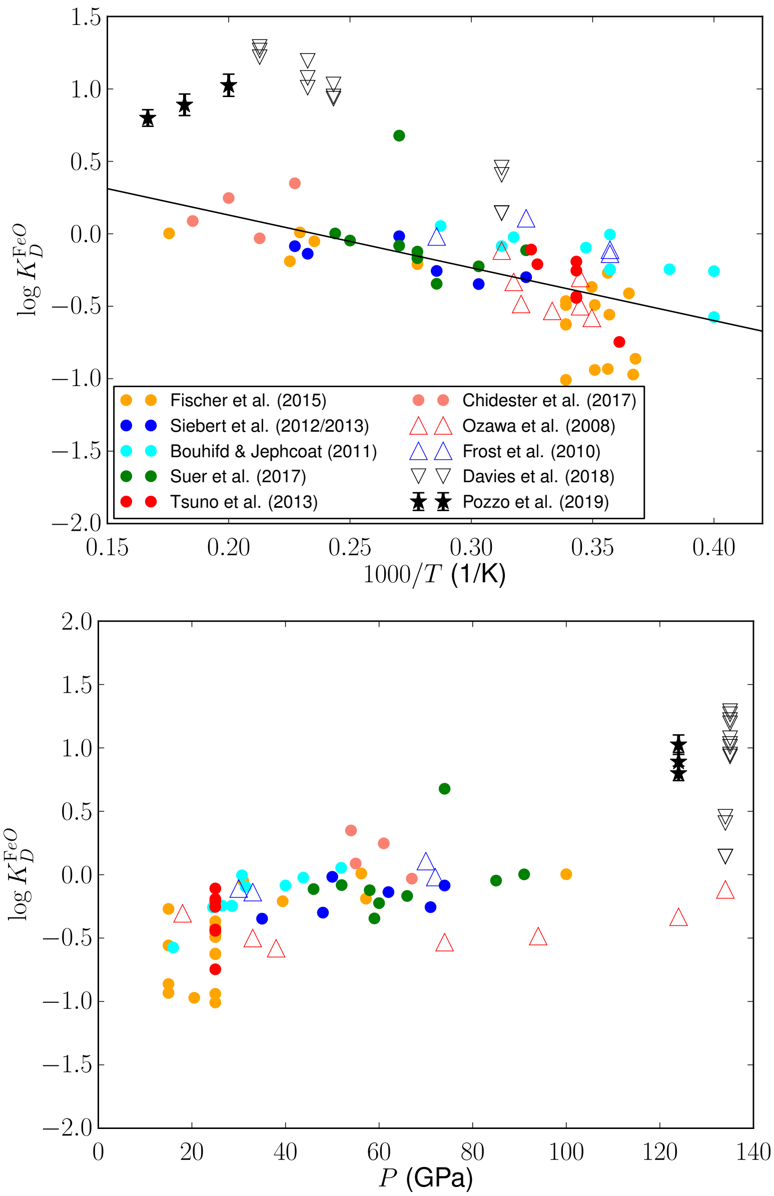

Figure 6: Comparison of published FeO distribution coefficients. Panels show values of the distribution coefficient K_D^{FeO} plotted against inverse temperature (top) and pressure (bottom) for solid-silicate–liquid-metal partitioning (open symbols) and silicate-melt–liquid-metal partitioning (closed symbols). The plotted studies are: Fischer et al. (2015), Siebert et al. (2012), Bouhifd and Jephcoat (2011), Suer et al. (2017), Tsuno et al. (2013), Chidester et al. (2017), Ozawa et al. (2008), Frost et al. (2010), Davies et al. (2018) and Pozzo et al. (2019). Figure adapted from Pozzo et al. (2019).

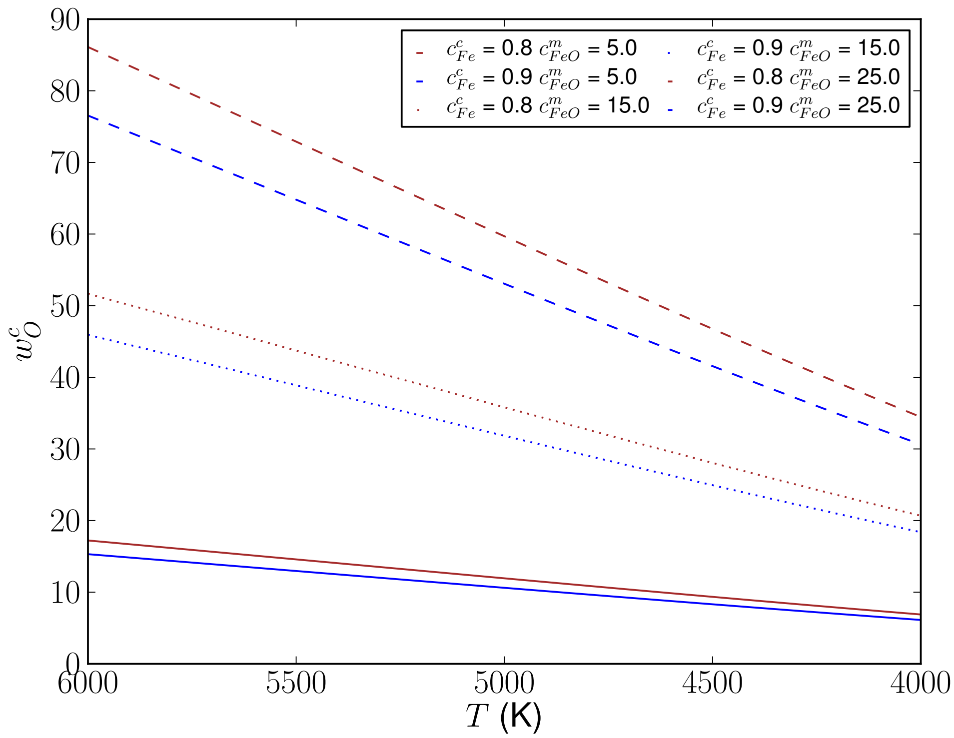

Figure 7: Equilibrium concentration of O in the core (wt %) as a function of temperature T for different concentrations of iron in the core, c_{Fe}^c, and FeO concentrations in the BMO, c_{FeO}^m.

range at high T; higher K_d^{FeO} would therefore increase the equilibrium concentrations in Figure 7. The results clearly show that the equilibrium O concentration exceeds all estimates for the bulk core O concentration. Therefore, FeO is expected to partition strongly into liquid iron at high T, creating a stably stratified layer atop the core (Buffett and Seagle, 2010; Davies et al., 2018).

3.4. Partitioning of multiple species at the CMB

In general the CMB compositions of the four elements assumed to be in the core (Fe, Si, O, Mg) and the three oxides assumed to comprise the BMO (MgO, FeO, SiO_2) can vary over time. The seven equations required to solve the system are obtained from mass balance of the four elements and the equilibrium constants for the three reactions (Rubie et al., 2011). These equations are nonlinear and hence both the onset and rate of precipitation of a given chemical species will in general depend sensitively on P, T, starting composition and the functional forms of the equilibrium constants. In this section we will show how the onset and rate of precipitation depend on these factors.

We calculate equilibrium concentrations following the method of Rubie et al. (2011). The main limitation of this method is that it is not easily generalised to include composition-dependence of the equilibrium constants. This is clearly an important issue since we have shown above that the equilibrium concentration of Mg is sensitive to the O and Mg concentration in the core. However, given the complexity of multi-species partitioning and significant uncertainties on some of the key parameters this is a necessary first step. It also simplifies the calculation of precipitation rates, which are needed by core thermal history models. Rubie et al. (2011) consider partitioning of Ni and assume a constant bulk Mg composition. Here we transpose Ni and Mg in their equations (details are provided in Appendix 1). We consider three different cases labelled according to whether the reaction governing transfer of O, Si and Mg are respectively exchange (E) or dissociation (D):

1. DEE. This Case corresponds to that of Rubie et al. (2011), who model oxygen transfer as a dissociation reaction and Si and Ni (here Mg) transfer by exchange reactions. The distributions coefficients are:

$$\log \frac{c^c_{Fe} c^c_O}{c^m_{FeO}} = a^{ds}_O + \frac{b^{ds}_O}{T} + c^{ds}_O \frac{P}{T}, \tag{24}$$

$$\log \frac{(c^m_{FeO})^2}{(c^c_{Fe})^2} \frac{c^c_{Si}}{c^m_{SiO2}} = a^e_{Si} + \frac{b^e_{Si}}{T} + c^e_{Si} \frac{P}{T}, \tag{25}$$

$$\log \frac{c^m_{FeO}}{c^c_{Fe}} \frac{c^c_{Mg}}{c^m_{MgO}} = a^e_{Mg} + \frac{b^e_{Mg}}{T} + c^e_{Mg} \frac{P}{T}. \tag{26}$$

2. DED. This Case retains the same reactions for Si and O as in Case 1, but employs a dissociation reaction for Mg as advocated by Badro et al. (2018) .
3. DDD. This Case employs dissociation reactions for all three species as done by Mittal et al. (2020), with distribution coefficients given by

$$\log \frac{c^c_{Fe} c^c_O}{c^m_{FeO}} = a^{ds}_O + \frac{b^{ds}_O}{T} + c^{ds}_O \frac{P}{T}, \tag{27}$$

$$\log \frac{c^c_{Si} (c^c_O)^2}{c^m_{SiO2}} = a^{ds}_{Si} + \frac{b^{ds}_{Si}}{T} + c^{ds}_{Si} \frac{P}{T}, \tag{28}$$

$$\log \frac{c^c_{Mg} c^c_O}{c^m_{MgO}} = a^{ds}_{Mg} + \frac{b^{ds}_{Mg}}{T} + c^{ds}_{Mg} \frac{P}{T}. \tag{29}$$

For Cases 2 and 3 the required modifications to the method of Rubie et al. (2011) are explained in Appendix 1.

The dependence of $\log K_d$ on temperature used in this section is shown in Figure 8. The a, b and c values are not the same as those in Table 4 because we ignore the composition-dependence. We have therefore refit K_d^{MgO} using the Badro et al. (2018) dataset as shown by the red lines in Figure 3, obtaining $a = -1.45$ and $b = -3596$ for the exchange reaction and $a = -1.039$ and $b = -6151$ for the dissociation reaction. We have also refit the a and b values from Du et al. (2019) based on a mean 15 mol% O in the core in order to account for the composition-dependence of their parameterisation. For Fe we use the parameters from Fischer et al. (2015). For reference, Figure 8 also shows K_d^{FeO} from Hirose et al. (2017); however, we were unable to obtain solutions to the mass balance equations with this parameterisation. For Si we use the exchange reaction parameterisation from Fischer et al. (2015) and the dissociation parameterisation of Mittal et al. (2020), who refit the partitioning data of Hirose et al. (2017).

Figure 9 shows two calculations using the initial compositions of Badro et al.

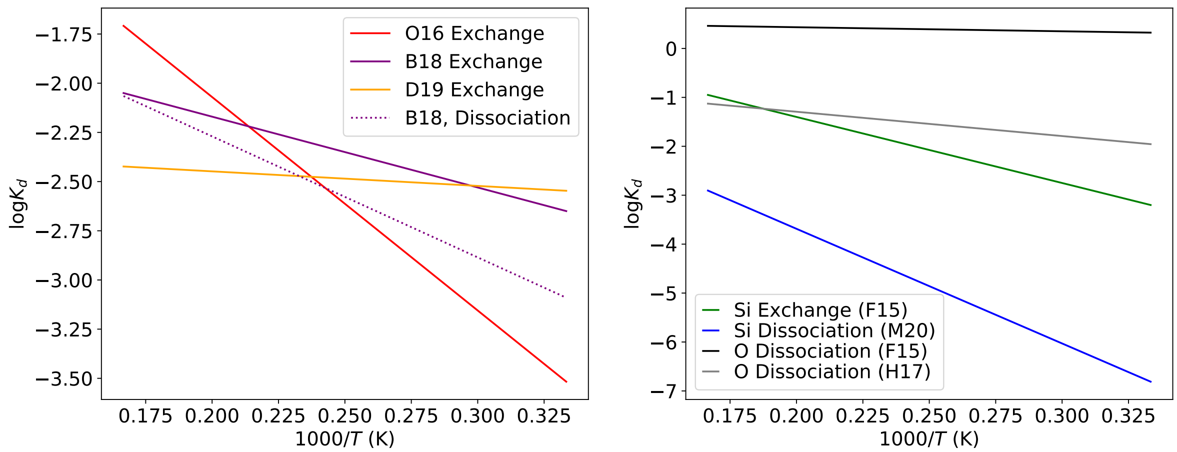

Figure 8: Distribution coefficients for Mg (left) and Si/O (right) used in comparison of multi-species precipitation.

(2018) for the DED and DEE cases respectively. The general behaviour in both cases is very similar to that described in O'Rourke and Stevenson (2016) and Liu et al. (2020) who used slightly different compositions and calculation methods: the core becomes gradually depleted in all light elements and the equilibrium oxide budget is dominated by MgO. Comparing DED to DEE, the only significant change is that the equilibrium Mg core composition and precipitation rate $\mathrm{d}w^c_{MgO}/\mathrm{d}T$ are increased by a factor of 3 and 2 respectively. Indeed, for the DED case the results are very similar to those for pure Mg partitioning (Figure 4) because the larger MgO concentration preferred in the multi-component case is offset by the larger equilibrium core O concentration. The increased w^c_{MgO} in the exchange reaction arises because of the increased MgO content of the BMO, while the FeO concentration is about the same as assumed in Figure 4 when considering only MgO partitioning (see equation (26)).

Figure 9 also shows for each element the temperature T_o below which precipitation would begin given the assumed initial compositions. Since the core Mg content was assumed to be zero, Mg does not precipitate in this calculation. Si does precipitate,

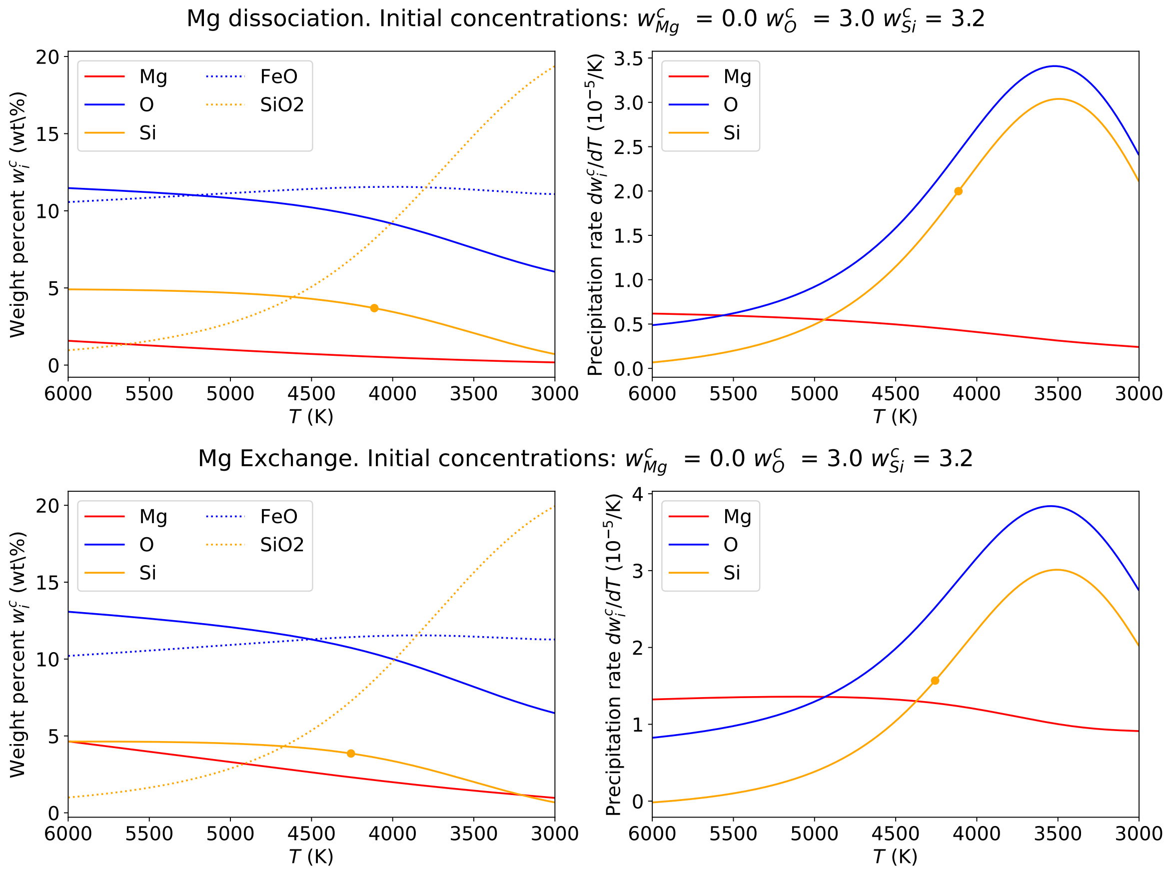

Figure 9: Equilibrium concentrations (left) and precipitation rate (right) for core elements and BMO oxides assuming the DED reaction set (top) and DEE reaction set (bottom). Dots mark the temperature at which the equilibrium core composition for element i falls below its concentration in the core.

but only once the CMB temperature has fallen below its current value of $\sim$4000 K. O never precipitates above 4000 K in all calculations we have undertaken.

Figure 10 compares equilibrium Mg concentrations and precipitation rates for three recent studies using the DEE Case. For direct comparison we have also reproduced a calculation where the O'Rourke and Stevenson (2016) parameters are all reduced by 0.25σ, where σ is the standard deviation quoted in their Extended Table 1. The results for the Du et al. (2019) and O'Rourke and Stevenson (2016) 0.25σ

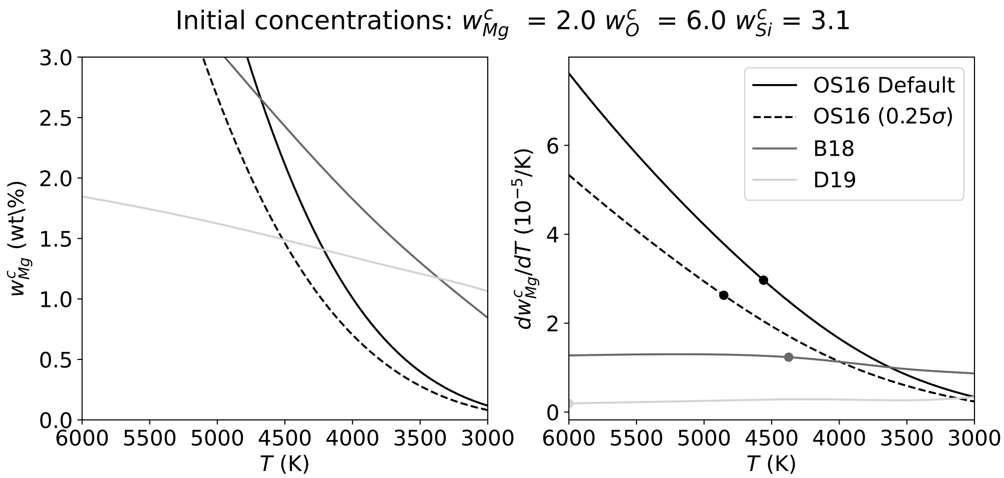

Figure 10: Equilibrium Mg concentration w^c_{Mg} (left) and Mg precipitation rate $\mathrm{d}w^c_{Mg}/\mathrm{d}T$ (right) plotted as functions of temperature T for the DEE reaction set. Parameters are from O'Rourke and Stevenson (2016, O16), Badro et al. (2018, B18) and Du et al. (2019, D19). Also shown is a case where the O'Rourke and Stevenson (2016) parameters are all reduced by 0.25σ, where σ is the standard deviation quoted in their Extended Table 1. Dots mark the temperature at which the equilibrium core composition for element i falls below its concentration in the core.

parameters are very similar to those reported in Figure 3a of Du et al. (2019), which is encouraging as we have used different methods to compute the equilibrium concentrations. The results using the Badro et al. (2018) parameters differ from those reported by Du et al. (2019), probably because we are considering the exchange reaction, which increases w^c_{Mg} as shown in Figure 9.

Figure 11 shows the equilibrium concentrations for Mg and Si and the Mg precipitation rate for the three different Cases and three initial oxide compositions corresponding to an MgO-rich, FeO-rich and SiO_2-rich BMO. There are three main messages from this Figure. First, the combination of reactions is crucial for determining both T_o and $\mathrm{d}w^c_{Mg}/\mathrm{d}T$; for certain BMO compositions $\mathrm{d}w^c_{Mg}/\mathrm{d}T$ varies by over an order of magnitude, while Mg precipitation can begin anywhere between 6000 K and 4000 K. Second, the initial BMO composition is generally less important for determining $\mathrm{d}w^c_{Mg}/\mathrm{d}T$, with variations of up to a factor of $2-3$, but is critical for determining T_o. Third, $\mathrm{d}w^c_{Mg}/\mathrm{d}T$ is not a monotonic function of T, though it is usually close to its maximum value when $T = T_o$. Finally, note that changing core composition does not significantly affect the basic evolution because all activity coefficients have been set to 1, but it does change the precipitation time. However, the results in Section 3 suggest this is not generally the case and more complex behaviour can be expected when the effect of compositional variations on the distribution coefficients are taken into account.

Figure 12 provides a synthesis of the multi-component precipitation results; it shows the temperature T_o below which precipitation begins and the precipitation rate at T_o for Mg and Si. In all calculations we have used an initial 2 wt% Mg in the core and so the values of T_o are probably at the upper end of viable estimates based on core formation studies. As shown by Mittal et al. (2020), the onset and rate of precipitation depend sensitively on several factors including the initial compositions and equilibrium constants. $\mathrm{d}w^c_{Mg}/\mathrm{d}T$ spans the range $0.3 - 3 \times 10^{-5}$ K^{-1}, which is broadly consistent with the results above considering pure Mg partitioning, while $\mathrm{d}w^c_{Si}/\mathrm{d}T$ spans the range $0.1 - 8 \times 10^{-5}$ K^{-1}. These rates are sufficient to provide significant gravitational power to the dynamo as will be shown below. There is a large spread of T_o values in both cases; however, most models favour onset of Mg precipitation at or below 5000 K while Si precipitation tends to begin at or below 4500 K. O'Rourke and Stevenson (2016) and Badro et al. (2016) also found a delayed onset of precipitation. The results in Section 3.2 suggest that accounting for composition-dependence reduces both T_o and $\mathrm{d}w^c_i/\mathrm{d}T$ and so we regard the values in Figure 12 as upper estimates based on presently available information. This suggests that precipitation began after core formation; before this time, light elements would have entered the core, providing a mechanism to stably stratify the upper core.

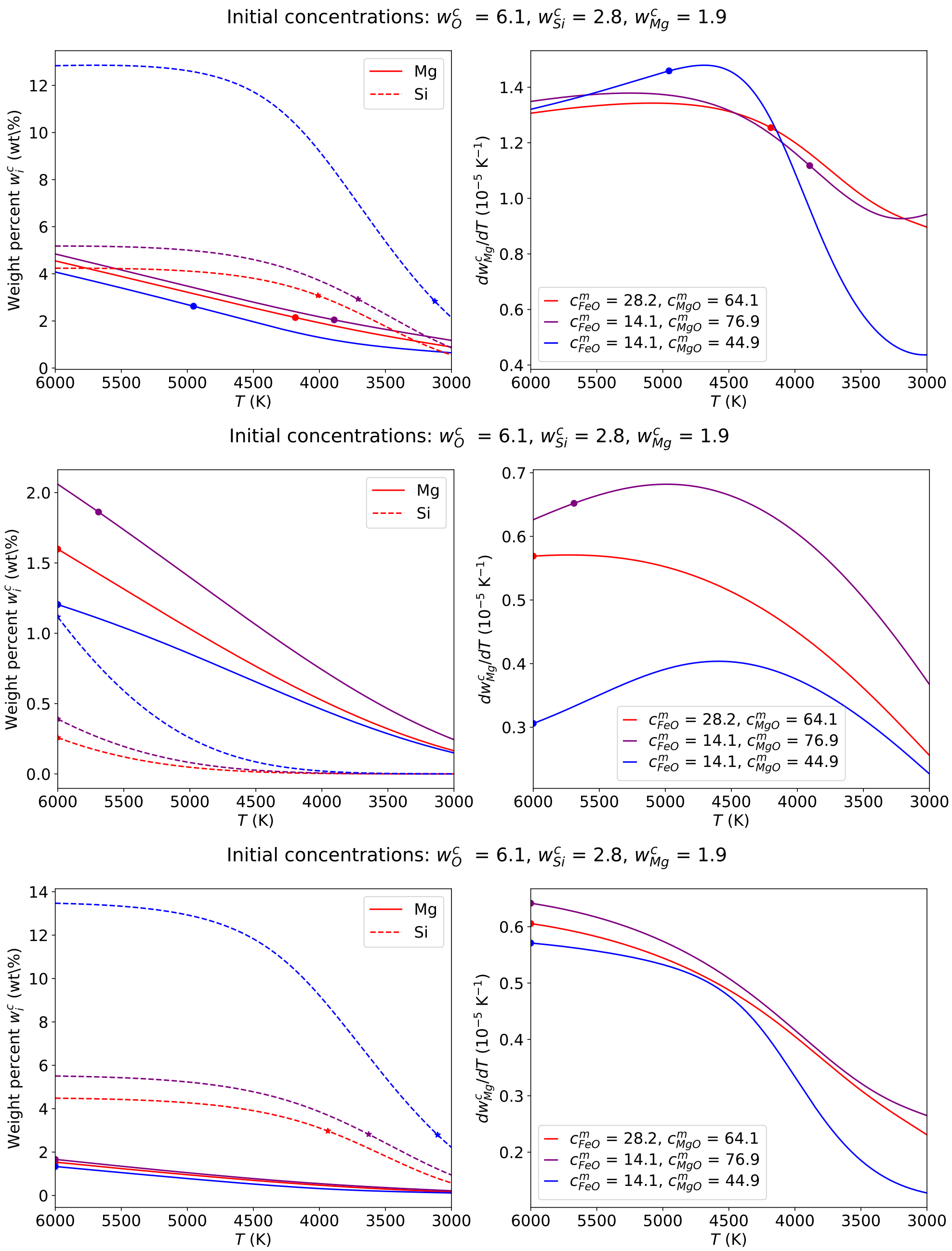

Figure 11: Equilibrium Mg and Si concentrations (left) and Mg precipitation rate $\mathrm{d}w^c_{Mg}/\mathrm{d}T$ (right) plotted as functions of temperature for Cases DEE (top), DDD (middle) and DED (bottom) described in the text. Dots mark the temperature at which the equilibrium core composition for element i falls below its concentration in the core.

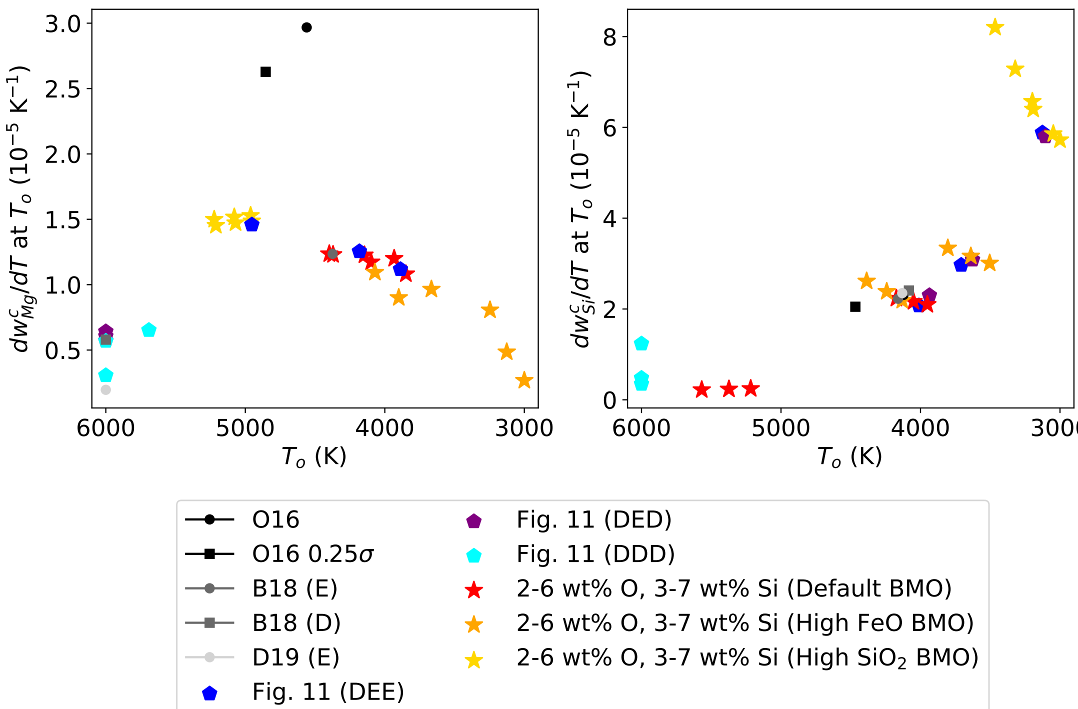

Figure 12: Precipitation rate of Mg (left) and Si (right) at the time T_o when precipitation began. The corresponding value of T_o is shown on the horizontal axis. All calculations have used an initial Mg core concentration of 2 wt%. Results for O'Rourke and Stevenson (2016, O16), Badro et al. (2018, B18) and Du et al. (2019, D19) are from Figure 10 except for the B18 Dissociation (D) case. The results denoted by stars have a default BMO composition of 28 mol% FeO, 64 mol% MgO and 8 mol% SiO_2. The results denoted by pentagons are from Figure 12.

4. Stratification below the CMB

4.1. Modern-day Observations of Stratification

Observational constraints on the presence of stratification at the top of the core have primarily originated from seismic studies. A number of SmKS wave studies (Lay and Young, 1990; Garnero et al., 1993; Helffrich and Kaneshima, 2010; Kaneshima, 2018) find a P-wave velocity reduction and steeper P-wave gradient relative to PREM up to 400km deep into the core. The strength of stratification is often measured by the Brunt-Väisälä period

$$T_{\mathrm{BV}} = \frac{2\pi}{N} = 2\pi\left(-\frac{g}{\rho}\frac{\partial\rho'}{\partial r}\right)^{-1/2}, \tag{30}$$

which determines the period of oscillations that arise when a fluid parcel in a stratified region is subjected to vertical displacement. Here the equation defines the Brunt-Väisälä frequency N and a prime denotes the non-hydrostatic part of density ρ. Matching a compositional model to the observed wavespeeds suggests $T_{\mathrm{BV}} = 1.6-3.4$ hours, implying strong stratification (Helffrich and Kaneshima, 2010). Alexandrakis and Eaton (2010) argued that stratification is absent at the top of the core; however, van Tent et al. (2020) showed that the Alexandrakis and Eaton (2010) data do not conflict with a low velocity region in the uppermost core, suggesting that methodological differences are responsible for the divergent conclusions. Irving et al. (2018) have derived a new 1D core reference model using normal mode centre frequencies, which provide a more direct constraint on density than body waves. The model suggests a lower P-wave velocity and higher density than PREM throughout the core thus reducing, though not eliminating, the stratification signal. van Tent et al. (2020) recently conducted an extensive review and concluded that "both seismological body-wave and normal mode observations require a low-velocity outermost core with respect to PREM, as well as a steeper velocity gradient than PREM". Evidently, there is now a reasonable degree of support for anomalous seismic velocity structure in the uppermost core.

At present it is not clear whether low seismic velocities in the upper core are a global or local feature. The SmKS data coverage is rather heterogeneous, with large regions of the uppermost core (e.g. under North America and the Indian ocean) not sampled by available raypaths (see Kaneshima, 2018). The distinction is crucial. Low velocities (with respect to PREM) reflect variations in either density or bulk modulus. If a global layer of anomalous fluid exists at the top of the core then this layer must be light, otherwise it would mix back into the bulk core. This implies that the velocities must reflect a greater decrease in bulk modulus than density, for example due to enrichment in one or more light elements (Helffrich, 2012; Komabayashi, 2014; Brodholt and Badro, 2017). On the other hand, if the velocity anomalies are local then there is no stability requirement since the anomalies could sample part of a large-scale circulation pattern (Mound et al., 2019). However, in both cases the seismic velocities imply thermo-chemical anomalies greater than those associated with core convection (Helffrich and Kaneshima, 2010) and so some other mechanism is required to explain their existence.

Observations of the geomagnetic secular variation have been used to search for radial motion near the top of the core, which is expected to be absent in a stable layer. In purely horizontal flows, local extrema in the radial magnetic field are time invariant (Whaler, 1980); however, this test for stratification renders inconclusive results owing to large uncertainties on estimates of the CMB field at a point (Whaler, 1986). Gubbins et al. (2007) showed that the present evolution of the south Atlantic anomaly, when attributed to flux expulsion, strongly suggests radial flow in the top 100 km of the core, while Amit (2014) argued that the mobility of high-latitude flux patches is best explained by localised downwelling. Lesur et al. (2015) inverted for the fluid flow at the top of the core and found that purely horizontal flow is not compatible with satellite observations of recent field variations but that a very limited amount of radial motion (comparable to diffusion, which was ignored) allows for acceptable fits. All of these studies neglected magnetic diffusion (following Roberts and Scott, 1965); however, diffusion is not necessarily negligible and potentially could explain much of the observed variation (Metman et al., 2019), negating the need for radial fluid flow to explain the temporal features of the field. Furthermore, steady flow over CMB topography in a stably stratified layer can induce radial motion (Glane and Buffett, 2018), complicating attempts to rule out stratification by searching for radial flow.

Buffett (2014) has shown that simple combinations of axisymmetric Magneto-Archimedian-Coriolis (MAC) waves in a stably stratified layer can explain a 60-yr periodic variation of the dipole geomagnetic field and the recent time-dependent evolution of zonal flow at the top of the core. The inferred stratified layer thickness is $130 - 140$ km with a maximum $N/\Omega \sim 1$ (Buffett et al., 2016) or $T_{\mathrm{BV}} \sim 24$ hrs, implying weaker stratification than inferred from seismology. Subsequent work has shown that these waves can be generated by underlying core convection (Jaupart and Buffett, 2017) and exchange some angular momentum with the mantle though not enough to explain decadal variations in length-of-day (Holme and de Viron, 2013; Buffett et al., 2016). Thus far, models based on MAC waves have assumed a global stable layer at the top of the core.

Another approach to investigating present-day stratification is to calculate the radial variation of buoyancy sources within the core (Davies and Gubbins, 2011; Gomi et al., 2013; Nimmo, 2015a). This method uses energy and mass conservation to balance the CMB heat flow against the sum of power sources inside the core (as outlined in Section 2.2). The core is assumed to be 1D and so stratification implicitly arises in the form of a layer. Stratification requires that

$$\alpha_{\mathrm{T}} \left(\frac{\mathrm{d}T}{\mathrm{d}r} - \frac{\mathrm{d}T_{\mathrm{a}}}{\mathrm{d}r} \right) + \alpha_i^{\mathrm{c}} \frac{\mathrm{d}w_i^c}{\mathrm{d}r} > 0, \tag{31}$$

(Landau and Lifshitz, 1987) which serves to define the base of the layer. Here r is radius, T and T_{a} are the temperature and adiabatic temperature respectively and barodiffusion has been ignored. The main challenge is approximating the gravitational energy since the spatial distribution of ohmic and viscous dissipation is not known (Jackson and Livermore, 2009), so various approaches have been used in the literature (see Davies and Gubbins, 2011; Gomi et al., 2013, for detailed discussion). Pozzo et al. (2012) used high k and found stable layers up to $O(1000)$ km thick depending on the imposed CMB heat flow. Gubbins et al. (2015) calculated a maximum present-day stable layer thickness of 740 km assuming high k and no dissipation available to generate the magnetic field; however, they dismiss such thick layers as being incompatible with geomagnetic secular variation.

The "buoyancy" approach to assessing present-day stratification is sensitive to a number of uncertain parameters including the CMB heat flow and ICB density jump, but also the depth dependence of thermal conductivity. Labrosse et al. (2015) calculated convective heat flow using the k profiles from Gomi et al. (2013) and Pozzo et al. (2012), the latter of which has a slightly shallower gradient. For mildly superadiabatic Q^{c} the Gomi et al. (2013) $k(r)$ suggests a stratified region within the core, whereas the Pozzo et al. (2012) $k(r)$ predicts no stratification anywhere. The present uncertainty on $k(r_{\mathrm{c}})$ (Section 2.3), let along $k(r)$, currently prevents definitive conclusions on the presence of stratified regions within the bulk core.

Overall there is support from seismology for strongly stratified regions up to

400 km thick at the top of the core. The geomagnetic observations paint a more complex picture and seem to prefer thinner stratified regions or no stratification at all. The observations also do not determine whether the stratification is regional or in the form of a global layer. We therefore turn to computational methods for investigating core stratification. There are two main approaches: direct numerical simulations (DNS, Section 4.2) represent the spatio-temporal interactions between core flow, stratification and magnetic field on centennial to millennial timescales, but have stable layers imposed; parameterised models (Section 4.3) investigate the Gyr timescale formation and evolution of stable layers, but only determine the radial thickness and strength of stratification. The stratification derives from some combination of thermal and chemical effects and so below we consider these possibilities in turn, focusing on the key issues that will help distinguish between the myriad scenarios. In particular we aim to shed light on the following questions: How did the stratification form? How has the stratification evolved over time? What is the predicted present-day thickness and stratification strength? Is the stratification global or local?

4.2. Direct Numerical Simulations (DNS) and Theory

There is a growing consensus from DNS that strong and thick stable layers are incompatible with the morphology of the present magnetic field. Olson et al. (2017), Olson et al. (2018), Christensen (2018) and Yan and Stanley (2018) performed DNS with thermal and compositional effects combined into a single co-density (see Braginsky and Roberts, 1995) and imposed a variety of CMB co-density gradients, both homogeneous and heterogeneous, promoting varying degrees of stabilising density gradients. Olson et al. (2017) and Olson et al. (2018) examined over 60 dynamo solutions and found that the high-latitude field morphology and the ratio of normal to reversed CMB flux are sensitive to the degree of stratification. They concluded that a weakly stratified 400-km-thick layer layer with $N_0/\Omega \sim 0.5$ ($T_{\mathrm{BV}} \sim 12$ hrs) is compatible with the simulation results, where

$$\frac{N_0}{\Omega} = \frac{1}{\Omega}\left(\alpha_{\mathrm{T}} g \frac{\partial T'}{\partial r}\right)^{1/2} \tag{32}$$

is the Brunt-Väisälä frequency derived from thermal variations only. Christensen (2018) considered 26 simulations with N_0/Ω in the range $2.4 - 4$. He applied the morphological criteria defined in Christensen et al. (2010) and found that simulations with 400-km-thick layers were only marginally compatible with the modern field. Yan and Stanley (2018) showed that the ratio of zonal dipole to octupole Gauss coefficients, g_3^0/g_1^0, is sensitive to the presence of a stable layer. From 33 simulations they found that matching both Earth's g_3^0/g_1^0 over the last 10 kyrs (obtained from the CALS10K.2 model of Constable et al., 2016) and the modern field (according to the Christensen et al. (2010) criteria) entails a trade-off between stratification strength and thickness. Their preferred solutions had layer thicknesses in the range $60 - 130$ km and $N_0/\Omega < 1$. Recently Gastine et al. (2020) modelled thermal stratification in a suite of 70 simulations with $0 \leq N_0/\Omega \leq 50$ and found that CMB fields become more dipolar and axisymmetric with increasing layer thickness, in line with previous studies (Christensen, 2006; Nakagawa, 2011), and hence generally do not match the modern geomagnetic field (again as assessed by the Christensen et al. (2010) criteria). They therefore argued against the presence of stratification in Earth's core.

A number of the aforementioned studies combined an imposed stable layer with lateral heat flow variations on the CMB. When the stratification is weak the lateral variations can induce flow at the CMB (Olson et al., 2017), effectively overcoming the mean stabilising codensity gradient in local regions where the CMB heat flow is anomalously high. However, for thick imposed layers, as the stratification strength increases the influence of the lateral variations is strongly diminished and the stable layer behaviour is relatively unaffected by their presence (Christensen, 2018). Using a simple model of non-magnetic thermal convection, Cox et al. (2019) showed that the transition between these two regimes (boundary-dominated and stratification-dominated) arises when the stratification parameter S, defined as the relative size of boundary temperature gradients to imposed vertical temperature gradients, exceeds unity. However, given uncertainties in estimating S for Earth they were unable to conclude whether the core is currently in the high S or low S regime.

Lateral heat flow variations can induce regional stratification even when the mean CMB heat flow is destabilising. Mound et al. (2019) found that thick localised stable regions were ubiquitous in a large suite of non-magnetic simulations that access the regime of rapid rotation and vigorous convection thought to be most relevant to Earth's core (Long et al., 2020). In these simulations the lateral extent of the stable regions is set by the imposed boundary anomalies (which were derived from seismic tomography) rather than the small scale motions associated with vigorous convection in the bulk of the core. Interestingly, 1D averaging in these models can yield a net stabilising temperature gradient, giving the impression of global stratification despite the presence of motion in regions of the upper core. Using scaling analysis Mound and Davies (2020) estimated that stable regions in Earth's core could extend up to 350 km depth, similar to the thick layers inferred from seismology. They obtained values of $N_0/\Omega \approx 2 - 5$, corresponding to $T_{\mathrm{BV}} \sim 5 - 12$ hrs, lower than estimates by Helffrich and Kaneshima (2010) but larger than that inferred from MAC waves (Buffett et al., 2016).

A variety of processes besides lateral heat flow variations can act to disrupt or even completely erode a pre-existing stable layer. It is well known from oceanography and astrophysics (Turner, 1973; Garaud, 2018) that stable systems where thermal and compositional fields have different diffusivities and adverse gradients are prone to instabilities that can drastically change their behaviour. These "double-diffusive" instabilities have recently begun to receive substantial attention in the planetary core context (Monville et al., 2019; Bouffard et al., 2020; Mather and Simitev, 2020). Heat diffuses faster than light elements in the core (Pozzo et al., 2013) and so the double diffusive dynamics take the form of 'oscillatory convection' if the chemical gradient is stabilising and the thermal gradient is destabilising; switching the signs of the gradients gives 'finger convection' (Turner, 1973). The relevant configuration for Earth's core may have varied over time.

As described in more detail in Section 4.4 below, chemical stratification may have originated early in Earth's history, either due to incomplete mixing during core formation (Landeau et al., 2016; Jacobson et al., 2017) or via enrichment in FeO from the mantle (Buffett and Seagle, 2010; Davies et al., 2020, and also Section 3.3). In the absence of precipitation, thermal convection was needed to power the geodynamo prior to inner core formation $0.5 - 1$ Gyrs ago (Nimmo, 2015a, and Table 1) and so thermal stratification should be a relatively recent feature. The core may have become thermally stratified below the CMB once precipitation began; however, the assessment in Section 3.4 suggests this was after core formation and so thermal convection would have been needed to power the dynamo before the core cooled to $\sim$5000 K. In this case the appropriate regime for modelling double diffusion in the early core is "oscillatory" convection (Bouffard et al., 2020). Depending on the strength of chemical stability and the Lewis number $Le = \kappa/D_i$, the ratio of thermal and chemical diffusion coefficients, large-scale secondary instabilities can emerge in the form of staircases or coherent vortices (Garaud, 2018; Monville et al., 2019).

The relevant configuration for the present day depends on the CMB heat flow and the survival of any primordial chemical layer. The total heat Q extracted from the core at present is estimated at $7-17$ TW (Nimmo, 2015a) while the adiabatic heat flow is around $Q_a = 14-16$ TW (Davies et al., 2015) and so both thermally stable ($Q^{\mathrm{c}} < Q_{\mathrm{a}}^{\mathrm{c}}$) and unstable ($Q^{\mathrm{c}} > Q_{\mathrm{a}}^{\mathrm{c}}$) conditions are consistent with available constraints. If chemical layers do survive then the configuration is either in the oscillatory regime or is completely stratified if $Q^{\mathrm{c}} < Q_{\mathrm{a}}^{\mathrm{c}}$, though the enrichment of the liquid in light elements due to inner core growth provides a potential destabilising mechanism. If chemical layers do not survive then any stable layer must be thermally stratified ($Q^{\mathrm{c}} < Q_{\mathrm{a}}^{\mathrm{c}}$), while composition is destabilising due to chemical convection arising from inner core growth. This system is in the 'finger' regime and can exhibit secondary instabilities in the form of large-scale zonal flows (Monville et al., 2019).

At present, it seems premature to apply the results of double-diffusive DNS studies to Earth's core. The simulations are extremely challenging because the value of $Le \sim 1000$ in Earth's core (Pozzo et al., 2013), which induces a large scale disparity between thermal and compositional fields. This difficulty has also prompted workers to invoke further simplifications, such as omitting the magnetic field (Monville et al., 2019) or imposing double diffusive conditions throughout the core (rather than just near the CMB) (Mather and Simitev, 2020). Finally, all current simulations are far from the rapidly rotating and low viscosity conditions of the core and robust scaling relationships of the kind that have recently been devised for the single-component system (Aubert et al., 2017; Wicht and Sanchez, 2019) have not yet been produced for the double-diffusive case. This area of research will undoubtedly see significant progress in the coming years.

Stable layers can be influenced by penetration from the underlying convection. Takehiro and Lister (2001) studied penetration of rapidly rotating non-magnetic convection underlying a stable layer and found that the penetration depth scales as $\ell_s(N/\Omega)^{-1}$, where ℓ_s is the characteristic flow scale. Gastine et al. (2020) have found good agreement with the Takehiro and Lister (2001) scaling in numerical simulations when N is calculated as the mean over the stable region. At the layer interface Gastine et al. (2020) found that ℓ_s is comparable to the lengthscale for the onset of convection, in which case the penetration depth is only a few hundred metres. Gubbins and Davies (2013) obtained a similar result by a different line of reasoning.

A related issue is whether turbulent convection can erode a stable layer by entraining buoyant fluid into the bulk. This problem has been studied extensively in oceanography (e.g. Levy and Fernando, 2002), but has only recently been studied in the context of Earth's core. Bouffard et al. (2020) considered the erosion of a thick ($\sim$700 km) pre-existing chemically enriched layer by thermal convection in non-magnetic simulations representative of an early Earth (no inner core). They found greater erosion in the equatorial plane than near the poles and estimated erosion rates (represented as the rate of change of stable layer thickness) of only $\sim$1 km Gyr^{-1} or less, despite considering the end member case of zero chemical diffusion. Only in a subset of their models do they find developed double diffusive convection, which they propose would become more prevalent in their simulations as the Ekman number further lowers towards predicted values for Earth. Interestingly Bouffard et al. (2020) find that an initial overshoot in kinetic energy in their simulations causes massive entrainment of the layer. This could simply reflect transient evolution from an arbitrary initial condition, though future work may consider whether physical effects (e.g. a giant impact) could produce similar behaviour.

Gubbins and Davies (2013) considered whether a chemically stable layer could be mixed by the Kelvin-Helmholtz instability. The sufficient condition for an inviscid and non-magnetic stratified fluid to be stable to Kelvin-Helmholtz instability is that the local Richardson number

$$Ri = \frac{N^2}{(\mathrm{d}U/\mathrm{d}z)^2} > 1/4, \tag{33}$$

where U is the flow speed and z the vertical coordinate. Both N and the shear $(\mathrm{d}U/\mathrm{d}z)$ vary with depth and cannot be observed directly in Earth's core. Gubbins and Davies (2013) assumed a constant value of $(\mathrm{d}U/\mathrm{d}z)$ throughout the layer inferred from core flow models (Holme, 2007) and used the approximately linear form of N obtained for a layer formed by barodiffusion, concluding that the layer is stable everywhere except in the bottom few km. We expect a similar result for other layer formation mechanisms for which N is approximately linear across the layer (Buffett and Seagle, 2010; Buffett, 2014).

Overall, numerical dynamo simulations incorporating global stratification that have attempted to match geomagnetic observations tend to favour thinner and more weakly stratified layers than those inferred from seismology. Some studies have also argued against the presence of a stable layer. A clearer understanding of the role of double diffusive instabilities, and particularly the attendant generation of large-scale flows, is necessary before more definitive conclusions can be drawn. Most current studies do agree that existing layers are stable to penetration, entrainment, interface instabilities and lateral variations in CMB heat flow. Regional stratification is another possibility, offering a plausible framework for producing both the significant compositional anomalies suggested by seismic studies and the upwelling flow near the top of the core that is preferred by a number of geomagnetic studies.

4.3. Evolution of Thermal Stratification

The evolution of the core over the age of the Earth is usually investigated using thermal history models. These models assume spherical symmetry and use global conservation of energy and entropy to solve for the core cooling rate and hence the power that is available to generate the magnetic field (see Nimmo, 2015a,b, for a detailed review of the methodology and standard solutions). In this approach the bulk of the core is assumed to be hydrostatic, adiabatic and compositionally well-mixed, while within a stable layer diffusion is assumed to control the radial temperature and compositional profiles. When small terms are neglected (see Gubbins et al., 2004; Nimmo, 2015a; Davies, 2015, for details) the energy balance can be written symbolically as

$$Q^{\mathrm{c}} = Q_{\mathrm{s}} + Q_{\mathrm{L}} + Q_{\mathrm{g}} + Q_{\mathrm{p}} = A\frac{\mathrm{d}T_{\mathrm{c}}}{\mathrm{d}t}, \tag{34}$$

(see Section 2.2) where $\mathrm{d}T_{\mathrm{c}}/\mathrm{d}t$ is the core cooling rate at the CMB. This equation states that the CMB heat flow Q^{c} is balanced by the heat Q_{s} stored in the core, the latent heat Q_{L} due to inner core freezing, the gravitational energy Q_{g} released as light elements are redistributed throughout the liquid as the inner core grows, and the gravitational energy released due to precipitation, Q_{p}, which arises when heavy residual liquid downward mixes into the bulk core. The magnetic field arises in the entropy budget, which can be written symbolically (again neglecting small terms) as

$$E_{\mathrm{J}} + E_{\alpha} + E_{\mathrm{k}} = E_{\mathrm{s}} + E_{\mathrm{L}} + E_{\mathrm{g}} + E_{\mathrm{p}} = B\frac{\mathrm{d}T_{\mathrm{c}}}{\mathrm{d}t}. \tag{35}$$

Here E_{α} is the entropy due to molecular diffusion of light elements, E_{k} is the entropy due to thermal conduction (which depends on the thermal conductivity) and E_{J} is the entropy production by Ohmic dissipation. The term E_{α} is negligible in this section; however, it will be important when considering FeO dissolution in Section 4.4 below. We have also neglected radiogenic heating since potassium 40 is not thought to partition significantly into the core (Xiong et al., 2018). In this section we also ignore $Q_{\rm p}$ and $E_{\rm p}$, but will reintroduce them when considering precipitation in Section 5.

The main uncertainties in the calculations using equations (34) and (35) are the time evolution of the CMB heat flow $Q^{\rm c}$, the precipitation rate (see Section 3), and the ICB density jump $\Delta\rho$ (see Section 2). The main outputs are the time evolution of the radius of the inner core, stable layer thickness and strength, and $E_{\rm J}$, which is required to be positive for dynamo action (Gubbins et al., 2003, 2004; Nimmo, 2015a). The vast majority of previous studies have assumed that the stable layer grows downwards from the CMB and so we also make this assumption in the remainder of this section.

Most previous studies of core thermal stratification have assumed a prescribed $Q^{\rm c}$ and focused on the core evolution. The key methodological differences are the numerical scheme used to solve for the time dependent growth of the layer and the choice of boundary conditions coupling the stable layer and convective region at their interface, $r_{\rm s}$. In an early study Gubbins et al. (1982) assumed continuity of thermal gradient at $r_{\rm s}$ and a constant CMB temperature, which ensured that sub-adiabatic conditions developed at the CMB. In a simple demonstration of the physical behaviour they found a $\sim$1000 km thick layer formed over 4.5 Gyrs for $k = 15$ W m^{-1} K^{-1}. Labrosse et al. (1997) instead modelled the moving boundary problem with a solution to a Stefan problem, which allowed both the temperature and its gradient to be continuous at $r_{\rm s}$ and the interface velocity to be determined. Imposing a linearly decreasing $Q^{\rm c}(t)$ that became sub-adiabatic at $\sim$ 1.5 Ga they obtained a $\sim$600 km thick stable layer at present. Although chemical effects were neglected within the stable layer, Labrosse et al. (1997) estimated the effects of changing composition due to inner core growth may lead to destabilising chemical gradients and potentially double-diffusive "finger" instabilities. Lister and Buffett (1998) assumed that finger convection mixes light elements uniformly throughout the layer and applied continuity of density at r_{s} (though the light element concentration is discontinuous). With a similar parameter choice to Labrosse et al. (1997) they found the deficit of light element in the layer limits the growth of the layer to $\sim$400 km.

Greenwood et al. (2021) recently examined the limits to present day thermal stratification in the high conductivity scenario (Table 1) using the data from Davies et al. (2015) and a similar setup to Labrosse et al. (1997), i.e. continuity of temperature and temperature gradient at r_{s}. In the absence of radiogenic heating and precipitation, thermal convection is required to generate the magnetic field prior to inner core nucleation and so high k implies that the time during which thermal stratification may grow is limited to the last $0.5 - 1$ Gyrs. Like the studies discussed in the previous paragraph, Greenwood et al. (2021) did not solve for the mantle evolution, but instead imposed a linear variation in $Q^{\mathrm{c}}(t)$ following inner core formation as suggested by recent coupled core-mantle evolution models (Driscoll and Bercovici, 2014; Nakagawa and Tackley, 2014; Patočka et al., 2020). Considering a wide range of present day heat flows and constant $\mathrm{d}Q^{\mathrm{c}}/\mathrm{d}t$ values, Greenwood et al. (2021) provide upper bounds on the present day size for the layer at 700 km, which is only achieved in the most extreme scenarios.

Whilst the recent trend in CMB heat flow is approximately linear, the long-term ($\sim$3.5 Gyrs) variation in Q^{c} based on published coupled models instead shows an exponential decrease (Figure 13). Extrapolating their short term linear heat flows back along an exponential to 3.5 Ga, Greenwood et al. (2021) find that scenarios producing present-day layers thicker than $\sim$400 km would require heat flows in the ancient Earth exceeding 70 TW, significantly larger than produced by coupled evolution models in the high conductivity scenario (Driscoll and Bercovici, 2014; Nakagawa and Tackley, 2014; Patočka et al., 2020). Filtering out models predicting > 70 TW in the ancient core Greenwood et al. (2021) obtain upper bounds of 400 km on the layer thickness, with minimum Brunt-Väisälä periods (peak N_0) of $T_{\rm BV} = 8 - 24$ hrs.

Strictly, the long-term evolution of $Q^{\rm c}$ and the core temperature are coupled and should be obtained self-consistently. The presence of a stable layer will alter the feedback between the core and mantle, although given our models only produce temperature anomalies of $\sim$10 K, the effect is likely to be insignificant. Thermal stratification raises the core temperature above the adiabat, which increases $Q^{\rm c}$ (all else being the same) and reduces ${\rm d}Q^{\rm c}/{\rm d}t$. The same effect arises when the inner core forms, where latent heat and gravitational energy reduce the core cooling rate [see equation (11)], reducing ${\rm d}Q^{\rm c}/{\rm d}t$. Therefore, extrapolating along an exponential curve tied to the present day ${\rm d}Q^{\rm c}/{\rm d}t$ likely under-estimates the ancient $Q^{\rm c}$. Future coupled models of a core-mantle evolution with core stratification may therefore find further reductions to the 400 km limit proposed by Greenwood et al. (2021).

We end this section by examining stable layer properties obtained using $k = 70$ W K^{-1} m^{-1} at the CMB, the lower values proposed in the 'high' conductivity scenario (Table 1), complementing the results of Greenwood et al. (2021) who considered the upper range of $k = 100$ W K^{-1} m^{-1} at the CMB. We repeat both the methodology and analysis of Greenwood et al. (2021), using the same depth dependence on k given in Davies et al. (2015) for ICB density jumps of $\Delta\rho = 600, 800$ and 1000 kg m^{-3} and a wide range of ${\rm d}Q^{\rm c}/{\rm d}t$ values. A full list of parameter values is given in Table 2. Figure 14 shows the resulting present day layer thickness; grey shaded regions indicate a super-adiabatic core and hence no stable layers, while white regions indicate models that are rejected for not producing a magnetic field ($E_{\rm J} > 0$) at all times. A wedge in the parameter space remains where the heat flow is sub-adiabatic at present,

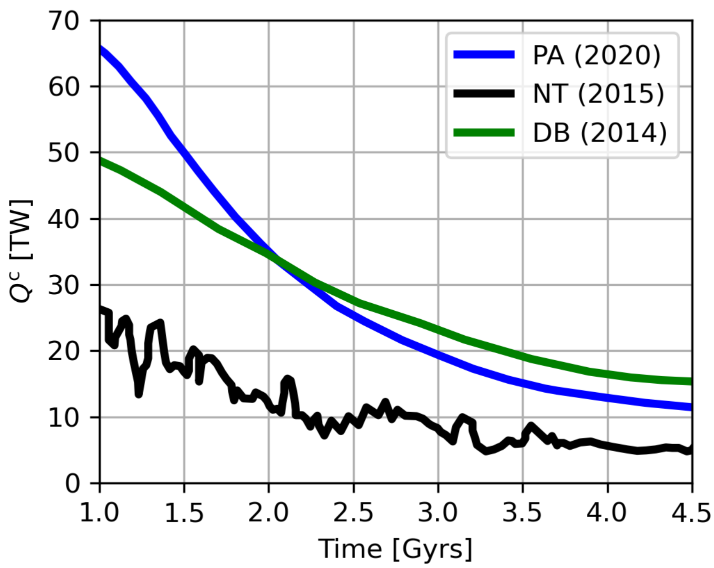

Figure 13: Published CMB heat flows from coupled core and mantle thermal history models. In the legend, PA (2020), NT (2015), and DB (2014) refer to the studies of Patočka et al. (2020, their Figure 12), Nakagawa and Tackley (2014, their Figure 9), and Driscoll and Bercovici (2014, their Figure 5) respectively.

producing thermal stratification, but with a fast enough $\mathrm{d}Q^{\mathrm{c}}/\mathrm{d}t$ to enable super-adiabatic heat flows prior to inner core formation.

Figure 14 shows that viable solutions maintaining $E_{\mathrm{J}} > 0$ and matching the present ICB radius are obtained with lower values of the present day Q^{c} for $k = 70$ W m^{-1} K^{-1} compared to $k = 100$ W m^{-1} K^{-1} due to a lower E_{k} in the entropy balance. Filtering out solutions that produce ancient heat flows exceeding 70 TW (see contours in Figures 14) gives a maximum layer thickness of $\sim$500 km with $k = 70$ W m^{-1} K^{-1} or $\sim$700 km when $\Delta\rho = 1000$ kg m^{-3}, significantly larger than the maximum thickness of $\sim$400 km when $k = 100$ W m^{-1} K^{-1} since the lower value of k permits lower heat flows which are proportionally further below the isentropic value. The minimum Brunt-Väisälä period (peak N_0), shown in Figure 15, is not significantly different to the range in Greenwood et al. (2021) ($8 - 24$ hours). Lowering k to 70 W m^{-1} K^{-1} shifts the value of Q^{c} at which stratification begins to grow; however, T_{BV} for a given ratio of $Q^{\mathrm{c}}/Q^{\mathrm{c}}_{\mathrm{a}}$ remains the same. Despite the range of core properties and $\mathrm{d}Q^{\mathrm{c}}(t)/\mathrm{d}t$ values used, the strength of stratification depends predominantly on the ratio $Q^{\mathrm{c}}/Q^{\mathrm{c}}_{\mathrm{a}}$ at present day. Models that are mildly sub-adiabatic ($Q^{\mathrm{c}}/Q^{\mathrm{c}}_{\mathrm{a}} > 0.8$) give periods similar to those inferred from MAC waves (Buffett et al., 2016) and comparisons of dynamo models with the magnetic field (Olson et al., 2017). Periods inferred from seismology of $1.3 - 3.5$ hours (Helffrich and Kaneshima, 2010) lie outside the ranges produced by thermal stratification, which given the trend in Figure 15 would require unrealistically low heat flows.

4.4. Evolution of Chemical Stratification

Chemical stratification arises when fluid at the top of the core is enriched in one or more light elements, thus reducing the fluid density. The source for this light element enrichment must be either an internal mechanism redistributing light element

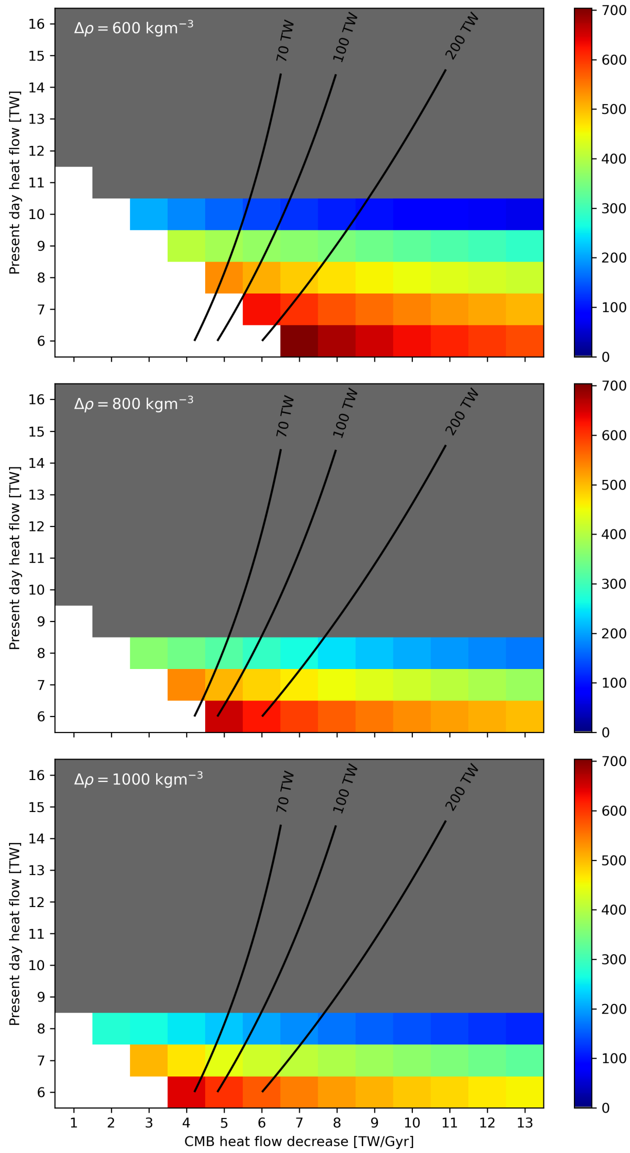

Figure 14: Present day thickness of thermally stratified layers for a parameter search across linear CMB heat flow trends and $\Delta\rho = 600, 800$ and 1000 kg m^{-3}, assuming $k = 70$ W m^{-1} K^{-1} at the CMB. Grey regions are super-adiabatic at present and so produce no thermal stratification. White regions indicate solutions where positive dynamo entropy was not maintained across the duration of the run. Contours indicate the CMB heat flow at 3.5 Ga (beyond the simulation time) by extrapolating along an exponential fitted to the present day Q^{c} and $\mathrm{d}Q^{c}/\mathrm{d}t$.

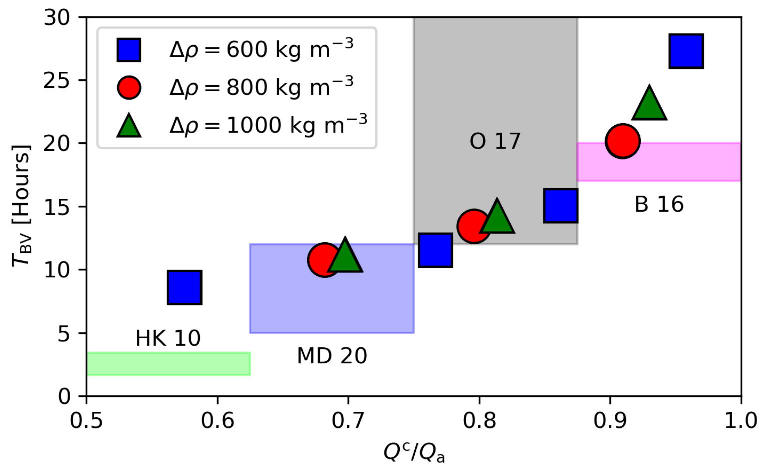

Figure 15: Buoyancy period, T_{BV}, for all models producing a stable layer, plotted as a function of the ratio $Q^{\mathrm{c}}/Q^{\mathrm{c}}_{\mathrm{a}}$. Squares, circles and triangles denote the ICB density jump used as indicated in the legend. Many models of the same $\Delta\rho$ plot on top of each other since the dominant control on T_{BV} is $Q^{\mathrm{c}}/Q^{\mathrm{c}}_{\mathrm{a}}$. Also shown are T_{BV} values from other studies (offset such that they do not overlap; they have no relation to the x-axis): HK 10 (Helffrich and Kaneshima, 2010), MD 20 (Mound and Davies, 2020), O 17 (Olson et al., 2017), and B 16 (Buffett et al., 2016). Note that the upper bound provided by Olson et al. (2017) stretches to infinity since they also promote models with no stratification.

within the core, or an external mechanism that enables the addition of material from the mantle. Internal mechanisms include the barodiffusion of light elements along the core pressure gradient (Fearn and Loper, 1981; Gubbins and Davies, 2013), immiscibility in the Fe-Si-O system at high pressure and temperature (Arveson et al., 2019), or the accumulation of light fluid parcels emitted from the inner core boundary (Moffatt and Loper, 1994; Bouffard et al., 2019). Komabayashi (2014) found that an increase in O concentration could decrease the seismic velocity in line with observations; however, Brodholt and Badro (2017) found that these simple accumulation mechanisms do not produce layers that are light and slow as required for a global stable layer. Instead Brodholt and Badro (2017) argue that an exchange of elements is required, for example by decreasing the Si concentration and increasing the O concentration compared to the bulk core. If one instead considers regional stratification then simple light element accumulation may not be incompatible with observations, though it is not clear how these internal mechanisms could generate enhanced chemical concentration on the scales suggested by the seismic observations. Clearly more work is required here; however, in the following we focus on external mechanisms.

Two external mechanisms for chemical stratification have been proposed. Landeau et al. (2016) used analogue experiments to argue that a stable layer of comparable thickness to seismic inferences could have been emplaced towards the end of core formation due to turbulent mixing between a light-element-enriched impactor and the proto-core. Jacobson et al. (2017) showed that changing equilibrium conditions during multi-stage core formation can lead to the formation of stable chemical layering. Their results indicate that the stable layer could be erased by a late giant impact, such as the hypothesised moon-forming event, though Bouffard et al. (2020) argue based on the results of Landeau et al. (2016) that the mixing efficiencies assumed by Jacobson et al. (2017) are too high and hence the stratification would have survived. A resolution to this issues awaits improved physical descriptions and observational constraints on core formation processes.

The second external mechanism for stratifying the upper core is through chemical interactions with the mantle. As established in Section 3 and originally shown by Frost et al. (2010) and Buffett and Seagle (2010), the core has likely been undersaturated in oxygen for much of its history and has therefore become progressively enriched in O at the CMB. Other elements such as Si and Mg may also have entered the core following its formation; however, the uncertainties are currently significant (see Section 3) and so here we focus on FeO partitioning.

The early core was probably susceptible to "oscillatory" double diffusive instabilities whereby radial oscillations develop into distinct convecting staircases (see Turner, 1973, and Section 4.2). Buffett and Seagle (2010) modelled the long term evolution of an oxygen enriched layer arising from a balance of the diffusive growth and convective entrainment due to staircases. They show that the amount of light element entrained into the bulk core is small relative to the inward diffusive flux of O at the CMB, which leads to the chemical layer growing to around 70 km in 4.5 Gyrs for a diffusivity of $D_O = 3 \times 10^{-9}$ m^2 s^{-1}. The growth is interrupted when the inner core forms since release of O at the ICB enriches the convecting fluid, however this only reduces the layer size by $\sim$10 km. Buffett and Seagle (2010) assumed a prescribed thermal evolution for the bulk core comprising a linear decrease in T and inner core growth $\propto \sqrt{t}$ which, whilst reasonable choices for their initial study, omits any feedback from the stable layer evolution on the evolution of the bulk core. In particular, Buffett and Seagle (2010) did not estimate the dynamo entropy E_J, which is important for ensuring that the calculated core history complies with paleomagnetic constraints.

Nakagawa (2018) adapted the model of Buffett and Seagle (2010), coupling it to the evolution of the bulk core, allowing feedback between the two regions. They found similar layer thicknesses to Buffett and Seagle (2010) since the enhanced oxygen concentrations give large density anomalies that are relatively insensitive to the heat loss of the core. Since it is assumed that diffusion primarily controls the evolution of the layer, the layer size is approximately $\propto \sqrt{D_O t}$, which Nakagawa (2018) confirms using a range of O diffusivities up to $D_O = 4.8 \times 10^{-8}$ m^2 s^{-1}. They obtained positive $E_{\rm J}$ using the entropy balance formulation of Labrosse et al. (2015) for layer thicknesses up to 270 km. In Labrosse et al. (2015), the entropy change due to mass diffusion, E_α, is not included which is reasonable when considering just the well-mixed core (Gubbins et al., 2004); however, strong gradients in chemically enriched layers mean that E_α is no longer negligible as we will show below.

Buffett and Seagle (2010) and Nakagawa (2018) both assume that mantle convection continually enriches the CMB in oxygen, such that the appropriate boundary condition is an imposed (time-varying) O concentration at the CMB. On the other hand, it seems plausible that either advection or diffusion in the mantle limit the replenishment of O-depleted material at the CMB (Davies et al., 2018). Taking optimistic estimates of $D^m_{FeO} = 10^{-12}$ m^2 s^{-1} for the diffusion coefficient of FeO in the solid mantle (Ammann et al., 2010) and a 20 mol% change in FeO composition across the chemical boundary layer in the lower mantle, Davies et al. (2018) obtained a chemical mass flux of $I_{FeO} \sim 1000$ kg s^{-1}. This value is comparable to the flux due to barodiffusion (Gubbins and Davies, 2013), which produces a $\sim$10% change in concentration at the top of the core over 4.5 Gyrs, a relatively small effect. A similar result is obtained when considering the (Stokes) rise time of a buoyant parcel of mantle material away from the CMB. The actual timescale for the Rayleigh-Taylor instability is more complex and depends on various uncertain quantities such as the lengthscale of the instability and the viscosity contrast between enriched and depleted layers (Ribe, 1998). Nevertheless, existing studies suggest that it is difficult to produce significant FeO flux through the solid mantle.

The high early core temperatures suggested by thermal history models with $k \sim 100$ W m^{-1} K^{-1} (Nimmo, 2015a; Davies, 2015; Labrosse et al., 2015) suggest that the presence of melting in a BMO should significantly enhance chemical exchange with the core (Brodholt and Badro, 2017). Davies et al. (2020) used the data of Pozzo et al. (2019) to model FeO exchange between the upper core and a BMO, extending the model of Labrosse et al. (2007). They found that the upper core could become strongly enriched in FeO (sometimes reaching a pure FeO composition) with stable layers of $70 - 80$ km thickness growing in the first 1 Gyr of evolution before reaching up to 150 km thickness at the present day. Furthermore, they found that FeO loss increased the freezing rate of the BMO in order to keep the region on the liquidus. Complete freezing of the BMO occurred in the first $1 - 3$ Gyrs following core formation and hence the BMO did not survive to the present day, contrasting with the original results of Labrosse et al. (2007).

Davies et al. (2020) did not calculate the entropy production E_{J} in the core and hence could not show that their FeO evolution models were consistent with the existence of a dynamo for the past 3.5 Gyrs. In order to calculate E_{J} it is important to account for the entropy E_α due to molecular diffusion, which is given by

$$E_\alpha = \int \frac{i^2}{\alpha_i^{\mathrm{D}} T} \mathrm{d}V, \tag{36}$$

(Gubbins et al., 2004). All else being equal, equation (35) shows that an increase in E_α reduces E_{J}, limiting the power available to the geodynamo. We have repeated the calculations from Davies et al. (2020), using the same formulation for the BMO evolution (following Labrosse et al., 2007), but with an altered core model. In Davies et al. (2020), the stable layer evolution was found by calculating oxygen diffusion in the top 400 km of the core subject to equation (3) at r_c (with no barodiffusion) and a Neumann condition at r_s given by , i.e. $\partial w_O/\partial r = -(\alpha_\mathrm{T}/\alpha^\mathrm{c}_O)\partial T/\partial r$ (Buffett and Seagle, 2010). Here we use the same approach but additionally calculate the change in layer size over time following Buffett and Seagle (2010). Treating the stable layer in this way makes little difference to the overall layer thickness but allows us to self-consistently partition energy and entropy between convecting and stable regions using the methodology in Greenwood et al. (2021) (note thermal stratification is not considered). Strictly the method of Buffett and Seagle (2010) is valid only when $Q^\mathrm{c} > Q^\mathrm{c}_\mathrm{a}$ as described above; however, in practice the layer evolution is set by the inward FeO flux, which dominates the downward entrainment at the base of the layer, and so the lower boundary condition (and hence the details of the double diffusive instability) have little effect. The upper boundary condition on Q^c is given by equation (2) with R given in Table 2 and the FeO flux calculated by the boundary layer model of Davies et al. (2020).

We first consider 2 example solutions that are identical except that one includes FeO transfer to the core while the other does not. We use the default BMO parameters in Labrosse et al. (2007) (as did Davies et al. (2020)) a partition coefficient of $P = K_d^{\mathrm{FeO}}/c^c_{Fe} = 10$ for the FeO dissolution reaction (Pozzo et al., 2019), a mantle FeO molar fraction of $c^m_{\mathrm{FeO}} = 0.05$, core oxygen molar fraction of $c^c_{\mathrm{O}} = 0.05$ and $k = 100$ W m^{-1} K^{-1}. These 2 solutions correspond to Figure 2 of Davies et al. (2020), where the case without FeO transfer is equivalent to the results of Labrosse et al. (2007). Our results differ from these mentioned studies only by the modifications to the core model, which does not affect the BMO evolution in this formulation. Core properties not already specified are taken from Davies et al. (2015) assuming an inner core density jump of 800 kg m^{-3}.

Figure 16 shows the energy and entropy sources from the 2 example solutions. The energy balance follows the behaviour described in Labrosse et al. (2007). The key observation is that radioactivity and release of latent heat in the BMO stifle the early CMB flow, which is reduced even further by the negative heat of reaction Q_{h} at the CMB [equation (2)]. In both examples, E_{J} is negative for the entire duration, indicating an absence of dynamo action. FeO transfer into the core initially produces an $E_\alpha > 1000$ MW K^{-1}, which quickly falls to between 250-500 MW K^{-1}, comparable to the entropy from thermal conduction E_{k} even in this high k scenario. Since $E_{\mathrm{k}} \propto k$ the thermal conductivity would need to be more than halved throughout the core in order to promote dynamo action in the case without FeO transfer. In the case with FeO transfer the geodynamo cannot operate for any k since E_α is sufficiently larger than E_{s} at all times. Finally, in this example the lifetime of the BMO is reduced from $\sim$ 4.5 Gyrs to less than 2 Gyrs with FeO loss, which causes the growth of a $\sim$100 km-thick chemically stable layer atop of the core.

We have found that none of the models in the ranges $P = 1-10$, $c^m_{\mathrm{FeO}} = 0.1-0.2$ and $c^c_{\mathrm{O}} = 0.05-0.13$ considered by Davies et al. (2020) produce a positive E_{J} during the lifetime of the BMO. We therefore made three plausible modifications to the Labrosse et al. (2007) model setup. First, we solve for the evolution of the solid mantle using the methodology of Driscoll and Bercovici (2014). Doing so allows us to produce a self-consistent heat flow out the top of the BMO and continue the calculation through to the present day once the BMO fully crystallises. The only modification to the solid mantle evolution from Driscoll and Bercovici (2014) is that the lower boundary is the time-dependent interface with the BMO, $r_{\mathrm{bmo}}(t)$. The heat flow into the solid mantle is defined using the difference in temperature between the BMO and the solid mantle and when the BMO fully freezes, the procedure is

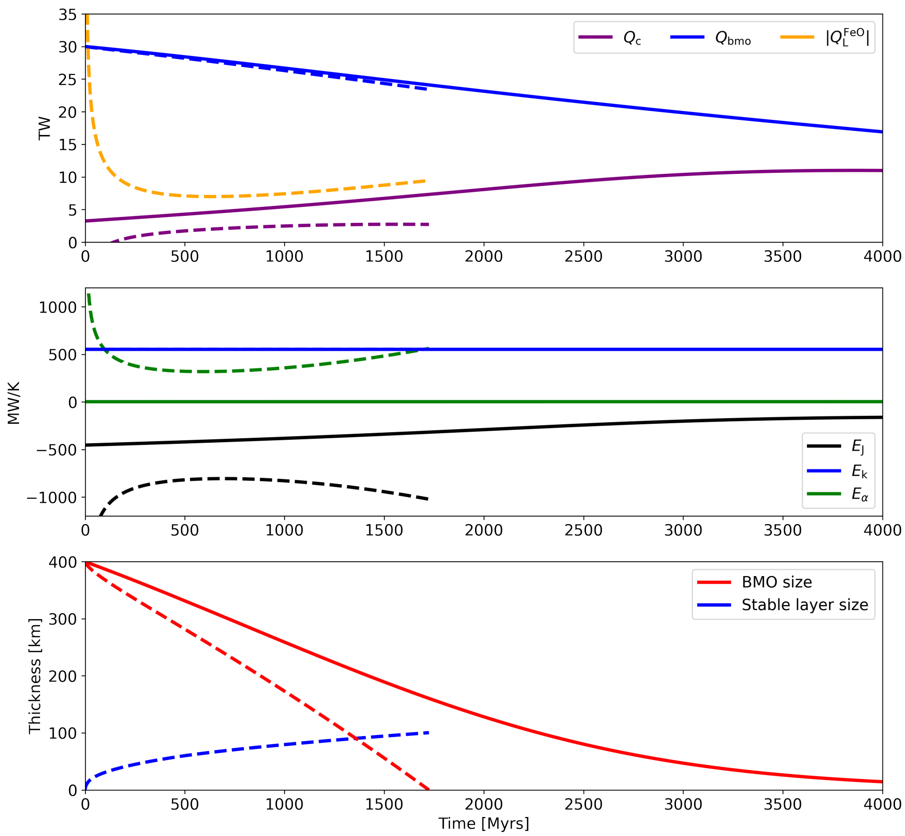

Figure 16: Examples of BMO evolution without (solid lines) and with (dashed lines) FeO transfer to the core, equivalent to those shown in Figure 2 of Davies et al. (2020). A partition coefficient of $P = 10$, a mantle FeO molar fraction of 0.05 and oxygen molar fraction of 0.05 in the core are used (see Davies et al. (2020) for a full set of parameters used for the BMO calculation). Top panel shows the energy sources within the BMO, middle panel shows the entropy sources within the core, and bottom panel shows the evolution of BMO and core stable layer thickness.

.

identical to that laid out in Driscoll and Bercovici (2014) for Earth. This modification produces a heat flow at $r_{\rm bmo}$ that is initially larger than that of Labrosse et al. (2007), but decreases more rapidly with time, which is more conducive for dynamo action.

Second, we raised the CMB temperature to 5500 K, the melting temperature of Bridgmanite at CMB pressure, which is the liquidus phase in the deep mantle (see review in Andrault et al., 2017). The presence of impurities would depress the melting point, perhaps by several hundred Kelvin, though this is still potentially within the significant uncertainties on the Bridgmanite melting point at these conditions (Stixrude et al., 2009). Higher initial temperatures allows sufficient cooling of the core to enable a dynamo since $\sim$4 whilst retaining the correct ICB radius. Finally, we increased the initial thickness of the BMO from 400 km (Labrosse et al., 2007) to 600 km, which increases the BMO lifetime, insulating the core from excessive heat loss to the solid mantle, particularly in the first 1 Gyrs. The initial thickness of the BMO is poorly constrained; however, values up to $\mathcal{O}(1000)$ km have been suggested (Stixrude et al., 2009; Blanc et al., 2020).

Figure 17 shows a suite of calculations with $P = 1-5$ and $c^m_{\rm FeO} = 0.1-0.2$, similar to the ranges considered by Davies et al. (2020). Higher P produces a larger FeO flux into the core, a larger E_α, and hence lower $E_{\rm J}$. $E_{\rm J}$ is initially negative in all models, but becomes positive around 4 Ga before declining towards inner core nucleation (ICN) and subsequently rising during inner core growth. Figure 17a shows that only models towards the lower range of P or $c^m_{\rm FeO}$ produce a positive $E_{\rm J}$ just prior to ICN. Figure 17b shows that at 4 Ga , approximately the earliest time where the presence of the geodynamo is constrained (Tarduno et al., 2015), only solutions with $P = 1$ and $c^m_{\rm FeO} < 0.2$ give $E_{\rm J} > 0$. The decrease of $E_{\rm J}$ with P is more significant at 4 Ga since oxygen is actively being transferred to the core, producing steeper chemical gradients that have not yet been smoothed out by diffusion. By ICN, the BMO has

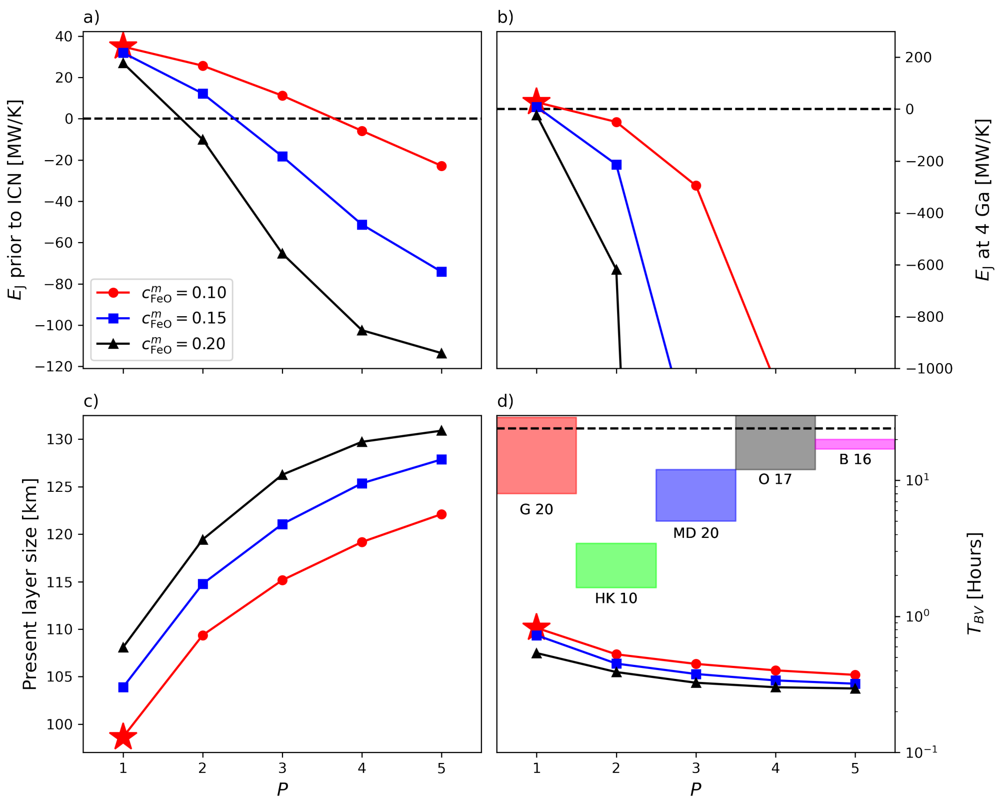

Figure 17: Results from the suite of models calculating the coupled evolution of the isentropic core, chemical stable layer, BMO, and solid mantle. All data are plotted with $P = 1 - 5$ on the horizontal axis, with varying mantle FeO concentrations shown by the colours that are consistent across each panel. Panels show values for $E_{\rm J}$ immediately prior to ICN (a) and at 4 Ga respectively (b), present-day chemical layer thickness at the top of the core (b), and the minimum Brunt-Väisälä period (peak N), $T_{\rm BV}$, for the present day layer (d) [equation (30)]. Also in panel (d) are $T_{\rm BV}$ values from other studies (offset such that they do not overlap; they have no relation to the x-axis): G 20 (Greenwood et al., 2021) (also equivalent to our results in section 4.3), HK 10 (Helffrich and Kaneshima, 2010), MD 20 (Mound and Davies, 2020), O 17 (Olson et al., 2017), and B 16 (Buffett et al., 2016). The dashed lines in (a) and (b) show $E_{\rm J} = 0$ and in (d) they show $T_{\rm BV} = 24$ hrs. Note the log scale in (d). Stars indicate the model which produces positive $E_{\rm J}$ for the last 4 Gyrs, which is discussed further in Section 6.

.

long since solidified, leading to a significant reduction in E_α.

Figure 17c plots the present day stable layer thickness, where as expected thicker layers are attained for larger P or c^m_{FeO}. However, the impact of varying input parameters causes thickness variations of only $\sim$30 km because the layer growth is limited by the small molecular diffusivity. Finally, Figure 17d shows the shortest T_{BV} within the layer at the present day. All models exhibit periods under 1 hour, indicating a very strong density stratification. There is a rapid increase in the periods as P is lowered and so achieving periods within the $1.45-3.5$ hours inferred from seismology (Helffrich and Kaneshima, 2010) would require a value of P of 1 or less. Other studies quoted on Figure 17d (Greenwood et al., 2021; Mound and Davies, 2020; Olson et al., 2017; Buffett et al., 2016) all favour much longer periods consistent instead with our previous results on thermal stratification.

In summary, the chemical stratification mechanisms that appear the most likely candidates to explain a thick and strongly stratified layer at the top of Earth's core are incomplete mixing during core formation (Landeau et al., 2016) and FeO exchange with the mantle (Buffett and Seagle, 2010; Brodholt and Badro, 2017). Whether a primordial layer can survive mixing due to late-stage impacts is a key issue that will benefit from improved models of core formation. We find that models of FeO transfer between a BMO and the core require relatively weak partitioning ($P \sim 1$) in order to enable dynamo action in the early core that continues to the present day while also producing present-day stable layers of similar strength to inferences from seismic models. These calculations are limited because they only include FeO partitioning with a constant value of P. Future work will need to couple the reactions of SiO_2 and MgO; however, as with the precipitation case it seems premature to move down this path owing to the significant uncertainties in the equilibrium calculations explained in Section 3. The multi-element calculations in Section 3.4 suggest that the core is strongly under-saturated in O, while P does not vary significantly when the BMO lifetime is short (and hence there is little variation in T). Therefore the calculations presented in this section hopefully represent a reasonable starting point for further investigations into coupled chemical core-mantle evolution.

It is notable that thermal stratification produces layers that match the thickness but not the stability inferred from seismology, instead predicting T_{BV} values more in line with inferences from geomagnetism. Conversely, FeO transfer produces layers that approximate the stability but not the thickness of the seismic observations, instead predicting layer thicknesses comparable to inferences from DNS and geomagnetism. One potential resolution is that the top of Earth's core comprises a strongly chemically stratified region embedded within and thicker and more weakly stratified layer. This scenario would require high T_{BV} values confined close to the CMB, with geomagnetic observations sampling an average stratification signal in the upper core.

5. Chemical Precipitation

In this section we discuss the effect of precipitation on the thermal and magnetic evolution of the core. The efficiency of precipitation in powering the geodynamo depends crucially on the precipitation rate $\mathrm{d}w_i^c/\mathrm{d}T$ of oxide i. Simple models assuming high conductivity and constant precipitation rates have shown that precipitation of MgO with $\mathrm{d}w_{MgO}^c/\mathrm{d}T = 5 \times 10^{-5}$ K^{-1} (O'Rourke and Stevenson, 2016) or precipitation of SiO_2 with $\mathrm{d}w_{SiO_2}^c/\mathrm{d}T = 4 \times 10^{-5}$ K^{-1} (Hirose et al., 2017) can maintain the geomagnetic field over the past 4 Gyrs with similar cooling rates and heat flows to those inferred from conventional low conductivity calculations. On the other hand, Du et al. (2019) found that high heat flows and cooling rates were still required to drive the dynamo using precipitation rates of $\mathrm{d}w_{MgO}^c/\mathrm{d}T = 6 \times 10^{-6}$ K^{-1} obtained from their experiments. Additional power provided by precipitation reduces the core cooling rate required to meet a given entropy production and hence predicts an older inner core age; however thermal history models with precipitation still predict super-solidus temperatures for the first $\sim 1-3$ Gyr after core formation (O'Rourke et al., 2017; Mittal et al., 2020) and so suggest the existence of a BMO at least in early times.

O'Rourke et al. (2017) conducted a large number of coupled core-mantle evolution models using a standard core setup (Labrosse et al., 2015) with the addition of precipitation (described in O'Rourke and Stevenson, 2016). Their mantle evolution model is from Korenaga (2006), which produces a much flatter CMB heat flow evolution compared to conventional mantle evolution models based on standard boundary layer theory (e.g. Driscoll and Bercovici, 2014; Jaupart et al., 2015, and Figure 13). O'Rourke et al. (2017) focused on the case where $k \approx 90$ W m^{-1} K^{-1} at the CMB and varied $\mathrm{d}w^c_{MgO}/\mathrm{d}T$ between 0 and 8×10^{-5} K^{-1}. For their nominal setup they found a preferred value of $\mathrm{d}w^c_{MgO}/\mathrm{d}T \sim 2 \times 10^{-5}$ to ensure E_J is sufficiently large to maintain dynamo action since core formation.

Mittal et al. (2020) modelled the simultaneous precipitation of Mg, Si and O. They coupled the evolution of the core and solid mantle to an intermediate 'interaction layer' comprising precipitated material (MgO, FeO and SiO_2) together with $MgSiO_3$ and $FeSiO_3$. In this model the interaction layer evolution is governed by a balance between growth due to precipitation and erosion by mantle flow. Mittal et al. (2020) found that a wide range of evolutionary scenarios are possible with different oxides precipitating at different times depending on the properties of the interaction layer (its thickness and erosion rate), the initial compositions and the parameters defining the equilibrium constants. This behaviour is consistent with the simple mass balance calculations presented in Section 3.

The large number of poorly constrained parameters mean that it is difficult to make general statements regarding the thermal and magnetic evolution of the core when precipitation is included. We therefore consider simple scenarios whereby MgO precipitation begins at core formation and proceeds at a constant rate in the range $0.3-1.5$ K^{-1} as shown in Figure 12. For simplicity we neglect the effects of SiO_2 and FeO and seek the minimum CMB heat flow that will enable dynamo action for the past 3.5 Gyrs. To do this we follow Nimmo (2015a) and Davies et al. (2015) and prescribe $E_{\rm J}=0$ before inner core formation and specify $Q^{\rm c}$ during inner core growth, which produces conservative estimates of the cooling rate, core temperature and inner core age and avoids the nonphysical behaviour that arises when $E_{\rm J}$ is fixed for all time (Nimmo, 2015a; Labrosse et al., 2015).

Figure 18 shows the predicted inner core age and the CMB temperature and CMB heat flow at 3.5 Ga, corresponding to the age of the paleointensity determinations of Tarduno et al. (2010). The shaded temperature range of 4150 ± 150 K corresponds to present estimates of the lower mantle solidus temperature (Fiquet et al., 2010; Andrault et al., 2011); core temperatures exceeding this range suggest partial melting in the past. Calculations are performed for the three values of $\Delta\rho = 600, 800$ and 1000 kg m^{-3} using parameters in Table 2 and core conductivity values of $k = 70$ W m^{-1} K^{-1} and $k = 100$ W m^{-1} K^{-1} (see Section 2.3). Also shown are favoured models from Labrosse et al. (2015), Driscoll and Bercovici (2014), Nakagawa and Tackley (2014) and Nimmo (2015a), who also consider high k but use different model setups and constraints on CMB heat flow.

Figure 18 shows that lower k values imply an older inner core and require lower CMB heat flow and core cooling rates to maintain the dynamo. Increasing $\Delta\rho$ from 600 kg m^{-3} to 1000 kg m^{-3} can produce a 600–800 K decrease in the early core temperature and a 200–400 Myr increase in the inner core age, depending on the details on the model. With ${\rm d}w^{c}_{Mg}/{\rm d}t \leq 0.3 \times 10^{-5}$ K^{-1} we find an inner core age of at most $300-600$ Gyrs ($400-800$ Gyrs) and minimum CMB heat flows at 3.5 Ga in the range $14-22$ TW ($10-15$ TW) for $k = 100$ W m^{-1} K^{-1} ($k = 70$ W m^{-1} K^{-1}). With a precipitation rate of 1.5×10^{-5} K^{-1} the maximum inner core age rises to $800-1100$ Gyrs ($1100-1500$ Gyrs) and required CMB heat flows at 3.5 Ga decrease to $8-9$ TW ($\sim$6 TW) for $k = 100$ W m^{-1} K^{-1} ($k = 70$ W m^{-1} K^{-1}). The vast majority of models predict an inner core age of at most 700 million years and early core temperatures exceeding the lower mantle solidus.

Davies et al. (2015) considered how uncertainties in a number of input parameters could affect predictions of inner core age and early core temperature. Within plausible ranges they varied the thermal expansivity, latent heat coefficient, specific heat capacity and core melting curve and found that the combined variations produced uncertainties on the inner core age of $\pm$150 Myr and the early temperature of $\pm$400 K. These uncertainties are comparable to the uncertainty in $\Delta\rho$ alone. When combined with the fact that the temperatures and inner core ages in Figure 18 are lower bounds this suggests that while MgO precipitation undoubtedly helps to relax the power requirements for the dynamo, some key implications of high core conductivity such as the existence of an early BMO remain even in the presence of precipitation. The inner core is also certainly much younger than the core, though its age is evidently rather uncertain. In particular these models cannot differentiate between paleomagnetic inferences of inner core nucleation at $\sim$0.5 Ga (Bono et al., 2019) and $\sim$1.3 Ga (Biggin et al., 2015).

6. Towards Resolving the New Core Paradox

Over the last few years various proposals have been put forth to resolve the new core paradox. Driscoll and Bercovici (2014) argued for 2 TW of heat produced by ^{40}K, which slows the core cooling rate for a given mantle heat flow and hence helps

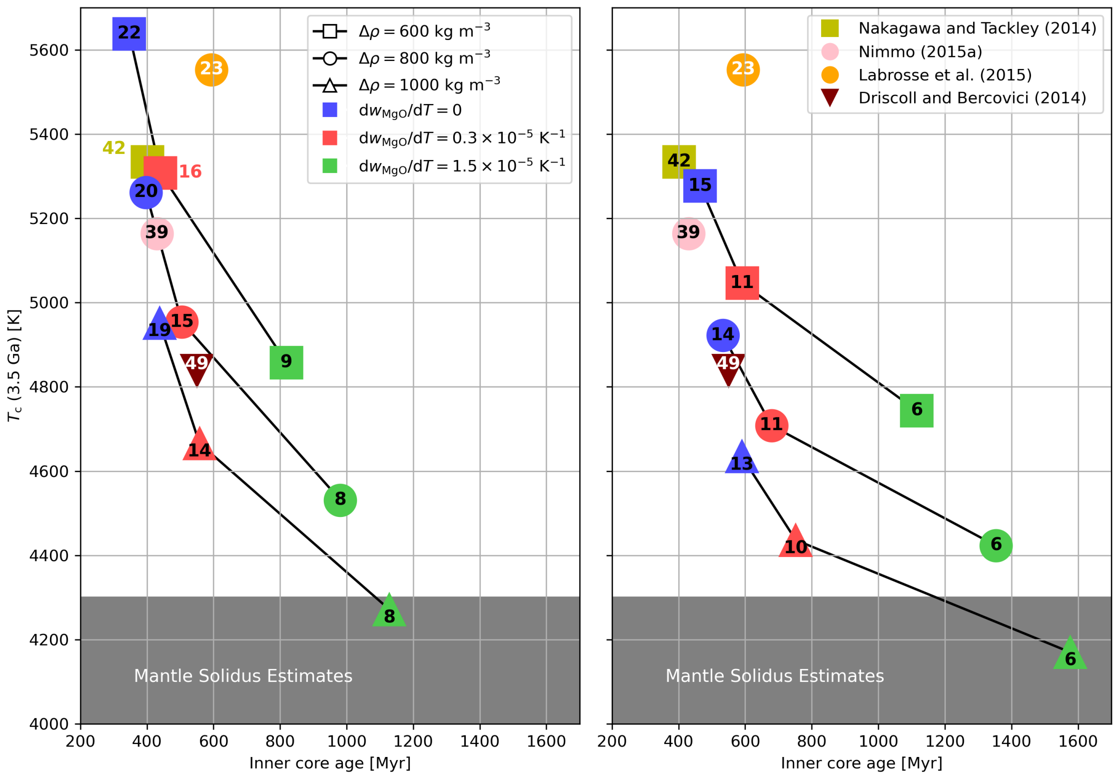

Figure 18: Effect on the inner core age and early CMB temperatures of MgO precipitation. Left panel shows our results using a CMB conductivity of $k = 100$ W m^{-1} K^{-1} and the right panel shows our results using $k = 70$ W m^{-1} K^{-1}. Symbols denote different core properties based on density jumps at the ICB of 600 (squares), 800 (circles), 1000 kg m^{-3} (triangles). Colours indicate no MgO precipitation (blue), and at a fixed rate of 0.3×10^{-5} K^{-1} (red) and 1.5×10^{-5} K^{-1} (green) as derived from Figure 12. Solid lines link models with the same core properties but varying rates of MgO precipitation. Numbers show the CMB heat flow in TW at 3.5 Ga. Results from other studies using a high thermal conductivity are also shown, replicated on both panels for comparison to each of our datasets. Based on Figure 3 in Davies et al. (2015).

to enable positive E_J before inner core formation. The drawback here is that experiments and simulations suggest that little ^{40}K partitioned into the core during formation (Chidester et al., 2017; Xiong et al., 2018). Precipitation provides another potential solution, though as we have seen it introduces a number of uncertain parameters and is difficult to constrain from available observations (though see Helffrich et al., 2018). Laneuville et al. (2018) suggested a compositionally stratified BMO, which helps to retain heat in the core; however, their model still suggests that the dynamo shuts off prior to inner core formation.

Here we present another possible resolution to the new core paradox that does not rely on precipitation or radiogenic heating. The approach is to retain the minimum number of physical processes (and hence poorly constrained parameters) while maintaining consistency with the basic predictions of core evolution with high conductivity. The early evolution involves coupled thermo-chemical interactions between the core and BMO, as expected from the high temperatures that arise in the high k scenario (Section 5). We allow exchange of FeO with the core, which actually lowers the available entropy (Section 4.4), but is suggested by a large range of core-mantle equilibrium calculations (Section 3.3). Consequently, a chemically stratified layer grows from the start of our model. FeO enrichment may enhance or be suppressed by a stratified layer was emplaced at core formation (Landeau et al., 2016), though we have not included this latter effect. Indeed, since erosion of chemical layers is expected to be weak (Bouffard et al., 2020) and layer growth is governed by diffusion we may anticipate similar long-term behaviour in the two cases. After complete freezing of the BMO the solid mantle follows the classical boundary-layer evolution described in the model of Driscoll and Bercovici (2014), with no further mass flux between core and mantle (Section 4.4). A “successful” model is required to produce positive E_J for all time and match the present-day ICB radius.

Figure 19 shows the results of one calculation that matches the constraints using $k = 70$ W m^{-1} K^{-1} and $\Delta\rho = 800$ kg m^{-3}, corresponding to the model denoted by a star in Figure 17. The BMO is initialised at 600 km thick and persists for 2 Gyrs producing a large flux of FeO into the core. The enhanced heat flux out of the BMO arising from our revisions to the original Labrosse et al. (2007) model (Section 4.4) enable the onset of dynamo action around 4 Ga with high k. Once the BMO freezes, the chemical layer continues to thicken by diffusion before the initiation and growth of the inner core around 0.8 Ga begins to erode it back towards the CMB. Prior to inner core formation E_{J} remains just above zero and hence the model predicts continuous dynamo action for the last 4 billion years. The present day heat flow and potential temperature at the top of the convecting mantle are respectively 35 TW and 1653 K, within current constraints of $35 - 41$ TW and $\sim$$1550 - 1750$ K (Jaupart et al., 2015), while the current inner core size is 1221 km as in Earth.

The results in Figures 19 are sensitive to the parameter choices as is evident by the fact that E_{J} remains just positive prior to inner core nucleation. In particular, increasing k above $k = 70$ W m^{-1} K^{-1}, which is on the lower end of the estimates presented in Section 2.3, causes E_{J} to fall below zero. We have not conducted an exhaustive search of the solution space, but did not obtain viable solutions in the absence of a BMO, using the original BMO setup of Labrosse et al. (2007), or with strong FeO partitioning ($P > 1$). However, while the solution might appear somewhat specialised, there are a large number of parameter combinations that have yet to be tested. Moreover, a large range of successful solutions are clearly available with only a modest additional amount of entropy due to precipitation or radiogenic heating that are within current observational or modelling uncertainties. Assuming precipitation of Mg and/or Si begins at a CMB temperature of 5000 K (Figure 12), the corresponding onset time for the solution in Figure 19 is 2.8 Ga. Prior to this

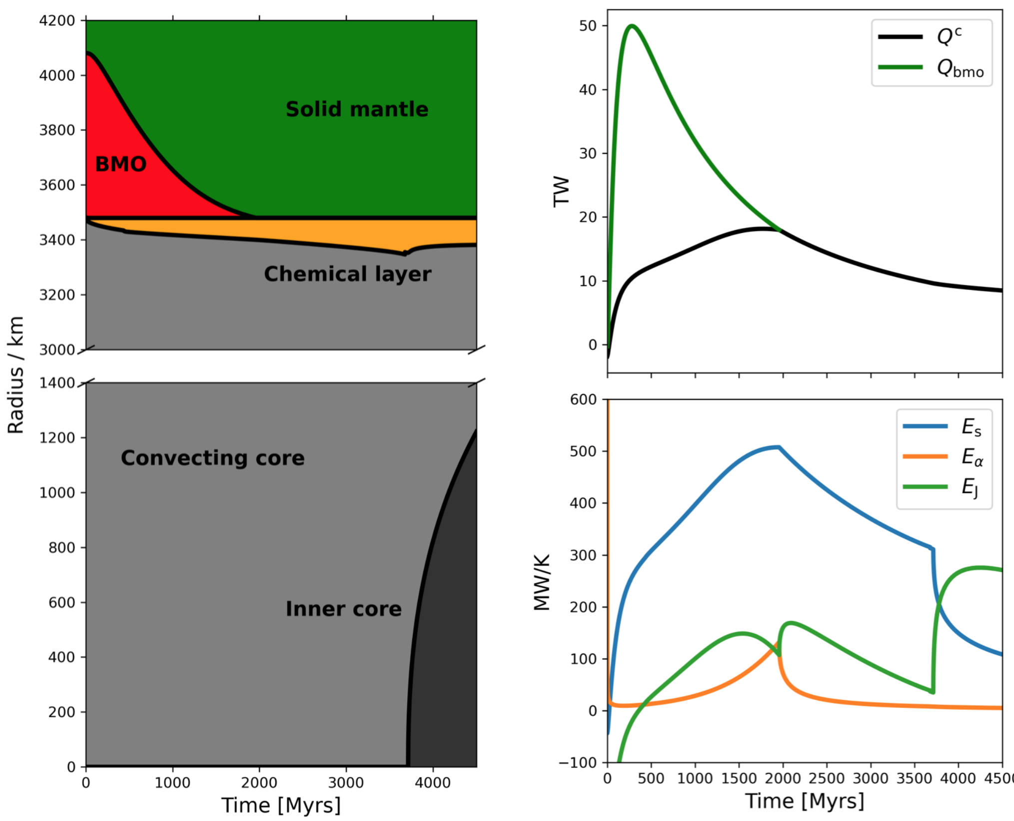

Figure 19: Results from our best model, indcated by the stars on Figure 17. On the left shows a radial cross section through time of the coupled Earth evolution. The inner core and convecting outer core are represented by the dark and light grey respectively. The chemically stratified layer is in orange, whilst the BMO and solid mantle are shown in red and green. Note the break in the y-axis and that both halves of the figure are to scale with each other. The right panels show energy (top) and entropy (bottom) sources from the calculation.

.

the dynamo would remain reliant on rapid cooling.

The solution in Figure 19 provides a number of predictions that can be tested with past and present observations. First, the Ohmic dissipation displays local minima just prior to inner core formation and completion of BMO freezing and a global minimum around 4 Ga. Since the magnetic field strength is thought to be proportional to E_{J} (Aubert et al., 2009) these minima might be observable in paleointensity data, though care is needed when translating E_{J} to an equivalent virtual dipole moment (Driscoll, 2016; Landeau et al., 2017; Driscoll and Wilson, 2018). The inner core age is 800 Myrs, which sits between the paleointensity changes inferred at $\sim$0.5 Ga by Bono et al. (2019) and $\sim$1.3 Ga by Biggin et al. (2015), while the delayed onset of dynamo action appears (perhaps coincidentally) close to the still debated Hadean paleointensity data of Tarduno et al. (2015). Nevertheless, the results will hopefully motivate future attempts to link paleointensity variations to abrupt changes in core evolution. Second, the present-day strength of stratification is strong enough to match the estimates derived from seismic observations (Helffrich and Kaneshima, 2010), but larger than inferences from MAC wave studies and geodynamo simulations. The stable layer thickness is 100 km, which is thinner than some seismic studies (Section 4.1) but more in line with inferences from geomagnetism and geodynamo simulations (Section 4.2). Finally, the present-day CMB heat flow is 8.5 TW, which is within the range of $7-17$ TW estimated by Nimmo (2015a) and the $5-15$ TW suggested by Lay et al. (2009). The core is actually mildly sub-adiabatic at present ($Q_{\mathrm{a}}^{\mathrm{c}} = 9.4$ TW), though we did not include this effect in the model. A potential resolution to the contrasting observational constraints on chemical vs thermal layers may be that a strongly stratified chemical sub-layer exists within a broader weakly stratified thermal layer.

It is worth noting that our preferred evolution scenario requires significant core cooling, with the CMB temperature falling from 5500 K to 4360 K over 4.5 Gyrs. Other scenarios have been proposed where the CMB temperature drop is much less dramatic, ∼300 K (Andrault et al., 2016). With high core conductivity we find rapid cooling is ubiquitous in our models and have not found a way to match the available constraints on core and mantle evolution with such slow cooling rates.

Many avenues for future work remain, as have been mentioned throughout this review. Systematic studies of core thermal conductivity approaching CMB conditions are needed to provide robust methods for extrapolating from lower $P-T$ conditions, while the effects of composition and the discordant results from direct experimental and computational determinations of k needs to be resolved. Improved constraints on the temperature- and composition-dependence of partitioning at CMB conditions as well as further systematic comparisons of candidate thermodynamic models (Badro et al., 2018) will help reduce the range of viable precipitation rates and onset times (Figure 12). Future seismic and geomagnetic observations together with high resolution DNS conducted in dynamical regions approaching Earth's core conditions (Aubert et al., 2017; Wicht and Sanchez, 2019) can help to constrain the existence, thickness, and global vs local nature of stable regions below the CMB. Finally, it is crucial to continue to seek observational evidence for the existence of a basal magma ocean, for example through its potential links to LLVPs and ultra-low velocity zones (Labrosse et al., 2015), and also for precipitation, perhaps in the form of a thin layer at the CMB or the incorporation of precipitation products into the mantle (Helffrich et al., 2018).

Improved constraints on the ICB density jump $\Delta\rho$ are also clearly needed. Wong et al. (2021) have made a potentially promising step in this direct by combining a theoretical model of a slurry region above the ICB (the so-called F-layer Souriau and Calvet, 2015) with seismic observations of 1D compressional wave-speed variations.

From a large suite of models that span uncertainties in the main input parameters, Wong et al. (2021) constrain $\Delta\rho \approx 530$ kg m^{-3}, on the lower end of the range of values obtained from normal modes (Masters and Gubbins, 2003). This model also yields an independent constraint on the CMB heat flow that is consistent with our preferred model.

Finally, we note that the structure, dynamics and evolution of layers within the core depends crucially on the role of myriad instabilities that can lead to partial or complete mixing. Parameterisations of these processes in thermal history models are rather crude (Greenwood et al., 2021), but rely heavily on results from DNS. In particular, future DNS studies will hopefully shed light on the role of double-diffusive instabilities and penetrative convection in the formation and survival of layering in the rapidly rotating, turbulent and magnetic environment that characterises the core.

7. Conclusions

We have reviewed the high thermal conductivity scenario for core evolution, which predicts a young inner core and early temperatures consistent with the existence of a basal magma ocean (Table 1). The main conclusions are:

- Consistent extrapolation of thermal and electrical conductivity estimates from a number of recent studies suggests $k = 70{-}110$ W m^{-1} K^{-1} at CMB conditions of 4000 K, 135 GPa and $\sim$10 mole percent light element;

- Both the onset time and rate of MgO and SiO_2 precipitation are uncertain and depend on a number of factors including temperature, compositions on both sides of the CMB, and the nature of the reactions that govern the equilibrium;

- MgO precipitation may begin anywhere between $3000 - 6000$ K with rates between $0.3 - 1.5 \times 10^{-5}$ K^{-1}. The majority of our calculations suggest a narrower range of onset between $4000-5000$ K with rates between $1.0-1.5\times 10^{-5}$ K^{-1};

- SiO_2 precipitation may begin anywhere between $3000-6000$ K with rates between $0.1-8\times10^{-5}$ K^{-1}. The majority of our calculations suggest a narrower range of onset between $3000-4500$ K with rates between $2-8\times10^{-5}$ K^{-1};

- The core is always undersaturated in O in our calculations, which causes FeO dissolution at all times;

- Our results suggest light elements dissolved into the core after its formation, forming a stably stratified chemical layer below the CMB. Precipitation was delayed, but once initiated would supply ample power for sustaining the geodynamo;

- Viable core evolution scenarios predict thermally stable layers at most $400-700$ km thick. The strength of stratification can match some inferences from geomagnetism but not values derived from seismic observations;

- The minimum requirements for maintaining the dynamo over the last 3.5 Gyrs suggest an inner core age of at most $300-600$ Gyrs ($400-800$ Gyrs) for $k=100$ W m^{-1} K^{-1} ($k=70$ W m^{-1} K^{-1}) and an MgO precipitation rate $\leq 0.3\times10^{-5}$ K^{-1}. With a precipitation rate of 1.5×10^{-5} K^{-1} the maximum inner core age is $800-1100$ Gyrs ($1100-1500$ Gyrs) for $k=100$ W m^{-1} K^{-1} ($k=70$ W m^{-1} K^{-1}). The temperature of the early core almost always exceeds present estimates of the mantle solidus, suggesting a BMO event with precipitation.

- We present a solution that overcomes the new core paradox by enabling continuous dynamo generation from 4 Ga to present. This model uses $k = 70$ W m^{-1} K^{-1} and matches the present inner core size and heat flow and temperature at the top of the convecting mantle. It predicts a present-day CMB heat flow of 8.5 TW, chemically stable layer of 100 km produced by FeO exchange with the mantle, and a BMO lifetime of 2 Gyrs.

Acknowledgements

SG is supported by NSF-NERC grant NE/T003855/1. CD acknowledges support via NERC grant NE/T000228/1. The authors are indebted to Prof. James Badro for detailed discussions and assistance benchmarking code used to calculate CMB equilibria. We are also grateful to Dr. Jon Mound, Dr. Alfred Wilson and Prof. Dario Alfè for commenting on various aspects of the article.

References

Adjaoud, O., Steinle-Neumann, G., Jahn, S., 2011. Transport properties of Mg_2SiO_4 liquid at high pressure: Physical state of a magma ocean. Earth Planet. Sci. Lett. 312 (3-4), 463–470.

Alexandrakis, C., Eaton, D., 2010. Precise seismic-wave velocity atop Earth's core: No evidence for outer-core stratification. Phys. Earth Planet. Int. 180, 59–65.

Alfè, D., Gillan, M., Price, G., 2002a. Composition and temperature of the Earth's core constrained by combining *ab initio* calculations and seismic data. Earth Planet. Sci. Lett. 195, 91–98.

Alfè, D., Gillan, M., Price, G., 2002b. *Ab initio* chemical potentials of solid and liquid solutions and the chemistry of the Earth's core. J. Chem. Phys. 116, 7127–7136.

Alfè, D., Price, G., Gillan, M., 2002c. Iron under Earth's core conditions: Liquid-state thermodynamics and high-pressure melting curve from *ab initio* calculations. Phys. Rev. B 65, 165118.

Amit, H., 2014. Can downwelling at the top of the Earth's core be detected in the geomagnetic secular variation? Phys. Earth Planet. Int. 229, 110–121.

Ammann, M., Brodholt, J., Wookey, J., Dobson, D., 2010. First-principles constraints on diffusion in lower-mantle minerals and a weak D". Nature 465, 462–465.

Andrault, D., Bolfan-Casanova, N., Bouhifd, M. A., Boujibar, A., Garbarino, G., Manthilake, G., Mezouar, M., Monteux, J., Parisiades, P., Pesce, G., 2017. Toward a coherent model for the melting behavior of the deep Earth's mantle. Phys. Earth Planet. Int. 265, 67–81.

Andrault, D., Bolfan-Casanova, N., Lo Nigro, G., Bouhifd, M., Garbarinho, G., Mezouar, M., 2011. Solidus and liquidus profiles of chondritic mantle: Implication for melting of the Earth across its history. Earth Planet. Sci. Lett. 304, 251–259.

Andrault, D., Monteux, J., Le Bars, M., Samuel, H., 2016. The deep Earth may not be cooling down. Earth Planet. Sci. Lett. 443, 195–203.

Anzellini, S., Dewaele, A., Mezouar, M., Loubeyre, P., Morard, G., 2013. Melting of iron at Earth's inner core boundary based on fast x-ray diffraction. Science 340, 464–466.

Arveson, S. M., Deng, J., Karki, B. B., Lee, K. K., 2019. Evidence for Fe-Si-O liquid immiscibility at deep Earth pressures. Proc. Natl. Acad. Sci. 116 (21), 10238–10243.

Aubert, J., Amit, H., Hulot, G., 2007. Detecting thermal boundary control in surface flows from numerical dynamos. Phys. Earth Planet. Int. 160, 143–156.

Aubert, J., Gastine, T., Fournier, A., 2017. Spherical convective dynamos in the rapidly rotating asymptotic regime. J. Fluid Mech. 813, 558–593.

Aubert, J., Labrosse, S., Poitou, C., 2009. Modelling the palaeo-evolution of the geodynamo. Geophys. J. Int. 179, 1414–1428.

Badro, J., Aubert, J., Hirose, K., Nomura, R., Blanchard, I., Borensztajn, S., Siebert, J., 2018. Magnesium partitioning between Earth's mantle and core and its potential to drive an early exsolution geodynamo. Geophys. Res. Lett. 45, 13–24.

Badro, J., Brodholt, J., Piet, H., Siebert, J., Ryerson, F., 2015. Core formation and core composition from coupled geochemical and geophysical constraints. Proc. Natl. Acad. Sci. 112, 12310–12314.

Badro, J., Côté, A., Brodholt, J., 2014. A seismologically consistent compositional model of Earth's core. Proc. Natl. Acad. Sci. 111, 7542–7545.

Badro, J., Siebert, J., Nimmo, F., 2016. An early geodynamo driven by exsolution of mantle components from Earth's core. Nature 536 (7616), 326.

Biggin, A., Piispa, E., Pesonen, L., Holme, R., Paterson, G., Veikkolainen, T., Tauxe, L., 2015. Palaeomagnetic field intensity variations suggest Mesoproterozoic inner-core nucleation. Nature 526 (7572), 245.

Blanc, N., Stegman, D., Ziegler, L., 2020. Thermal and magnetic evolution of a crystallizing basal magma ocean in Earth's mantle. Earth Planet. Sci. Lett. 534, 116085.

Bloxham, J., Jackson, A., 1990. Lateral temperature variations at the core-mantle boundary deduced from the magnetic field. Geophys. Res. Lett. 17, 1997–2000.

Bono, R. K., Tarduno, J. A., Nimmo, F., Cottrell, R. D., 2019. Young inner core inferred from Ediacaran ultra-low geomagnetic field intensity. Nat. Geosci. 12 (2), 143–147.

Bouffard, M., Choblet, G., Labrosse, S., Wicht, J., 2019. Chemical convection and stratification in the Earth's outer core. Frontiers in Earth Science 7, 99.

Bouffard, M., Landeau, M., Goument, A., 2020. Convective erosion of a primordial stratification atop Earth's core. Geophys. Res. Lett. 47 (14), e2020GL087109.

Bouhifd, M., Jephcoat, A., 2011. Convergence of Ni and Co metal-silicate partition coefficients in the deep magma-ocean and coupled silicon-oxygen solubility in iron melts at high pressures. Earth Planet. Sci. Lett. 307 (3), 341 – 348.

Braginsky, S., 1999. Dynamics of the stably stratified ocean at the top of the core. Phys. Earth Planet. Int. 111, 21–34.

Braginsky, S., Roberts, P., 1995. Equations governing convection in Earth's core and the geodynamo. Geophys. Astrophys. Fluid Dyn. 79, 1–97.

Brodholt, J., Badro, J., 2017. Composition of the low seismic velocity E' layer at the top of Earth's core. Geophys. Res. Lett. 44, 2017GL074261.

Buffett, B., 2014. Geomagnetic fluctuations reveal stable stratification at the top of the Earth's core. Nature 507, 484–487.

Buffett, B., 2015. Core-mantle interactions. In: Schubert, G. (Ed.), Treatise on Geophysics, Vol. 8: Core Dynamics. Elsevier, Amsterdam, pp. 213–224.

Buffett, B., Huppert, H., Lister, J., Woods, A., 1996. On the thermal evolution of the Earth's core. J. Geophys. Res. 101, 7989–8006.

Buffett, B., Knezek, N., Holme, R., 2016. Evidence for MAC waves at the top of Earth's core and implications for variations in length of day. Geophys. J. Int. 204, 1789–2000.

Buffett, B., Seagle, C., 2010. Stratification of the top of the core due to chemical interactions with the mantle. J. Geophys. Res. 115, B04407.

Caracas, R., Hirose, K., Nomura, R., Ballmer, M. D., 2019. Melt–crystal density crossover in a deep magma ocean. Earth Planet. Sci. Lett. 516, 202–211.

Chester, G., Thellung, A., 1961. The law of Wiedemann and Franz. Proc. Phys. Soc. London 77, 1005–1013.

Chidester, B. A., Rahman, Z., Righter, K., Campbell, A. J., 2017. Metal-silicate partitioning of U: Implications for the heat budget of the core and evidence for reduced U in the mantle. Geochimica et Cosmochimica Acta 199, 1 – 12.

Christensen, U., 2018. Geodynamo models with a stable layer and heterogeneous heat flow at the top of the core. Geophys. J. Int. 215 (2), 1338–1351.

Christensen, U., Aubert, J., Hulot, G., 2010. Conditions for Earth-like geodynamo models. Earth Planet. Sci. Lett. 296, 487–496.

Christensen, U. R., 2006. A deep dynamo generating Mercury's magnetic field. Nature 444 (7122), 1056–1058.

Constable, C., Korte, M., Panovska, S., 2016. Persistent high paleosecular variation activity in southern hemisphere for at least 10 000 years. Earth Planet. Sci. Lett. 453, 78–86.

Cox, G., Davies, C., Livermore, P., Singleton, J., 2019. Penetration of boundary-driven flows into a rotating spherical thermally-stratified fluid. J. Fluid Mech. 864, 519–553.

Davies, C., 2015. Cooling history of Earth's core with high thermal conductivity. Phys. Earth Planet. Int. 247, 65–79.

Davies, C., Gubbins, D., 2011. A buoyancy profile for the Earth's core. Geophys. J. Int. 187, 549–563.

Davies, C., Pozzo, M., Gubbins, D., Alfè, D., 2015. Constraints from material properties on the dynamics and evolution of Earth's core. Nat. Geosci. 8, 678–687.

Davies, C., Pozzo, M., Gubbins, D., Alfè, D., 2018. Partitioning of oxygen between ferropericlase and Earth's liquid core. Geophys. Res. Lett. 45, 6042–6050.

Davies, C., Pozzo, M., Gubbins, D., Alfè, D., 2020. Transfer of oxygen to Earth's core from a long-lived magma ocean. Earth Planet. Sci. Lett. 538, 116208.

de Koker, N., Steinle-Neumann, G., Vojtech, V., 2012. Electrical resistivity and thermal conductivity of liquid Fe alloys at high P and T and heat flux in Earth's core. Proc. Natl. Acad. Sci. 109, 4070–4073.

Driscoll, P., 2016. Simulating 2 Ga of geodynamo history. Geophys. Res. Lett. 43 (11), 5680–5687.

Driscoll, P., Bercovici, D., 2014. On the thermal and magnetic histories of Earth and

Venus: Influences of melting, radioactivity, and conductivity. Phys. Earth Planet. Int. 236, 36–51.

Driscoll, P. E., Du, Z., 2019. Geodynamo conductivity limits. Geophys. Res. Lett. 46 (14), 7982–7989.

Driscoll, P. E., Wilson, C., 2018. Paleomagnetic biases inferred from numerical dynamos and the search for geodynamo evolution. Frontiers in Earth Science 6, 113.

Du, Z., Boujibar, A., Driscoll, P., Fei, Y., 2019. Experimental constraints on an MgO exsolution-driven geodynamo. Geophys. Res. Lett. 46 (13), 7379–7385.

Du, Z., Jackson, C., Bennett, N., Driscoll, P., Deng, J., Lee, K., Greenberg, E., Prakapenka, V., Fei, Y., 2017. Insufficient energy from MgO exsolution to power early geodynamo. Geophys. Res. Lett. 4, 2017GL075283.

Dumberry, M., 2018. Earth Rotation, Excitation, Core. In: Grafarend, E. (Ed.), Encyclopedia of Geodesy. Springer International Publishing, Cham, pp. 1–5.

Dziewonski, A., Anderson, D., 1981. Preliminary Reference Earth Model. Phys. Earth Planet. Int. 25, 297–356.

Eggins, S., Rudnick, R., McDonough, W., 1998. The composition of peridotites and their minerals: a laser-ablation ICP–MS study. Earth Planet. Sci. Lett. 154 (1-4), 53–71.

Fearn, D., Loper, D., 1981. Compositional convection and stratification of Earth's core. Nature 289, 393–394.

Fiquet, G., Auzende, A., Siebert, J., Corgne, A., Bureau, H., Ozawa, H., Garbarino, G., 2010. Melting of peridotite to 140 gigapascals. Science 329, 1516–1518.

Fischer, R. A., Campbell, A. J., Ciesla, F. J., 2017. Sensitivities of Earth's core and mantle compositions to accretion and differentiation processes. Earth Planet. Sci. Lett. 458, 252–262.

Fischer, R. A., Cottrell, E., Hauri, E., Lee, K. K., Le Voyer, M., 2020. The carbon content of Earth and its core. Proc. Natl. Acad. Sci. 117 (16), 8743–8749.

Fischer, R. A., Nakajima, Y., Campbell, A. J., Frost, D. J., Harries, D., Langenhorst, F., Miyajima, N., Pollok, K., Rubie, D. C., 2015. High pressure metal-silicate partitioning of Ni, Co, V, Cr, Si, and O. Geochimica et Cosmochimica Acta 167 (Supplement C), 177 – 194.

Frost, D., Asahara, Y., Rubie, D., Miyajima, N., Dubrovinsky, L. S., Holzapfel, C., Ohtani, E., Miyahara, M., Sakai, T., 2010. Partitioning of oxygen between the Earth's mantle and core. J. Geophys. Res. 115, B02202.

Garaud, P., 2018. Double-diffusive convection at low Prandtl number. Annual Review of Fluid Mechanics 50, 275–298.

Garnero, E., McNamara, A., Shim, S.-H., 2016. Continent-sized anomalous zones with low seismic velocity at the base of Earth's mantle. Nat. Geosci. 9, 481–489.

Garnero, E. J., Helmberger, D. V., Grand, S. P., 1993. Constraining outermost core velocity with SmKS waves. Geophys. Res. Lett. 20 (22), 2463–2466.

Gastine, T., Aubert, J., Fournier, A., 2020. Dynamo-based limit to the extent of a stable layer atop Earth's core. Geophys. J. Int. 222 (2), 1433–1448.

Glane, S., Buffett, B., 2018. Enhanced core-mantle coupling due to stratification at the top of the core. Frontiers in Earth Science 6, 171.

Gomi, H., Ohta, K., Hirose, K., Labrosse, S., Caracas, R., Verstraete, V., Hernlund, J., 2013. The high conductivity of iron and thermal evolution of the Earth's core. Phys. Earth Planet. Int. 224, 88–103.

Greenwood, S., Davies, C., Mound, J., 2021. On the evolution of thermally stratified layers at the top of Earth's core. Phys. Earth Planet. Int.Preprint available on arXiv.

Gubbins, D., 2003. Thermal core-mantle interactions: theory and observations. In: Dehant, V., Creager, K., Karato, S., Zatman, S. (Eds.), Earth's core: Dynamics, Structure, Rotation. Geodynamics Series 31. American Geophysical Union, pp. 162–179.

Gubbins, D., Alfè, D., Davies, C., Pozzo, M., 2015. On core convection and the geodynamo: Effects of high electrical and thermal conductivity. Phys. Earth Planet. Int. 247, 56–64.

Gubbins, D., Alfe, D., Masters, G., Price, G., Gillan, M., 2003. Can the Earth's dynamo run on heat alone? Geophys. J. Int. 155, 609–622.

Gubbins, D., Alfè, D., Masters, G., Price, G., Gillan, M., 2004. Gross thermodynamics of two-component core convection. Geophys. J. Int. 157, 1407–1414.

Gubbins, D., Davies, C., 2013. The stratified layer at the core-mantle boundary caused by barodiffusion of Oxygen, Sulphur and Silicon. Phys. Earth Planet. Int. 215, 21–28.

Gubbins, D., Thomson, C., Whaler, K., 1982. Stable regions in the Earth's liquid core. Geophys. J. R. Astr. Soc. 68, 241–251.

Gubbins, D., Willis, A., Sreenivasan, B., 2007. Correlation of Earth's magnetic field with lower mantle thermal and seismic structure. Phys. Earth Planet. Int. 162, 256–260.

Hardy, C. M., Livermore, P. W., Niesen, J., 2020. Enhanced magnetic fields within a stratified layer. Geophys. J. Int. 222 (3), 1686–1703.

Helffrich, G., 2012. How light element addition can lower core liquid wave speeds. Geophys. J. Int., 1065–1070.

Helffrich, G., Ballmer, M. D., Hirose, K., 2018. Core-exsolved SiO_2 dispersal in the Earth's mantle. J. Geophys. Res. 123 (1), 176–188.

Helffrich, G., Hirose, K., Nomura, R., 2020. Thermodynamical Modeling of Liquid Fe-Si-Mg-O: Molten Magnesium Silicate Release From the Core. Geophys. Res. Lett. 47 (21), e2020GL089218.

Helffrich, G., Kaneshima, S., 2010. Outer-core compositional stratification from observed core wave speed profiles. Nature 468, 807–809.

Hernlund, J., McNamara, A., 2015. The Core-Mantle Boundary Region. In: Schubert, G. (Ed.), Treatise on Geophysics Vol. 7. Elsevier, pp. 461–519.

Hirose, K., Labrosse, S., Hernlund, J., 2013. Compositional state of Earth's core. Annual Review of Earth and Planetary Sciences 41, 657–691.

Hirose, K., Morard, G., Sinmyo, R., Umemoto, K., Hernlund, J., Helffrich, G., Labrosse, S., 2017. Crystallization of silicon dioxide and compositional evolution of the Earth's core. Nature 543 (7643), 99–102.

Holme, R., 2007. Large-scale flow in the core. In: Schubert, G. (Ed.), Treatise on Geophysics Vol. 8. Elsevier, pp. 107–130.

Holme, R., de Viron, O., 2013. Characterization and implications of intradecadal variations in length of day. Nature 499, 202–204.

Hsieh, W.-P., Goncharov, A. F., Labrosse, S., Holtgrewe, N., Lobanov, S. S., Chuvashova, I., Deschamps, F., Lin, J.-F., 2020. Low thermal conductivity of iron-silicon alloys at Earth's core conditions with implications for the geodynamo. Nat. Commun. 11 (1), 1–7.

Inoue, H., Suehiro, S., Ohta, K., Hirose, K., Ohishi, Y., 2020. Resistivity saturation of hcp Fe-Si alloys in an internally heated diamond anvil cell: A key to assessing the Earth's core conductivity. Earth Planet. Sci. Lett. 543, 116357.

Irving, J. C., Cottaar, S., Lekić, V., 2018. Seismically determined elastic parameters for Earth's outer core. Science advances 4 (6), eaar2538.

Jackson, A., Livermore, P., 2009. On Ohmic heating in the Earth's core I: nutation constraints. Geophys. J. Int. 177, 367–382.

Jacobson, S., Rubie, D., Herlund., J., Morbidelli, A., Nakajima, M., 2017. Formation, stratification, and mixing of the cores of Earth and Venus. Earth Planet. Sci. Lett. 474, 375–386.

Jaupart, C., Labrosse, S., Mareschal, J.-C., 2015. Temperatures, heat and energy in the mantle of the Earth. In: Schubert, G. (Ed.), Treatise on Geophysics, Vol. 7. Elsevier, Amsterdam, pp. 223–270.

Jaupart, E., Buffett, B., 2017. Generation of MAC waves by convection in Earth's core. Geophys. J. Int. 209 (2), 1326–1336.

Kaneshima, S., 2018. Array analysis of SmKS waves and stratification of Earth's outermost core. Phys. Earth Planet. Int. 276, 234–246.

Koelemeijer, P., Deuss, A., Ritsema, J., 2017. Density structure of Earth's lowermost mantle from Stoneley mode splitting observations. Nat. Commun. 8 (1), 1–10.

Komabayashi, T., 2014. Thermodynamics of melting relations in the system Fe-FeO at high pressure: Implications for oxygen in the Earth's core. J. Geophys. Res. 119 (5), 4164–4177.

Konôpková, Z., McWilliams, R., Gómez-Pérez, N., Goncharov, A., 2016. Direct measurement of thermal conductivity in solid iron at planetary core conditions. Nature 534, 99–101.

Korenaga, J., 2006. rchean geodynamics and the thermal evolution of Earth. Geophysical Monograph-American Geophysical Union 164, 7.

Labrosse, S., Hernlund, J., Coltice, N., 2007. A crystallizing dense magma ocean at the base of the Earth's mantle. Nature 450, 866–869.

Labrosse, S., Hernlund, J. W., Hirose, K., 2015. Fractional melting and freezing in the deep mantle and implications for the formation of a basal magma ocean. In: Badro, J., Walter, M. (Eds.), The early Earth: accretion and differentiation. AGU, Ch. 7, pp. 123–142.

Labrosse, S., Poirier, J.-P., Le Moeul, J.-L., 1997. On cooling of the Earth's core. Phys. Earth Planet. Int. 99, 1–17.

Labrosse, S., Poirier, J.-P., Le Moeul, J.-L., 2001. The age of the inner core. Earth Planet. Sci. Lett. 190, 111–123.

Landau, L., Lifshitz, E., 1987. Fluid mechanics (course of theoretical physics, volume 6), 2nd Edition. Permagon Press.

Landeau, M., Aubert, J., Olson, P., 2017. The signature of inner-core nucleation on the geodynamo. Earth Planet. Sci. Lett. 465, 193–204.

Landeau, M., Olson, P., Deguen, R., Hirsh, B. H., 2016. Core merging and stratification following giant impact. Nat. Geosci. 1 (September), 1–5.

Laneuville, M., Hernlund, J., Labrosse, S., Guttenberg, N., 2018. Crystallization of a compositionally stratified basal magma ocean. Phys. Earth Planet. Int. 276, 86–92.

Lau, H. C., Mitrovica, J. X., Davis, J. L., Tromp, J., Yang, H.-Y., Al-Attar, D., 2017. Tidal tomography constrains Earth's deep-mantle buoyancy. Nature 551 (7680), 321–326.

Lay, T., Hernlund, J., Buffett, B., 2009. Core-mantle boundary heat flow. Nat. Geosci. 1, 25–32.

Lay, T., Young, C., 1990. The stably-stratified outermost core revisited. Geophys. Res. Lett. 71, 2001–2004.

Lesur, V., Whaler, K., Wardinski, I., 2015. Are geomagnetic data consistent with stably stratified flow at the core-mantle boundary? Geophys. J. Int., 929–946.

Levy, M., Fernando, H., 2002. Turbulent thermal convection in a rotating stratified fluid. Journal of Fluid Mechanics 467, 19.

Li, Y., Vočadlo, L., Alfè, D., Brodholt, J., 2019. Carbon partitioning between the Earth's inner and outer core. J. Geophys. Res. 124 (12), 12812–12824.

Lister, J., Buffett, B., 1998. Stratification of the outer core at the core-mantle boundary. Phys. Earth Planet. Int. 105, 5–19.

Liu, W., Zhang, Y., Yin, Q.-Z., Zhao, Y., Zhang, Z., 2020. Magnesium partitioning between silicate melt and liquid iron using first-principles molecular dynamics: Implications for the early thermal history of the Earth's core. Earth Planet. Sci. Lett. 531, 115934.

Long, R., Mound, J., Davies, C., Tobias, S., 2020. Scaling behaviour in spherical shell rotating convection with fixed-flux thermal boundary conditions. J. Fluid Mech. 889.

Masters, G., Gubbins, D., 2003. On the resolution of density within the Earth. Phys. Earth Planet. Int. 140, 159–167.

Mather, J. F., Simitev, R. D., 2020. Regimes of thermo-compositional convection and related dynamos in rotating spherical shells. Geophys. Astrophys. Fluid Dyn., 1–24.

Metman, M. C., Livermore, P. W., Mound, J. E., Beggan, C. D., 2019. Modelling decadal secular variation with only magnetic diffusion. Geophysical Journal International 219 (Supplement_1), S58–S82.

Mittal, T., Knezek, N., Arveson, S. M., McGuire, C. P., Williams, C. D., Jones, T. D., Li, J., 2020. Precipitation of multiple light elements to power Earth's early dynamo. Earth Planet. Sci. Lett. 532, 116030.

Moffatt, H., Loper, D., 1994. The magnetostrophic rise of a buoyant parcel in the Earth's core. Geophys. J. Int. 117, 394–402.

Monville, R., Vidal, J., Cébron, D., Schaeffer, N., 2019. Rotating double-diffusive convection in stably stratified planetary cores. Geophys. J. Int. 219 (Supplement_1), S195–S218.

Mound, J., Davies, C., Rost, S., Aurnou, J., 2019. Regional stratification at the top of Earth's core due to core-mantle boundary heat flux variations. Nat. Geosci.

Mound, J. E., Davies, C. J., 2020. Scaling Laws for Regional Stratification at the Top of Earth's Core. Geophys. Res. Lett. 47 (16), e2020GL087715.

Nakagawa, T., 2011. Effect of a stably stratified layer near the outer boundary in numerical simulations of a magnetohydrodynamic dynamo in a rotating spherical shell and its implications for Earth's core. Phys. Earth Planet. Int. 187, 342–352.

Nakagawa, T., 2018. On the thermo-chemical origin of the stratified region at the top of the Earth's core. Phys. Earth Planet. Int. 276, 172–181.

Nakagawa, T., 2020. A coupled core-mantle evolution: review and future prospects. Progress in Earth and Planetary Science 7 (1), 1–17.

Nakagawa, T., Tackley, P., 2014. Influence of combined primordial layering and recycled MORB on the coupled thermal evolution of Earth's mantle and core. Geochem. Geophys. Geosys. 15, 619–633.

Nimmo, F., 2015a. Energetics of the core. In: Schubert, G. (Ed.), Treatise on Geophysics 2nd Edn, Vol. 8. Elsevier, Amsterdam, pp. 27–55.

Nimmo, F., 2015b. Thermal and compositional evolution of the core. In: Schubert, G. (Ed.), Treatise on Geophysics 2nd Edn, Vol. 9. Elsevier, Amsterdam, pp. 209–219.

Nimmo, F., Price, G., Brodholt, J., Gubbins, D., 2004. The influence of potassium on core and geodynamo evolution. Geophys. J. Int. 156, 363–376.

Ohta, K., Kuwayama, Y., Hirose, K., Shimizu, K., Ohishi, Y., 2016. Experimental determination of the electrical resistivity of iron at Earth's core conditions. Nature 534 (7605), 95.

Olson, P., Deguen, R., Rudolph, M., Zhong, S., 2015. Core evolution driven by mantle global circulation. Phys. Earth Planet. Int. 243, 44–55.

Olson, P., Landeau, M., Reynolds, E., 2017. Dynamo tests for stratification below the core-mantle boundary. Phys. Earth Planet. Int. 271, 1–18.

Olson, P., Landeau, M., Reynolds, E., 2018. Outer core stratification from the high latitude structure of the geomagnetic field. Frontiers in Earth Science 6, 140.

O'Rourke, J., Korenaga, J., Stevenson, D., 2017. Thermal evolution of Earth with magnesium precipitation in the core. Earth Planet. Sci. Lett. 458, 263–272.

O'Rourke, J. G., Stevenson, D. J., 2016. Powering Earth's dynamo with magnesium precipitation from the core. Nature 529 (7586), 387–389.

Ozawa, H., Hirose, K., Mitome, M., Bando, Y., Sata, N., Ohishi, Y., 2008. Chemical equilibrium between ferropericlase and molten iron to 134 GPa and implications for iron content at the bottom of the mantle. Geophys. Res. Lett. 35, L05308.

Patočka, V., Šrámek, O., Tosi, N., 2020. Minimum heat flow from the core and thermal evolution of the Earth. Phys. Earth Planet. Int. 305, 106457.

Posner, E. S., Schmickler, B., Rubie, D. C., 2018. Self-diffusion and chemical diffusion in peridotite melt at high pressure and implications for magma ocean viscosities. Chemical Geology 502, 66–75.

Pourovskii, L., Mravlje, J., Pozzo, M., Alfe, D., 2020. Electronic correlations and transport in iron at Earth's core conditions. Nat. Commun. 11 (1), 1–8.

Pozzo, M., Alfè, D., 2016. Saturation of electrical resistivity of solid iron at earth's core conditions. SpringerPlus 5 (1), 1–6.

Pozzo, M., Davies, C., Gubbins, D., Alfè, D., 2012. Thermal and electrical conductivity of iron at Earth's core conditions. Nature 485, 355–358.

Pozzo, M., Davies, C., Gubbins, D., Alfè, D., 2013. Transport properties for liquid silicon-oxygen-iron mixtures at Earth's core conditions. Phys. Rev. B 87, 014110.

Pozzo, M., Davies, C., Gubbins, D., Alfè, D., 2019. The FeO Content of Earth's Core. Phys. Rev. X 9, 041018.

Ribe, N., 1998. Spouting and planform selection in the Rayleigh–Taylor instability of miscible viscous fluids. J. Fluid Mech. 377, 27–45.

Roberts, P., Scott, S., 1965. On analysis of the secular variation. I. a hydromagnetic constraint: Theory. J. Geomagn. Geoelectr. 17, 137–151.

Rubie, D., Nimmo, F., Melosh, H., 2015a. Formation of Earth's Core. In: Schubert, G. (Ed.), Treatise on Geophysics 2nd Edn, Vol. 9. Elsevier, Amsterdam, pp. 43–79.

Rubie, D. C., Frost, D. J., Mann, U., Asahara, Y., Nimmo, F., Tsuno, K., Kegler, P., Holzheid, A., Palme, H., 2011. Heterogeneous accretion, composition and core-mantle differentiation of the Earth. Earth Planet. Sci. Lett. 301, 31–42.

Rubie, D. C., Jacobson, S. A., Morbidelli, A., O'Brien, D. P., Young, E. D., de Vries, J., Nimmo, F., Palme, H., Frost, D. J., 2015b. Accretion and differentiation of the terrestrial planets with implications for the compositions of early-formed Solar System bodies and accretion of water. Icarus 248, 89–108.

Secco, R. A., 2017. Thermal conductivity and Seebeck coefficient of Fe and Fe-Si alloys: Implications for variable Lorenz number. Phys. Earth Planet. Int. 265, 23–34.

Siebert, J., Badro, J., Antonangeli, D., Ryerson, F. J., 2012. Metal-silicate partitioning of Ni and Co in a deep magma ocean. Earth Planet. Sci. Lett. 321 (Supplement C), 189 – 197.

Sinmyo, R., Hirose, K., Ohishi, Y., 2019. Melting curve of iron to 290 GPa determined in a resistance-heated diamond-anvil cell. Earth Planet. Sci. Lett. 510, 45–52.

Solomatov, V., 2015. Magma oceans and primordial mantle differentiation. In: Schubert, G. (Ed.), Treatise on Geophysics 2nd Edn, Vol. 10. Elsevier, Amsterdam, pp. 81–104.

Souriau, A., Calvet, M., 2015. Deep Earth structure – the Earth's cores. In: Schubert, G., Romanowicz, B., Dziewonski, A. (Eds.), Treatise on geophysics. Vol. 1. Elsevier, Amsterdam, Ch. 23, pp. 725–757.

Stevenson, D., 1987. Limits on lateral density and velocity variations in the Earth's outer core. Geophys. J. Int. 88, 311–319.

Stixrude, L., de Koker, N., Sun, N., Mookherjee, M., Karki, B. B., 2009. Thermodynamics of silicate liquids in the deep Earth. Earth Planet. Sci. Lett. 278 (3-4), 226–232.

Suer, T.-A., Siebert, J., Remusat, L., Menguy, N., Fiquet, G., 2017. A sulfur-poor terrestrial core inferred from metal-silicate partitioning experiments. Earth Planet. Sci. Lett. 469 (Supplement C), 84 – 97.

Takafuji, N., Hirose, K., Mitome, M., Bando, Y., 2005. Solubilities of O and Si in liquid iron in equilibrium with (Mg,Fe)SiO_3 perovskite and the light elements in the core. Geophys. Res. Lett. 32 (6), L06313.

Takehiro, S.-i., Lister, J. R., 2001. Penetration of columnar convection into an outer stably stratified layer in rapidly rotating spherical fluid shells. Earth Planet. Sci. Lett. 187 (3-4), 357–366.

Tang, F., Taylor, R. J., Einsle, J. F., Borlina, C. S., Fu, R. R., Weiss, B. P., Williams, H. M., Williams, W., Nagy, L., Midgley, P. A., et al., 2019. Secondary magnetite in ancient zircon precludes analysis of a Hadean geodynamo. Proc. Natl. Acad. Sci. 116 (2), 407–412.

Tarduno, J., Cottrell, R., Bono, R., Oda, H., Davis, W., Fayek, M., van't Erve, O., Nimmo, F., Huang, W., Thern, E., et al., 2020. Paleomagnetism indicates that primary magnetite in zircon records a strong Hadean geodynamo. Proc. Natl. Acad. Sci. 117 (5), 2309–2318.

Tarduno, J., Cottrell, R., Watkeys, M., Hofmann, A., Doubrovine, P., Mamajek, E., Liu, D., Sibeck, D., Neukirch, L., Usui, Y., 2010. Geodynamo, solar wind, and magnetopause 3.4 to 3.45 billion years ago. Science 327, 1238–1240.

Tarduno, J. A., Cottrell, R. D., Davis, W. J., Nimmo, F., Bono, R. K., 2015. A Hadean to Paleoarchean geodynamo recorded by single zircon crystals. Science 349, 521–524.

Tauxe, L., Yamazaki, T., 2015. 5.13-paleointensities. In: Treatise on Geophysics. Elsevier, pp. 461–509.

Tilgner, A., 2015. Rotational Dynamics of the Core. In: Schubert, G. (Ed.), Treatise on Geophysics, 8.07. Elsevier, Amsterdam, pp. 183–212.

Tsuno, K., Frost, D. J., Rubie, D. C., 2013. Simultaneous partitioning of silicon and oxygen into the Earth's core during early Earth differentiation. Geophys. Res. Lett. 40, 66–71.

Turner, J., 1973. Buoyancy effects in fluids. Cambridge University Press.

Umemoto, K., Hirose, K., 2020. Chemical compositions of the outer core examined by first principles calculations. Earth Planet. Sci. Lett. 531, 116009.

van Tent, R., Deuss, A., Kaneshima, S., Thomas, C., 2020. The signal of outermost-core stratification in body-wave and normal-mode data. Geophys. J. Int. 223 (2), 1338–1354.

Whaler, K. A., 1980. Does the whole of the Earth's core convect? Nature 287, 528–530.

Whaler, K. A., 1986. Geomagnetic evidence for fluid upwelling at the core-mantle boundary. Geophys. J. R. Astr. Soc. 86, 563–588.

Wicht, J., Sanchez, S., 2019. Advances in geodynamo modelling. Geophys. Astrophys. Fluid Dyn. 113 (1-2), 2–50.

Williams, Q., 2018. The thermal conductivity of Earth's core: a key geophysical parameter's constraints and uncertainties. Annual Review of Earth and Planetary Sciences 46, 47–66.

Wong, J., Davies, C. J., Jones, C. A., 2021. A regime diagram for the slurry F-layer at the base of Earth's outer core. Earth Planet. Sci. Lett. 560, 116791.

Xiong, Z., Tsuchiya, T., Taniuchi, T., 2018. Ab initio prediction of potassium partitioning into Earth's core. J. Geophys. Res. 123 (8), 6451–6458.

Xu, J., Zhang, P., Haule, K., Minar, J., Wimmer, S., Ebert, H., Cohen, R., 2018. Thermal conductivity and electrical resistivity of solid iron at Earth's core conditions from first principles. Phys. Rev. Lett. 121 (9), 096601.

Yan, C., Stanley, S., 2018. Sensitivity of the geomagnetic octupole to a stably stratified layer in the Earth's core. Geophys. Res. Lett. 45 (20), 11–005.

Zhang, K., 1992. Convection in a rapidly rotating spherical shell at infinite Prandtl number: transition to vacillating flows. Phys. Earth Planet. Int. 72, 236–248.

Zhang, Y., Hou, M., Liu, G., Zhang, C., Prakapenka, V. B., Greenberg, E., Fei, Y., Cohen, R., Lin, J.-F., 2020. Reconciliation of experiments and theory on transport properties of iron and the geodynamo. Phys. Rev. Lett. 125 (7), 078501.

Appendix A. Mass Balance Between the Core and Magma Ocean

We implement three differences compared to the algorithm presented in Rubie et al. (2011): 1) Mg replaces Ni in the reaction set; 2) distribution coefficients for Si and Mg are defined by dissociation reactions rather than exchange reactions. We start by considering the reaction

$$[(FeO)_x(MgO)_y(SiO_2)_z] + [(Fe)_a(Mg)_bO_c(Si)_d] \Longleftrightarrow \tag{A.1}$$

$$[(FeO)_{x'}(MgO)_{y'}(SiO_2)_{z'}] + [(Fe)_{a'}(Mg)_{b'}O_{c'}(Si)_{d'}]\,. \tag{A.2}$$

which is essentially the reaction considered by Rubie et al. (2011), ignoring elements that do not partition and replacing Ni with Mg. Mass conservation demands

$$a' = x + a - x', \tag{A.3}$$

$$b' = y + b - y', \tag{A.4}$$

$$c' = x + y + 2z + c - x' - y' - 2z', \tag{A.5}$$

$$d' = z + d - z'. \tag{A.6}$$

The distribution coefficients are given in this notation by

$$K_D^O = \frac{c_{Fe}c_O}{c_{FeO}} = \frac{a'c'}{x'}\frac{(x'+y'+z')}{(a'+b'+c'+d')^2} \tag{A.7}$$

$$K_D^{Mg} = \frac{c_{Mg}c_O}{c_{MgO}} = \frac{b'c'}{y'}\frac{(x'+y'+z')}{(a'+b'+c'+d')^2} \tag{A.8}$$

$$K_D^{Si} = \frac{c_{Si}c_O^2}{c_{SiO_2}} = \frac{d'(c')^2}{z'}\frac{(x'+y'+z')}{(a'+b'+c'+d')^3}. \tag{A.9}$$

The procedure of Rubie et al. (2011) starts by guessing a value for x', which gives a' from equation (A.3). Next y' is obtained from the definition of K_D^{Mg}. We note that

$$\frac{K_D^{Mg}}{K_D^O} = \frac{x'b'}{y'a'}, \tag{A.10}$$

which is the same result as equation S12 in Rubie et al. (2011) despite the fact that we are considering different reactions. This arises since the FeO and MgO concentrations in the silicate are determined by the amount of Fe and Mg respectively. Equation (A.10) allows us to determine y' from an initial guess at x'. Using the definitions of b' and y' gives

$$y' = \frac{x'(y+b)}{(x+a-x')K_D^{Mg}/K_D^O + x'}. \tag{A.11}$$

and hence b' is also determined from equation (A.4).

To obtain z' substitute equations (A.5) and (A.6) into the definition of K_D^O/K_D^{Si}, obtaining

$$\frac{K_D^O}{K_D^{Si}} = \frac{a'c'z'(a'+b'+c'+d')}{x'd'(c')^2}, \tag{A.12}$$

$$= \frac{a'z'(a'+b'+x+y+3z+c-x'-y'-3z'+d)^2}{x'(z+d-z')(x+y+2z+c-x'-y'-2z')}. \tag{A.13}$$

Defining

$$\alpha = z+d, \tag{A.14}$$

$$\gamma = a'+b'+x+y+3z+c-x'-y'+d, \tag{A.15}$$

$$\sigma = x+y+2z+c-x'-y', \tag{A.16}$$

we can write

$$\frac{K_D^O}{K_D^{Si}} = \frac{a'z'(\gamma-3z')}{x'(\alpha-z')(\sigma-2z')}, \tag{A.17}$$

which turns in to a quadratic equation for z':

$$(z')^2\left[3a' + 2x'\frac{K_D^O}{K_D^{Si}}\right] - z'\left[(2\alpha x') + x'\sigma)\frac{K_D^O}{K_D^{Si}} + a'\gamma\right] + \frac{K_D^O}{K_D^{Si}}x'\alpha\sigma = 0. \tag{A.18}$$

We note here an analytical solution for the special case where exchange of Fe and

Si is disallowed. We require that

$$x = x', a = a', z = z', d = d'. \tag{A.19}$$

The mass balance equations reduce to

$$b' = y + b - y' \tag{A.20}$$

$$c' = y - y' + c, \tag{A.21}$$

while the distribution coefficients are

$$K_D^O = \frac{ac'(x + y' + z)}{x(a + b' + c' + d)^2}, \tag{A.22}$$

$$K_D^{Mg} = \frac{b'c'(x + y' + z)}{y'(a + b' + c' + d)^2}, \tag{A.23}$$

$$K_D^{Si} = \frac{d(c')^2(x + y' + z)}{z(a + b' + c' + d)^3}, \tag{A.24}$$

$$\frac{K_D^{Mg}}{K_D^O} = \frac{xb'}{a(y + b - b')}, \tag{A.25}$$

$$\frac{K_D^O}{K_D^{Si}} = \frac{az(a + b' + c' + d)}{xdc'}. \tag{A.26}$$

From the first ratio we find a solution for b' as

$$b' = \frac{a(y + b)K_{Mg}/K_O}{x + aK_{Mg}/K_O} \tag{A.27}$$

and from the second ratio we get

$$b' = \left[az(a + c - b + d) - \frac{K_O}{K_{Si}}xd(c - b)\right]\left(\frac{K_O}{K_{Si}}xd - 2az\right). \tag{A.28}$$

Equating these two expressions gives a constraint on the input compositions.